SUBSTRATE STIFFNESS TUNES THE NEURONAL RESPONSE TO THE CHEMICAL GUIDANCE CUE SEMAPHORIN3A

Sarah Foster

Churchill College

Department of Physiology, Development, and Neuroscience

University of Cambridge

This dissertation is submitted for the degree of Doctor of Philosophy

January 2020

DECLARATION

This dissertation is the result of my own work and includes nothing, which is the outcome of work done in collaboration except where specifically indicated in the text. It has not been previously submitted, in part or whole, to any university of institution for any degree, diploma, or other qualification. Material mentioned in the introduction that was previously submitted for my MPhil thesis is clearly indicated.

In accordance with the guidelines of the Degree Committee of the School of Biological Sciences, this thesis is does not exceed 60,000 words.

Signed:_____

Date:_____

Sarah Katherine Foster

Cambridge

SUMMARY

During development, neurons extend long axons which must navigate towards specific synaptic targets in the brain. This navigation is accomplished by a sensorimotor apparatus called the neuronal growth cone, located at the tip of the growing axon. Growth cones rely on signals present in their environment to navigate. Previous research has primarily examined how growth cones sense and respond to chemical guidance cues. However, the nervous system presents a rich and varied mechanical environment, and neuronal growth cones also respond strongly to physical stimuli.

Previous work from the Franze research group identified that tissue stiffness and the mechanosensitive ion channel Piezo1 are important for proper pathfinding of the axons of retinal ganglion cell neurons (RGCs). In an *in vitro* culture system comprising explanted *Xenopus laevis* eye primordia, I found that application of the Piezo1 agonist Yoda1 triggered axonal calcium transients in RGC axons, while Piezo1 knockdown with an antisense morpholino resulted in increased axonal outgrowth.

This mechanosensitive ion channel-dependent modulation of intracellular calcium, which is a crucial second messenger in many chemical signalling pathways, indicated that piezo1 signalling may significantly impact the response of growth cones to chemical signals. I therefore used compliant polyacrylamide hydrogels of defined stiffness to control the mechanical environment of RGCs *in vitro*, and studied if the mechanical environment of neurons impacts their response to Semaphorin 3A (Sema3A), a highly conserved guidance molecule that classically functions as a chemorepellant in this system.

Indeed, I found that the response of *Xenopus* RGC growth cones to Sema3A was significantly reduced on softer substrates. This dramatic change in the response to Sema3A indicated that substrate stiffness may strongly and chronically alter biochemical components that act downstream of chemical guidance cue receptors. In order to test this hypothesis, I used a variety of imaging and perturbation approaches to examine the dependence of critical regulators of the Sema3A response, including cyclic nucleotides, calcium, and resting membrane potentials, on the stiffness of the neuronal environment. CGMP levels were elevated, calcium flickers more dynamic, and resting membrane potential more depolarized in neurons grown on soft, as compared to stiff, substrates. Given what is known about the activity of these second messengers in the Sema3A signalling cascade, each of these changes is consistent with the less repulsive response to Sema3A observed in the soft condition.

Piezo1 is thought to be activated by high lateral membrane tension, and membrane tension is presumed to correlate with increased substrate stiffness. In collaboration with Jeffrey Mc Hugh in Ulrich Keyser's group at the Cavendish Laboratory, I used optical tweezers to measure membrane tension in neurons grown on soft and stiff substrates by pulling membrane tethers from axons. We found no difference in bulk membrane tension as a function of substrate stiffness, while easy sliding of the tethers along axons indicated low membrane-cytoskeletal coupling on all substrates studied. Thus, while Piezo1 is critically involved in neuron growth and pathfinding, variations in substrate stiffness do not seem to invoke changes in membrane tension, suggesting that Piezo1 activity is modulated differently than currently thought.

Taken together my results indicate that substrate stiffness is a critical variable in determining how growth cones respond to chemical guidance cues, and that cells integrate chemical and mechanical signals. I have identified several second messengers upon which Sema3A signalling and mechanotransduction cascades converge. Importantly, these second messengers are also master regulators of numerous other axon guidance cue responses (such as netrins and ephrins), and more generally of a wide variety of crucial biochemical signalling cascades. Variations in local tissue mechanics occur naturally during development and disease states, and could therefore be important in determining cellular responses to chemical signals during these pivotal events.

ACKNOWLEDGEMENTS

My sincere thanks are due to my supervisor, Kristian for making this project possible, for his invaluable scientific advice and encouragement, and for his refreshing and consistent optimism. Kristian is not only dedicated to helping his students achieve academic success but also to ensuring that they are able to live a happy and balanced life while doing so. I am very lucky to done my PhD with a supervisor who cares deeply about the welfare of his students.

-

And also to the lab-mates, collaborators, and mentors who have provided encouragement, and inspiration:

My advisor Prof Christine Holt, for being an inspiring scientist, and for many useful scientific discussions.

The whole Harris/Holt lab for their immense generosity in sharing equipment and knowledge, and especially Roberta Cagnetta, Hovy Wong, Julie Qiaojin Lin, and Asha Dwivedy.

Members of the Franze Lab, past and present have been a wonderful and entertaining group of people to work with, as well as a source of exciting scientific advice and ideas:

Julia Becker, Lars Bollman, Alejandro Carnicer-Lombarte, Andrea Dimitracopoulos, Ivan Dimov, Hélène Gautier, Ryan Greenhalgh, Max Jakobs, Eva Kreysing, Katrin Mooslehner, Eva Pillai, Rasha Rezk, Johannes Rheinlander, Rajesh Shahapure, Jana Sipkova, Vanesa Sokleva, Isabel Weber, Liz Williams, Omer Wagner, Alex Winkel

Particularly the other 'frog people' for innumerable instances of help with embryo care.

Joy, Eva P, and Julia for generously volunteering their time to proofread sections of this thesis.

Liz Williams for keeping the lab running smoothly, for many entertaining and refreshing early morning coffee chats, and for keeping my plants alive while I was away writing this thesis.

Jeff Mc Hugh, Kurt Andresen and Mus Çağlar for being wonderful, fun collaborators.

Phil Nelson for continuing to be a kind and supportive mentor.

-

And thanks are also do to all the wonderful people outside the world of science who offered support, friendship, and perspective:

My parents, who made many sacrifices to ensure that their children were able to get the best education possible.

My brother Andrew and my sister Elizabeth for being amazing and inspiring siblings.

Kate, Mark, and Rachel for helping me to find a home away from home in Cambridge; Rosaline, Lucky, and Danica for their continued friendship; and Sagrario, at whose beautiful home most of this thesis was written.

-

This thesis was possible thanks to the generous funding of the Herchel Smith Foundation.

CONTENTS

List of Tables

List of Figures

List of Abbreviations and Acronyms

AFM	**Atomic Force Microscope**
B	Bending rigidity
BM	Blastomere
CAM	Cell Adhesion Molecule
conA	concanavalinA
CNGC	Cyclic Nucleotide Gated Calcium Channel
CNS	Central Nervous System
CPI	Calpastatin Peptide Inhibitor
CSPG	Chondroitin Sulfate ProteoGlycans
D	Dalton
DCC	Deleted in Colorectal Cancer
cAMP	Cyclic Adenosine Monophosphate
cGMP	Cyclic Guanosine Monophosphate
E	Young's modulus
ECM	Extracellular Matrix
F-actin	Filamentous actin
FAK	Focal Adhesion Kinase
FARP2	FERM, ARH/RhoGEF, And Pleckstrin domain Protein 2
FGF(R)	Fibroblast Growth Factor (Receptor)
G',G''	Sheer storage (') and loss ('') moduli
GAP	GTPase Activating Protein
GECI	Genetically Encoded Calcium Indicator
GEF	Guanine nucleotide Exchange Factor
k	Spring constant

K	Reduced apparent elastic modulus
KD	Knockdown
(Q)ICC	(Quantitative) Immunocytochemistry
IG	Immunoglobulin
MAP(s)	Microtubule Associated Protein(s)
MBS	Modified Barth's Saline
MO	Morpholino
MPD	Membrane Potential Dye
MSC	Mechanosensitive Ion Channel
Npn1	Neuropilin-1
NFPC	NF-protocadherin
ODQ	1*H*-[1,2,4]Oxadiazolo[4,3-*a*]quinoxalin-1-one
OT	Optic Tract
PAA	Poly-acrylamide
Pa	Pascal
PBS	Phosphate Buffered Saline
PlxA(1,2,..)	Plexin A (1,2,…)
RGC	Retinal Ganglion Cell
RGD	Arginine-Glycine-Aspartate
RNA	Ribonucleic Acid
Robo	Roundabout
ROI	Region Of Interest
RPE	Retinal Pigmented Epitheli(a/um)
Sema3A	Semaphorin 3A
SGC	Soluble Guanylyl Cyclase
Shh	Sonic hedgehog

SNARE	SNAp (Soluble N-ethylmaleimide-sensitive factor Attached Protein) REceptor
T	Effective membrane tension (= T_m +γ)
***t*-BOC**	7-Amino-4-Chloromethylcoumarin, *t*-BOC-L-Leucyl-L-Methionine amide
TRPC	Transient Receptor Potential Channel
TMR	Tetra-Methyl Rhodamine
T_m	Lateral bilayer tension
Unc	Uncoordinated
γ	Membrane-cytoskeleton adhesion energy
γ_p	Poisson's ratio
Ions: Ca^{2+},K^+,Na^+	Divalent calcium ion, monovalent potassium ion, monovalent sodium ion
Units: p, n, µ, m, c, M, G	pico-, nano-, mico-, milli-, centi-, mega-, giga-

List of Appendices

1 INTRODUCTION

1.1 Axon growth and the neuronal growth cone

The brain is our most complex organ. Its main function is to process and transmit information. The conduits that carry information throughout the brain and body are called axons. These neuronal projections act like wires to transmit electrical signals over sometimes immense distances throughout the body. The formation of networks of precisely connected neurons is a fundamental event during development. It relies critically on the correct navigation of growing axons through the developing brain or central nervous system (CNS) to their synaptic targets. A failure of this process can be catastrophic, and axon pathfinding errors have been linked to numerous human developmental disorders[1,2]. The growth trajectory of pathfinding axons is determined by a host of environmental cues: chemical signals present in surrounding tissues provide a complex suite of growth promoting or inhibiting, and repulsive or attractive signals; and the axon is also exposed to an immensely complex and rapidly changing substratum. To confront this navigational challenge, developing axons are equipped with a specialised sensory-motor apparatus called a growth cone.

1.1.1 The neuronal growth cone: growth and motion

Growth cones were first identified by Santiago Ramón y Cajal in 1890[3,4], and already in 1914 Ross Harrison appreciated their critical physical role in axon outgrowth, writing that "the active factor in the spinning of the nerve fiber is a small mass of amoeboid protoplasm at the end of a cell processes"[5].

Growth cones are now recognized to be exquisitely complex and sensitive apparatuses for growth cone steering and navigation. As they must operate, in many cases, long distances away from the cell body, growth cones function largely autonomously of the nucleus, at least on the timescales relevant to axon guidance. To enable their complex computational and motor function, growth cones are equipped with endoplasmic reticulum[6], mitochondria[7], and the machinery to enable translation alongside a complex suite of mRNA molecules[8,9].

Of particular and fundamental importance is the growth cone's unique cytoskeletal architecture, represented in Figure 1.1. In the following section I will introduce some of the critical features of the growth cone cytoskeleton, which are reviewed in in more detail in References [10–13].

Growth cones can be thought of as comprising a few distinct structural domains[11,14]. The axon shaft immediately preceding the growth cone is characterised by tight bundles of polarized, collinear microtubules, which facilitate directed transport along the axon shaft[15,16]. On entering the growth cone, these microtubules begin to unbundle and splay out[7,17].

The 'central zone' is a thicker region of the growth cone that is enriched in vesicles and mitochondria[7]. The central zone cytoskeleton is characterised by a population of stable microtubules, and is relatively actin-poor compared to the rest of the growth cone[11,14].

The thin region dividing the central zone from the growth cone periphery is called the transition zone. The transition zone is enriched in contractile myosin II[18]. In some cases, 'actin arcs', curved F-actin bundles approximately parallel to the growth cone leading edge, have been observed in the transition zone. These are thought to be important in constraining and stabilizing the central domain microtubule population[19].

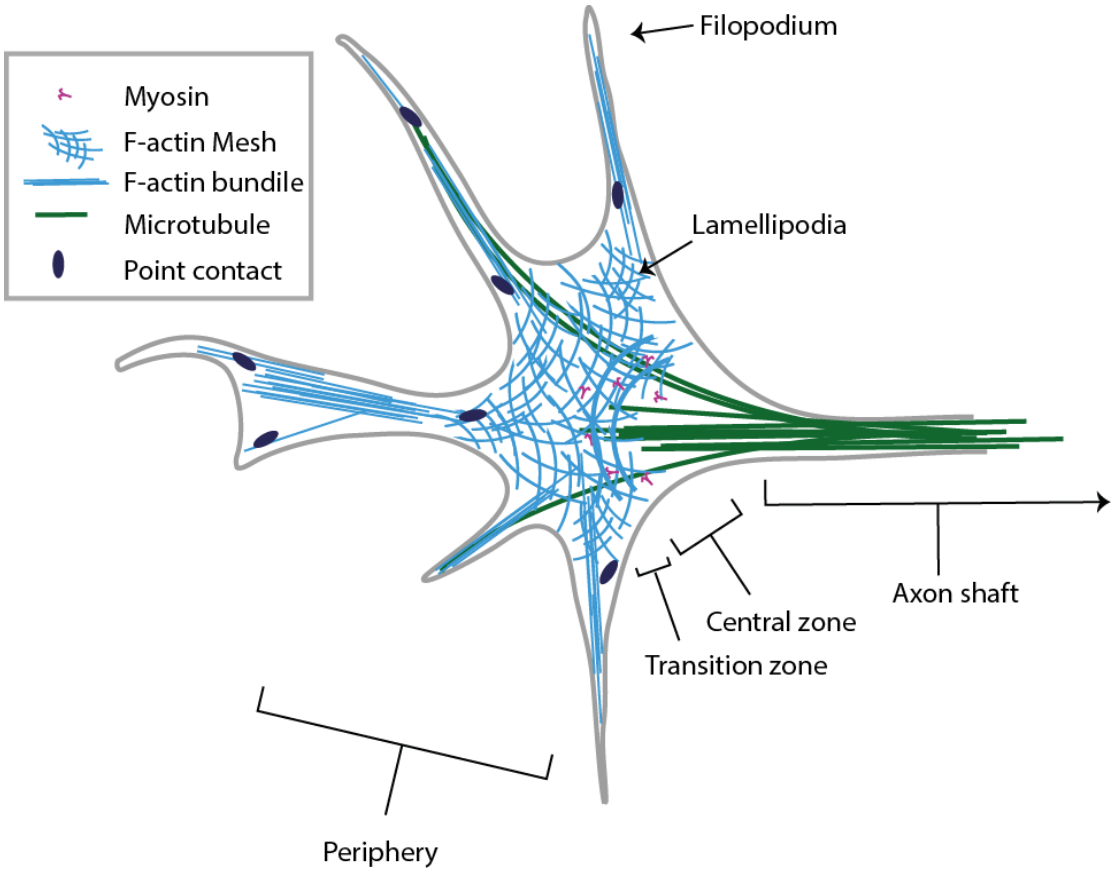

Figure 1.1: Cytoskeletal ultrastructure of the neuronal growth cone

The structure of a neuronal growth cone. Growth cones are typically divided into several regions that can be distinguished by their cytoskeletal components. From left: the distal lamellipoda and filopodia characterized by filamentous actin (F-actin) organised into a polarized meshwork or thin bundles, respectively, comprise the peripheral domain; the narrow transition zone separates the peripheral and central regions and is enriched in myosin motors and arc-like F-actin bundles; the central domain is characterized by the presence of organelles (not shown) and a population of stable microtubules.

The transition zone gives way to the thin (often less than 100 nm[20]) peripheral domain, which comprises two main elements: sheet-like lamellipodia that is characterized by a dynamic actin meshwork, and thin filopodia whose structure is dominated by tightly bundled collinear actin filaments. These distinct actin structures result from the presence of different actin nucleating and bundling proteins. Lamellipodia is enriched in the branch-inducing Arp2/3 complex (which however may also play a role in filopodia initiation)[21,22], and bundling proteins such as fascin are critical for filopodia[23]. Dynamic microtubules also extend into the growth cone periphery, often looping, and frequently entering filopodia. Interactions between actin bundles and dynamic microtubules in the periphery are critically important for proper growth cone navigation[7,12,17,24].

This cytoskeletal edifice is intensely dynamic. The actin network in the periphery undergoes retrograde flow: actin polymerizes at the leading edge of the growth cone,

against the barrier created by membrane tension; at the same time, myosin II exerts contractile forces to pull the meshwork back, leading to continuous 'actin treadmilling'[18,25,26].

Growth cones assemble small integrin-containing adhesion complexes known as point contacts that are similar to immature focal adhesion complexes[27]. By transforming these internal actin-generated forces into traction forces exerted on the substrates[28], Point contacts provide a 'clutch' to convert actin retrograde flow into forward motion[29].

While actin is considered the primary 'motor' of the growth cone, microtubule mediated sliding or protrusive forces can also play a role in driving forward motion of the growth cone[30]. Indeed, studies with agents that inhibit cytoskeletal dynamics have repeatedly shown that while growth cones require actin dynamics for pathfinding, they are not required for outgrowth[24,31].

1.1.2 Morphological diversity of growth cones

Most models of neuronal growth and pathfinding have imagined growth cones as the flat, spread structures like that in Figure 1.1; however, *in vivo* and *in vitro*, growth cone morphology can diverge significantly from this archetype (Figure 1.2). Elegant early studies from Bill Harris and Christine Holt imaged individual retinal growth cones traversing the optic pathway of embryos of the frog *Xenopus laevis*, and found a rich variety of morphologies. At many points in the optic pathway growth cones had a much simpler, more club-like, and less flattened morphology than that typically observed on glass culture substrates *in vitro*[32]. Early electron microscopy studies of *Xenopus* Rohnan-Beard neurons show similar morphologies[33]. Additionally growth cone morphology is highly dynamic and context specific; for example, both *Xenopus*[32] and mammalian[34] retinal ganglion cells (RGCs) tend to assume a small streamlined morphology during spurts of rapid growth, but slow down and 'pancake' at critical points during their navigation.

Thus it is possible that some structures and patterns of motility observed *in vitro* are artefacts of this continuous, flat, sheet-like lamellipodia which often seems not to exist in the same form *in vivo*. Further studies will be needed to elucidate more precisely how growth mechanisms determined *in vitro* translate to the *in vivo* situation.

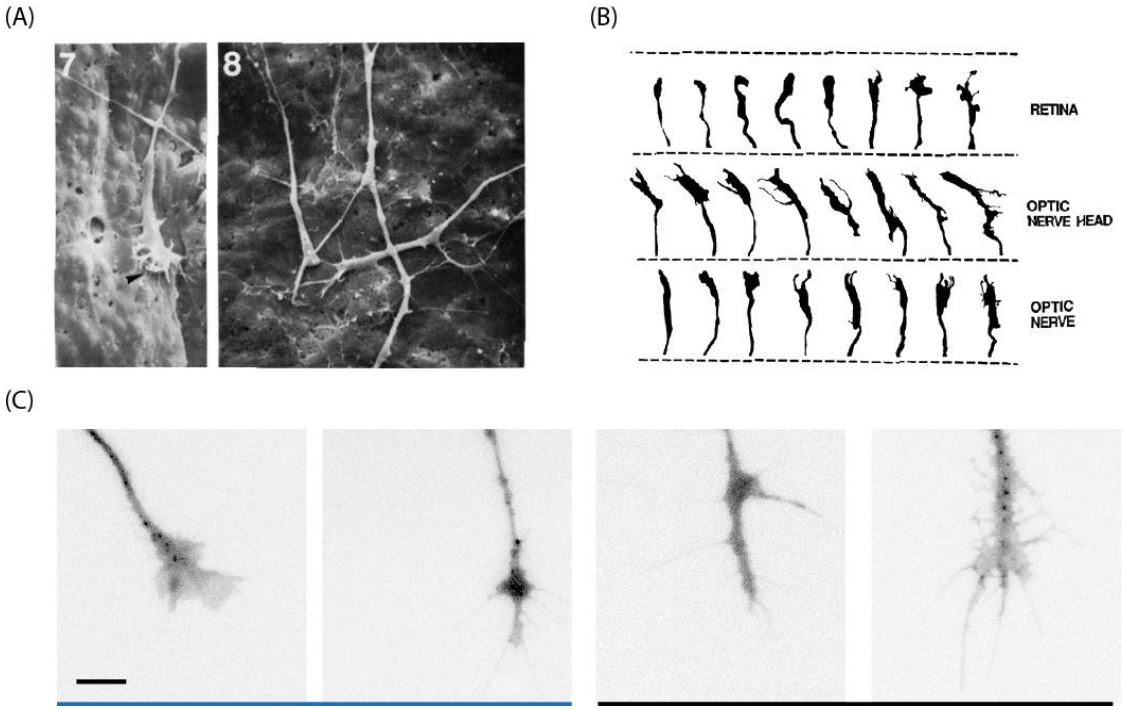

Figure 1.2: Growth cone morphological diversity

Growth cone morphologies may diverge considerably from that shown in (Figure 1.1). (A) Scanning electron micrographs of Xenopus sensory neurons in the developing embryo. Growth cones appear more 'club-like', and do not seem to have large spread filopodia; reproduced from[33]. (B) Sketches made from labelled retinal growth cones at different points in the Xenopus optic pathway; reproduced from[32]. Growth cone morphology varies between different points in the optic pathway, and there is considerable morphological variation even among growth cones imaged as they traverse the same location in the optic pathway. (C) Even in very controlled 2D in vitro conditions, there is considerable morphological diversity: four Xenopus retinal growth cones from experiments completed for this thesis grown on soft (two left, blue line) or stiff (two right, black line) hydrogel substrates. Growth cones were filled with a fluorescent dextran to facilitate imaging, and images have been inverted. Scale bar is 10 µm.

1.1.3 The neuronal growth cone: chemical guidance

Growth cones possess a diverse collection of receptors for chemical signals that provide repulsive or attractive signals to direct neuronal growth, as well as providing instructions for critical morphological changes such as branching and fasciculation[35]. These signals are called chemical guidance cues.

Guidance cues are generally proteins present in the environment either bound to the substrate, or secreted by neighbouring cells. Four canonical groups of ligand/receptor pairs play crucial roles in nervous system development, semaphorins and the plexin receptors, ephrins and the eph receptors, netrins and the deleted in colorectal cancer (DCC) or UNC5 receptors, and slits and their robo receptors[36–38]. An increasingly diverse

set of molecules with well characterised functions in other pathways have been found to also exert guidance effects on neurons, including morphogens such as sonic hedgehog[39] and fibroblast growth factor[40] , and components of adhesion complexes such as N-cadherin and integrins[41].

While initially guidance cues were categorized as 'repulsive' or 'attractive' (or 'collapsing' or 'growth promoting'), it was soon discovered that growth cones have a remarkable ability to adapt their response to the same guidance cue based on external conditions (i.e. which adhesion molecules the growth cone encounters), and/or the growth cone's internal state (i.e. levels of critical second messengers). This plasticity provides a critical level of regulation to guidance cue responses.

Figure 1.3 illustrates some of the common motifs relating to guidance cue signalling cascades. For many classical guidance cues, the directionality of the response is controlled by the elevation of critical second messengers that act in the first stages of the response. The initial response to many guidance cues involves an elevation of either cAMP or cGMP. This cyclic nucleotide elevation is followed by an influx of calcium, and level of this cyclic nucleotide elevation (or the cAMP/cGMP ratio in the case of netrin-1) is critical for determining the nature of the subsequent calcium influx. The calcium influx in turn determines the directionality of the growth cone response, with larger elevations typically corresponding to attractive responses and smaller elevation to repulsive responses. Thus cyclic nucleotide levels[42,43] and calcium levels [44–46] are 'master regulators' which can in many cases be manipulated to switch an attractive response to a repulsive one, and vice versa.

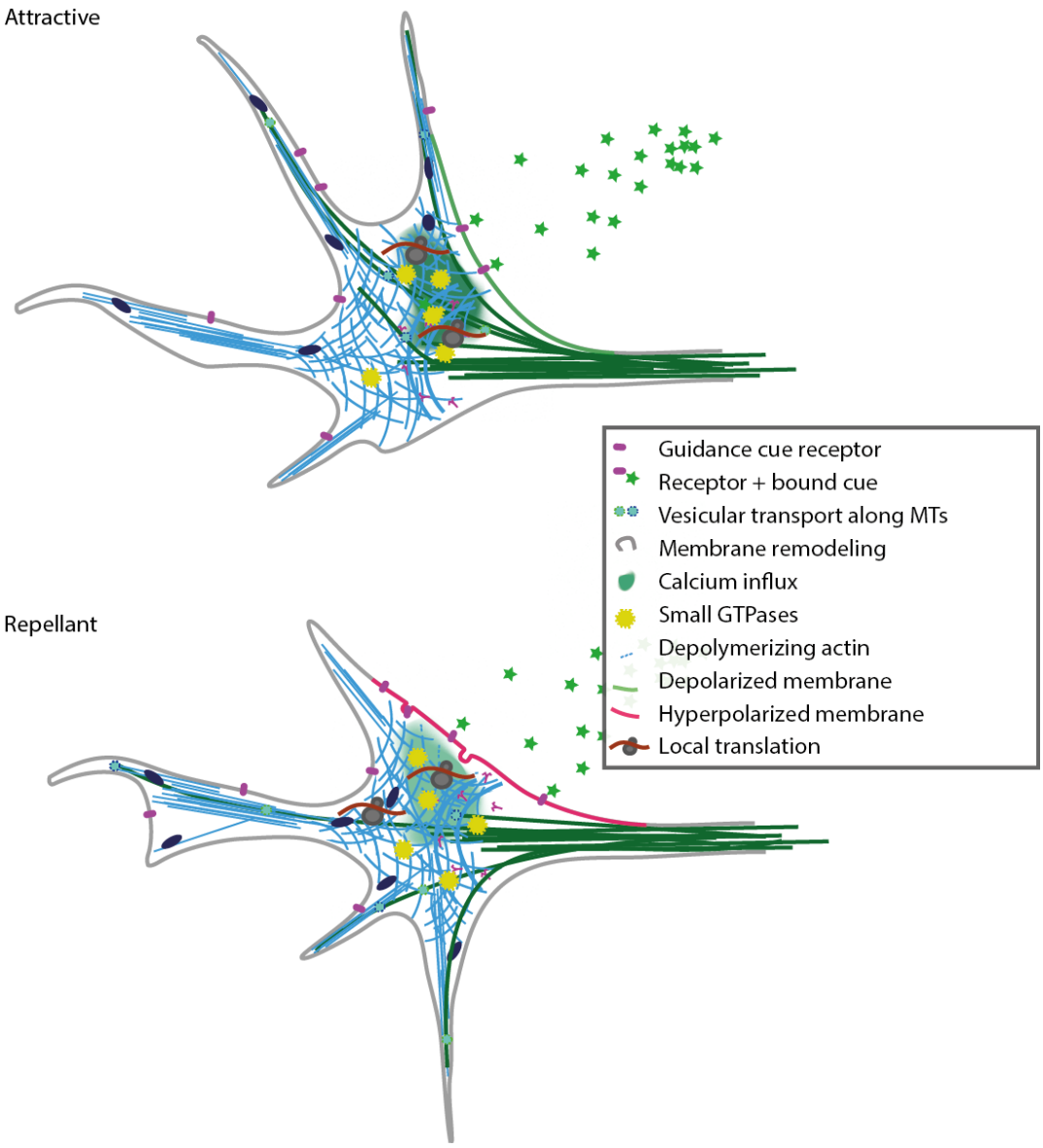

Figure 1.3: Common components of axon guidance cue signalling cascades

Asymmetric stimulation with a guidance cues may trigger an attractive or repulsive signalling cascade. In the cartoon the cue (green stars) is present in a gradient with its source somewhere to the upper right. Cue molecules engage receptors (purple ovals) on the 'top' side of the growth cone. Generally, attractive cues result in membrane depolarization (green membrane), while repulsive cues result in membrane hyperpolarization (magenta membrane)[47–49]. In many cases this localized membrane potential change results from cyclic nucleotide signalling (not shown). Calcium enters the cell downstream of the membrane potential change, with attractive cues typically inducing a larger calcium influx[42,44,45,48]. Attractive cues can promote vesicle movement along microtubules, while repulsive cues inhibit this process[50]. Repulsive cues cause disassembly of the actin meshwork via depolymerisation and reduction in membrane area via endocytosis[51–54]. Much of the crucial downstream cytoskeletal modulations occur via activation of small GTPases, which occurs in a complex and pathway dependent manner, reviewed in Reference [47]. Finally, both attractive and repulsive cues regulate local translation[9].

Downstream of these initial signalling events, guidance cues affect cytoskeletal dynamics and organization in order to induce morphological changes. Actin treadmilling keeps the

growth cone primed to respond quickly to any perturbations and contributes to its exquisite sensitivity and fast responses. In many cases guidance-cue dependent modulation of the cytoskeleton is mediated via small GTPases, molecular switches that cycle between active GTP bound and inactive GDP bound states[55] (See inset, Figure 1.5). In particular Rho and Ras are crucial regulators of cytoskeletal and adhesion dynamics downstream of axon guidance cues[47,56,57].

Microtubules also play critical roles in axon guidance[58], indeed polarized invasion of dynamic microtubules into the growth cone periphery is sufficient to cause directional motion, and inhibiting vesicular transport along microtubules can abolish the turning response to at least some guidance cues[50,59,60].

Finally, growth cones contain a complex suite of mRNAs[61], as well as the molecular machinery needed for protein translation and degradation[62]. Axon guidance cues induce rapid restructuring of the local proteome. The lab of Christine Holt demonstrated in 2001 that blocking translation inhibited both repulsive and attractive turning[63]. A number of critical locally translated proteins have since been identified, including, for example β-actin following netrin-1 stimulation[64], or RhoA following Sema3A simulation[56]. More recently, elegant high-throughput proteomic studies, also from the Holt lab, have identified a complex suite of proteins whose translation is up or downregulated in response to chemical guidance cue stimulation[9]. Cagnetta et al., observed profound and cue-specific restructuring of the axonal proteome within five minutes of cue stimulation. This dataset also revealed some unexpected results, such as the upregulation of histone H4 following Sema3A stimulation, suggesting that much remains to be discovered about the complex regulation of growth cone guidance[9].

1.1.4 Semaphorin3A

Semaphorins are a diverse group of proteins with over 20 members. They are divided into seven families based on structural differences, but all contain a structural unit called a sema domain[65]. Though first discovered for their role in axon guidance[66,67], semaphorins are now known to act as crucial signalling molecules in a wide variety of contexts throughout the body[68].

In this thesis I studied growth cone responses to Sema3A, a class 3 secreted Semaphorin. Sema3A was first identified by the Raper lab in 1993. It was initially named collapsin, for its ability to cause reversible growth cone collapse and retraction[66], and it was soon found that asymmetric contact of growth cones with Sema3A resulted in repulsive turning

in vitro[69]. In this section I will describe what has since been discovered about the Sema3A receptor complex and signalling cascade.

The Sema3A signal is received by an obligate co-receptor complex consisting of neuropilin-1 (Npn1) and an A-type plexin (PlxA, in the later discussion of the Sema3A signalling cascade, I will discuss mainly PlxA1)[70,71]. The active unit of Sema3A is a dimer[72], which binds a receptor comprising two molecules each of Npn1 and PlexA[71]. Npn1 has a very small cytoplasmic domain, and in fact growth cone collapse in response to Sema3D requires only the extracellular part of Npn1[73]. The extracellular portion of Npn1 however, is required for structural stability of the receptor complex[74]. Plexins in contrast contain a large, highly conserved signalling intracellular region, as well as an extensive extracellular portion. The latter includes a sema domain, which interacts with the sema domain in Sema3A[71,75].

In addition to PlxA/Npn1, the Sema3A holoreceptor can also include the cell adhesion molecule L1Cam[52,76,77] (discussed more in Section 7.5.1). Other discretionary receptor components have been suggested which may play key regulatory roles in the Sema3A response (reviewed in References [68,78]).

Sema3A binding induces an elevation of intracellular cGMP. Several studies suggest that this proceeds via local activation of the soluble guanylyl cyclase (sGC): in cerebral basket cells, where Sema3A regulates branching, Sema3A was found to induce trafficking of sGC to the membrane to enable localized cGMP elevations[79], and in cortical apical dendrites different levels of sGC in different cellular compartments determine the polarity of the Sema3A response[80].

In the case of a repulsive response, this cGMP elevation leads to subsequent membrane hyperpolarization, which is likely mediated by chloride channels. In the case of an attractive response it leads to membrane depolarization likely mediated by sodium channels. An influx of calcium into the growth cone follows in both cases, though the magnitude is greater in the case of an attractive signal[48].

In the case of an attractive response, membrane depolarization likely facilitates calcium influx via voltage gated calcium channels, as has been shown explicitly for other attractive guidance cues[42,45]. CGMP-gated cyclic nucleotide gated calcium channels (CNGCs) have been strongly implicated in repulsive Sema3A signalling[81] . However, the exact relationship between cGMP and calcium in the Sema3A response is not yet clear. Lipid rafts are essential for Sema3A signalling transduction[82], and clustering of signalling

components such as sGC and CNGCs into spatially segregated lipid domains together with Sema3A receptor complexes may be important. The relationships among calcium, cGMP, and membrane potential are outline in Figure 1.4.

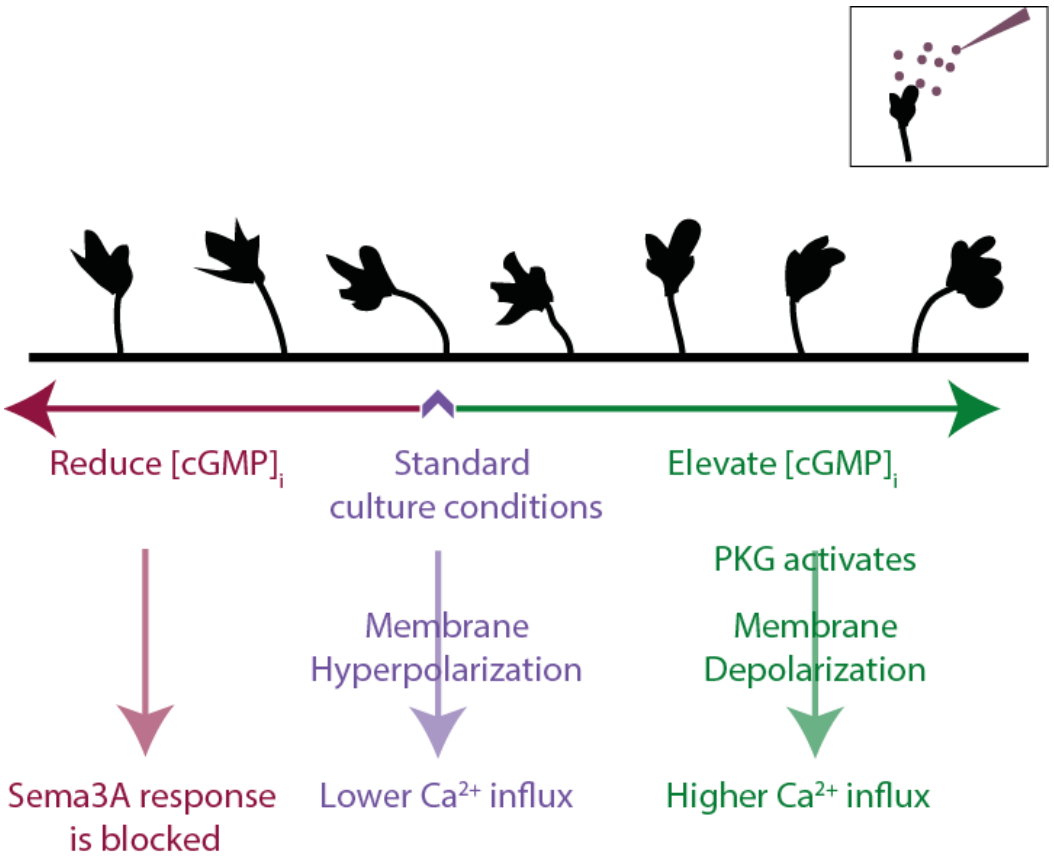

Figure 1.4: Relationships between cGMP, membrane potential, and calcium influx in the Sema3A response

Cartoons indicate growth cone responses to asymmetric stimulation with Sema3A from the top right (see inset). Under standard in vitro culture conditions (purple arrow), the Sema3A response is strongly repulsive, causes membrane hyperpolarization, and a subsequent influx of calcium. If cGMP is pharmacologically reduced (red arrow), cells cease to respond to Sema3A. In contrast if cGMP is elevated (green arrow), PKG activates, inducing membrane depolarization and a larger calcium influx. This figure is based largely on the results demonstrated by Nishiyama et al. [48].

Downstream of these initial signalling events, Sema3A alters cytoskeletal and membrane dynamics. I will not attempt to catalogue every known step in the Sema3A signalling cascade, but instead will describe a few crucial mechanisms by which Sema3A impacts growth cone morphology. The Sema3A signalling cascade is reviewed more exhaustively in References [68,83]. As discussed, Sema3A can function either as an attractive or a repulsive cue depending on environmental conditions and the biochemical state of the growth cone[48,84], and also plays a role in axonal branching where it can similarly promote[79] or inhibit[85] branching. However, as Sema3A was initially characterized as a

collapsing agent and a chemorepellant, and as this seems to be its activity under the most common *in vitro* culture conditions, research into Sema3A's signalling cascade has focused on its repulsive activity. Thus, the signalling pathways discussed here were, for the most part, discovered using Sema3A as a collapsing agent or repellent. (Collapse and repulsion are generally considered to be a very similar response, with the main difference being whether the stimulus was applied globally or asymmetrically)

1.1.4.1 Sema3A affects endocytosis, adhesion, and actin dynamics via complex interactions with small GTPases

Sema3A dramatically restructures growth cone actin[53,86], alters cell adhesion, and induces large scale endocytosis[53]. Much of this regulation proceeds via the activity of small GTPases, reviewed in References [55,87]. The following section will discuss several of the ways in which Sema3A signalling is known to alter the activity of Rho and Ras GTPases to produce its effects on cell morphology and motility. A visual summary of the mechanisms discussed here is presented in Figure 1.5.

A guanine nucleotide exchange factor (GEF) called FARP2 (FERM, RhoGEF and pleckstrin domain-containing protein) is recruited to PlexinA1/Npn1 complexes. Upon Sema3A binding the receptor complex, FARP2 dissociates and activates the Rho family GTPase Rac[88]. Rac plays a role in stimulating endocytosis during Sema3A mediated growth cone collapse[51], and in fact, inhibition of Rac signalling blocks collapse[89].

The conserved intracellular domain of PlxA1 contains a functional GTPase activating protein (GAP) homology domain which acts as a Ras GAP[90]. The GAP activity of PlxA1 relies on the Rac activation described above, and the subsequent association of another Rho family GTPase called Rnd1 with PlxA1[88]. PlxA1's GAP activity reduces R-Ras activity by causing R-Ras to revert to its inactive, GDP bound state. As R-Ras is a potent integrin activator[91], the net result is likely decreased adhesion.

The series of associations of various small GTPases with the Sema3A receptor complex also relate to conformational changes of PlxA1, this has not been discussed here, but is reviewed in the articles mentioned above.

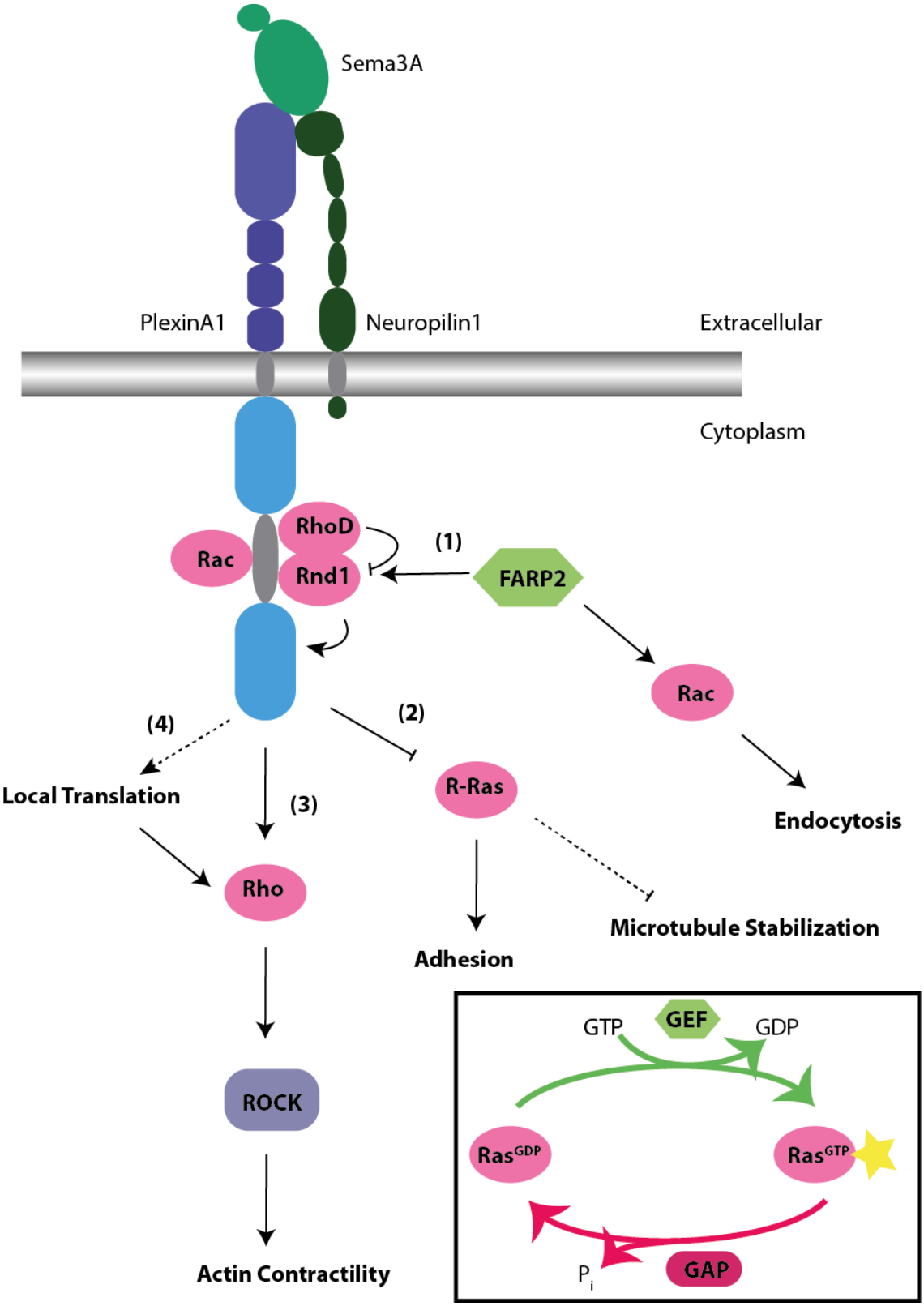

Figure 1.5: Small GTPases in Sema3A signalling

Figure 1.5: (continued)

This figure is based on Figure 4 from Reference [55] and Figure 2 from Reference [87], with some modifications. Note that although one copy of Sema3A, Npn1, PlxA1 are shown in the cartoon, in reality at least two copies of each are present in a functional, activated, holoreceptor complex. Rho, Rac, and Rnd can all physically associate with the PlxA1 intracellular domain. (1) Upon Sema3A binding, FARP2 dissociates from the PlxA1/Npn1 complex and activates Rac (2) FARP2 dissociation facilitates Rnd1 association with the receptor which in turn enables the intrinsic Ras GAP activity of PlxA1. Another small GTPase called RhoD may antagonize Rnd1 signalling in this context[92]. The net effect is reduced R-Ras activity which in turn results in reduced adhesion, and may also alter microtubule stability in a GSK-3 dependent manner[93]. (3) PlxA1 activates Rho, and (4) RhoA is also locally translated downstream of Sema3A signalling. Rho activation stimulates actin contractility. Inset box: small GTPases (Ras in this example) cycle between an active, GTP-bound state and an inactive, GDP-bound state, facilitated by the activity of guanine nucleotide exchange factors (GEFs) and GTPase activating proteins (GAPs). In the GTP bound active conformation small GTPases can interact with various effectors (yellow star). Inset based on Reference [55].

Finally, protein synthesis is induced within minutes of Sema3A stimulation, and blocking protein synthesis abolishes the Sema3A response[63]. RhoA, best known for regulating actin contractility via the Rho-associated protein kinase ROCK, is one of the critical effectors that is locally translated downstream of Sema3A[56].

While it is likely that not all of these pathways are active in every context in which Sema3A functions, small GTPases provide a versatile and robust way for Sema3A signalling to adjust growth cone morphology and dynamics. In the following two sections I will discuss in a bit more depth the mechanisms by which Sema3A induces membrane restructuring and modulates growth cone adhesion.

1.1.4.2 Sema3A induces membrane restructuring

Membrane restructuring is critical for the large scale morphological changes induced in response to guidance cues. As eluded to in Section 1.1.4.1, Sema3A induces localised endocytosis, and in fact inhibition of clathrin-mediated endocytosis abolishes the (repulsive) Sema3A response[54]. Endocytosis is necessary for repulsive turning, but also may play another important role in the temporary desensitization of growth cones to Sema3A, as the Sema3A receptor complexes are transiently and specifically internalized by endocytosis following the Sema3A stimulus[94].

Additionally, the cyclic nucleotide and calcium elevations that occur downstream of most guidance cues may alter transport of exocytotic vesicles along peripheral domain microtubules, which is important for membrane restructuring in response to both attractive and repulsive signals[50,60]. In particular, repulsive cGMP signals, such as that observed in the Sema3A response were found to locally inhibit microtubule-mediated transport of VAMP7 (Vesicle-associated membrane protein 7)-containing vesicles,

resulting in an asymmetric distribution of microtubule protrusion and exocytosis biased towards the side of the growth cone distal to the cGMP influx[50].

1.1.4.3 Sema3A alters adhesion

Repulsive growth cone turning requires disassembly of growth cone adhesions on the side of the growth cone proximal to the Sema3A stimulus. As with the other facets of Sema3A signalling, Sema3A can affect adhesion via multiple mechanisms.

As previously mentioned (1.1.4.1), R-Ras is directly inhibited by the Ras GAP activity of PlxA1. R-Ras activates integrin signalling and suppression of R-Ras signalling thus serves to weaken cell adhesion[91].

Additionally, FARP2, which activates Rac in response to the Sema3A signal, may play another role in adhesion: FARP2 can physically associated with PIPKIγ661 (phosphatidylinositol phosphate kinase type 1 isoform) and sequester it away from talins[88]. Talins are critical adhesions complex proteins that help link integrins to the cytoskeleton. Among other activities, PIPKIγ661 is implicated in the correct localisation of talin to focal adhesion complexes[95].

Sema3A also activates the protease calpain[96,97], which can subsequently promote point contact turnover by cleaving point contact components such as talin and focal adhesion kinase (FAK)[98,99].

Finally, as will be discussed in the context of RGC axon pathfinding later (Section 1.2.2), Sema3A signalling can stimulate adhesion by directly inducing the local translation of the cell adhesion molecule NF- protocadherin (NFPC)[100]. This highlights the complexity and specificity of the Sema3A response, as it indicates that Sema3A may simultaneously inhibit certain types of adhesion while encouraging others.

1.2 The *Xenopus* retinotectal system

I studied Sema3A responses in retinal ganglion cell (RGC) neurons of embryonic *Xenopus laevis* frogs. The *Xenopus* retinotectal pathway is an excellent system for the study of axon growth during development. As amphibians develop ex-utero, the growth of these axon tracts can be visualized *in vivo* in the developing embryo (Figure 1.6 and Reference [101]). For my experiments, I used a corresponding *in vitro* culture system: if eye primordia are explanted from the embryo and placed onto a growth-permissive substrate, RGCs still exit the eye primordium and grow out across the substrate (See for example Figure 1.8A for images of RGC axons in culture). In the following sections I will describe

the *in vivo* path taken by these neurons, and then briefly discuss what is known about axon guidance in the *Xenopus* retinotectal system.

1.2.1 *In vivo* path of RGC neurons

RGCs are born in the embryonic retina at around stage 24[102]. (All developmental stages mentioned in this thesis are based on the staging table to Nieuwkoop and Faber[103]; stage 24 corresponds roughly to one day post-fertilization if the embryo is kept at 24ºC.) Generally each RGC extends a single axon, though about 5% percent of RGCs send two independently navigating axons down the optic pathway[32]. This axon grows along the vitreal surface of the retina until reaching the optic nerve head (ONH), where it exits the eye and crosses into the brain. Upon reaching the optic chiasm, which occurs at about stage 32 of development, all RGCs cross to the contralateral brain hemisphere[101]. (In *Xenopus* tadpoles all RGCs cross at the optic chiasm, ipsilaterally projecting axons arise later in development as the frog undergoes metamorphosis and develops binocular vision[104,105].) RGCs then grow in a bundle across the brain, generally localised to a depth of within 10 µm of the surface[32]. This tract grows approximately straight until it makes a critical bend near the diencephalon/telencephalon boundary, and then grows straight once again until finally terminating at the optic tectum, where the axons splay out, branch, and undergo a complex process of topographic mapping[106]. The pathway taken by RGC axons and the locations of the anatomical signposts mentioned in the preceding paragraph are summarized in Figure 1.6B.

1.2.2 Axon guidance in the *Xenopus* optic pathway

Early studies in the *Xenopus* embryo strongly indicated the presence of diffusible cues capable of attracting RGC axons from afar. In the 1980's, Bill Harris found that when regions of the neurepithelia that underlies the optic tract were rotated by 90º, RGCs that grew over these rotated sections also turned by 90º, which strongly indicated that a local cue(s) present in the neuroepithelia was able to direct axon growth[107]. He also found that the ability of RGCs to navigate to the tectum was remarkably robust: some of these axons made a second turn to re-orient back to the tectum after their trajectory had been altered. Even more impressive, axons from eye primordia that had been dissected and then re-implanted a significant distance from their usual location were in many cases able to successfully navigate back to the tectum. This was despite the fact that they were not growing over tissue that normally formed part of the optic pathway. This striking result strongly suggested the presence of diffusible attractive chemical gradients[108].

An immense body of work (reviewed in part in Reference [37]) has since sought out these chemical signals, and has elucidated many aspects of the chemical regulation of axon growth and pathfinding in the *Xenopus* optic pathway. A full description of the chemical guidance cues that have been suggested to play a role in RGC guidance is beyond the scope of this introduction. Here I will describe some of the main cues that are known to direct RGC growth at critical choice points.

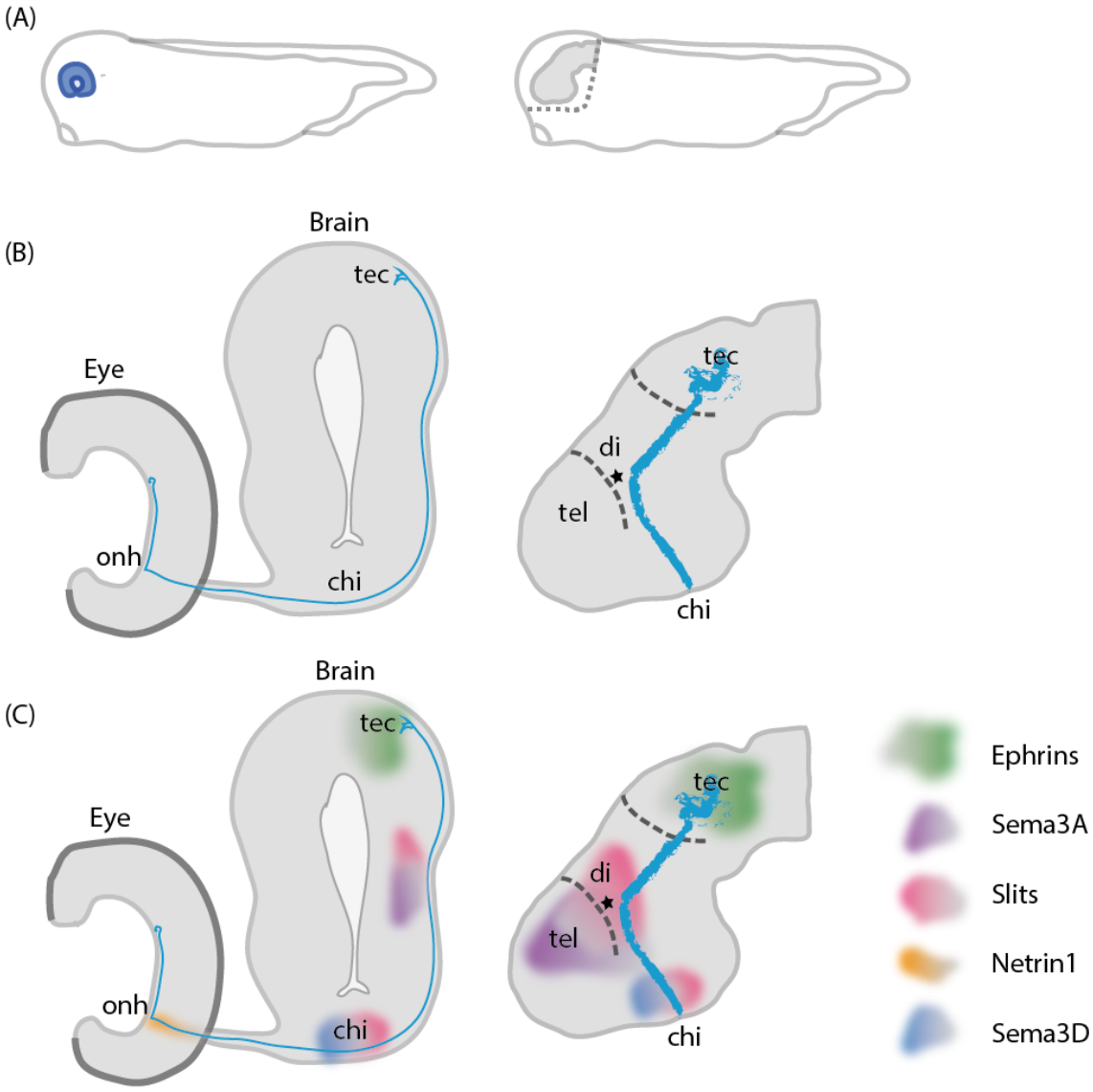

Figure 1.6: RGC growth and guidance in the Xenopus optic pathway

Figure 1.6: (continued)

RGC axons follow a stereotyped pathway during development, and numerous chemical guidance signals have been identified that contribute to establishing this growth pathway. (A) Two cartoons of the Xenopus embryo are shown. Left: intact embryo with the eye primordium in blue. Right: cartoon of an embryo in which one eye and the underlying skin and dura mater have been dissected away to expose the brain. (B) Cartoons of the Xenopus eye and brain indicating the path taken by RGC axons during development. Left: Cross section of the Xenopus brain, a single RGC axon is shown in blue (only one eye is shown for clarity). Right: a lateral view of the brain, showing the path taken by the optic tract across the brain surface. RGC axons (shown in blue) make a key bend in their trajectory at stage 35/36 (*) before reaching their destination in the optic tectum at around stage 39/40. Axon tracts are shown as they would look at stage 39/40, when most of the axons have completed their growth process. Cartoons are based on [101]. (C) The cartoons from (B) are reproduced to show the approximate localisation of critical axon guidance cues in the Xenopus brain. For a fuller description of the expected function of these cues, please see the text. onh: optic nerve head, chi: optic chaism, tec: optic tectum, di: diencephalon, tel: telencephalon.

A new-born RGC axon first navigates through the retina towards the optic nerve head. Within the retina, RGC axons are constrained to a specific retinal layer called the optic fibre layer. This confinement is critically reliant on the expression of adhesion molecules, in particular NrCAM, in the underlying neuroepithelial endfeet. The homophilic cell adhesion molecule L1CAM is also important, allowing RGCs to adhere to other RGCs that navigated ahead of them[34,109].

Upon arriving at the optic nerve head, RGCs must change direction and exit the eye. Early work suggested a role for topographic guidance in this process, as oriented neuroepithelial endfeet seemed to form 'channels' around the optic fissure that might guide RGCs[34]. Netrin1 signalling is also essential: the disk of neuroepithelial cells surrounding RGCs as they head for the optic nerve head secretes netrin-1, which is sensed by DCC receptors on RGCs. In this case DCC is thought to transduce an attractive signal, which is essential for proper exit of RGCs from the eye[110].

Once in the brain, RGCs encounter the optic chiasm. Here all axons project to the contralateral brain hemisphere in *Xenopus* embryos. The positioning of the optic chiasm is thought to be defined by a temporally controlled alleviation of inhibitory sonic hedgehog (Shh) signalling[39], as well as by inhibitory Slit/Robo2 signalling[111]. Slit/Robo also seems to play a role in error correction, redirecting aberrantly projecting RGC axons in zebrafish (in which all RGCs also project contralaterally)[112]. Studies in zebrafish have also identified the secreted semaphorin Sema3D present at the chiasm, and Sema3D knockdown resulted in an increased number of aberrantly projecting ipsilateral axons[113]. Thus multiple guidance mechanisms seem to be in place; however, how they function

together to ensure proper contralateral projection of embryonic axons is not fully understood.

Subsequently, axons in the optic tract are thought to be constrained to their path via Slit/Robo signalling, perhaps aided by repulsive chondroitin sulfate proteoglycans in the telencephalon[112,114]. Midway through the brain, the optic tract bends to head toward the tectum. This bend is associated with a proposed gradient of secreted Slits and Sema3A[115,116]. Here Sema3A is thought to act as a repulsive cue, but it has at least one other function: Sema3A induces local translation of the homophilic cell adhesion molecule NF-protocadherin (NFPC) and its cytosolic partner molecule TAF-1[100]. Thus Sema3A may serve also to promote adhesion and therefore stimulate growth; consistent with this, the phenotype of a Sema3A/Slit1 knockdown is axon stalling, rather than misdirection[100].

RGCs terminate in the optic tectum. Here they undergo a complex process of topographic mapping wherein the initial position of the RGC cell body in the retina determines the physical location of its synaptic targets in the optic tectum. The formation of these maps relies critically on Eph/Ephrin signalling[117].

1.3 Mechanical constraints on biological systems

In addition to chemical signals, the biophysical properties of the environment strongly affect cell morphology and gene expression patterns[118], influencing cell behaviour across the entire lifespan of an organism, from stem cell differentiation[119] to cancer progression and invasion[120,121]. Most relevant to this thesis, mechanics plays an important role in nervous system development[122] and axon guidance[123].

In the following sections I will briefly introduce key techniques that have been developed to measure cell and tissue mechanical properties *in vivo* and to explore mechanical responses of cultured cells *in vitro.* I will then review the mechanisms by which cells are thought to sense their physical surroundings. Finally I will discuss membrane tension and the use of optical tweezers to measure it.

1.3.1 Cell and tissue mechanics *in vivo* and *in vitro*

Methods for measuring cell and tissue mechanics often focus on elastic tissue properties; an **elastic** material is one which deforms in response to an applied force, but then returns to its original confirmation once the force is removed. The force exerted on a material per unit area is referred to as **stress** (unit: $Pa = N/m^2 = pN/\mu m^2$), and the relative deformation

of the material in response to as stress is **strain** (dimensionless). Stress and strain in a **linearly elastic** material are proportional, in a **nonlinearly elastic** material, the stress/strain relationship changes with changing stress. Nonlinear elasticity is often encountered in biological materials, as, for example, tissues[124] and cytoskeletal networks[125] undergo strain stiffening. The relationship of stress to strain at any given moment can be quantified as an **elastic modulus**. Various different elastic moduli can be reported depending on how the stress was applied; in this thesis, the stiffness of hydrogels is generally reported as **shear modulus** (G, Pa), which relates stress applied parallel to a material's surface (shear stress) to the corresponding strain. Finally, the resistance of a fluid to flow, its **viscosity**, is quantified by the ratio of stress to strain rate. Biological tissues usually exhibit some degree of **viscoelasticity**, that is, the elastic deformation of tissues in response to strain is accompanied by some degree of viscous flow.

A variety of methods have been developed to study the physical properties of tissues. A review of these techniques with a focus on the mechanical properties of brain tissue can be found Reference [126]. The application of these techniques to different tissues in the body has revealed that biological tissues span several orders of magnitude in stiffness, from a few hundred pascals in brain[127] and bone marrow[128] to megapascals in cartilage[129].

Bulk elastic moduli offer an important readout of tissue status, but are less useful at describing the biophysical milieu encountered by cells within a tissue. Atomic force microscopy (AFM) has emerged as a powerful method for probing the stiffness of biological tissues with a spatial resolution relevant to growing cells, helping to bridge the gap between large scale tissue measurements and the exploration of individual cell mechanics and behaviour. In AFM stiffness measurements, a probe attached to a thin cantilever is used to push on a tissue and the resultant deflection of the cantilever measured using a laser[130,131]. For biological applications, the probe is generally a spherical one. As will be discussed in more depth later (Section 1.4.2) AFM has been used to map the physical properties of the surface of the *Xenopus* brain[123,132].

In vitro methods (reviewed in the context of the nervous system in Reference [122]) generally aim to expose individual cells to a controlled mechanical environment, or to a specific deformation, and to readout their responses, generally optically. I will briefly discuss several of these techniques with a focus on how they have been used to elucidate the mechanical responses of neurons.

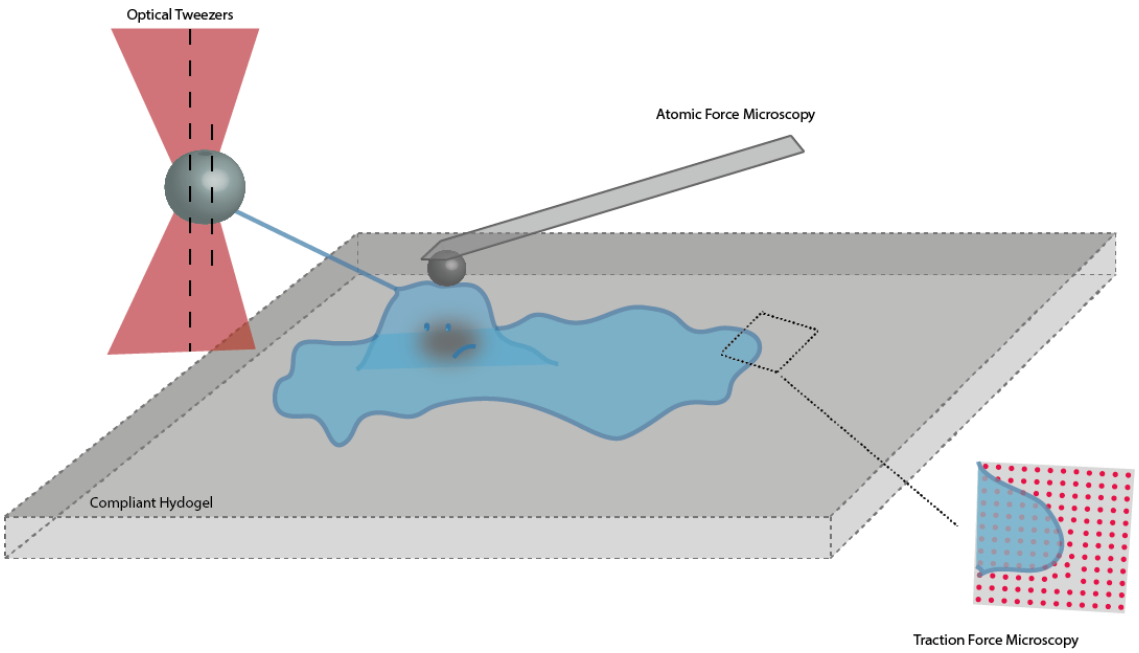

Figure 1.7: Perturbing and measuring cell mechanics *in vitro*

Numerous methods have been developed to perturb and measure cell mechanics in vitro. The physical environment can be set by growing cells on compliant hydrogels. Forces can be exerted and/or measured by deformation with an AFM cantilever, membrane tethers can be pulled via beads held in an optical trap, and traction forces exerted on the substrate can be measured by TFM.

The stiffness of the underlying substrate encountered by cells in culture can be controlled using compliant hydrogel substrates. These gels are generally composed of a polymer, wherein the degree of crosslinking can be tuned to determine the elastic properties of the gel. Hydrogels have been developed from a variety of polymers, including protein or polysaccharide based biological polymers such as matrigel[133] and agarose[134], or synthetic polymers like polyacrylamide (PAA)[135]. PAA gels can offer a slightly more controlled environment than those composed of biopolymers, as they are biologically inert until functionalized[136]. PAA gels can then be functionalised with an adhesive ligand of choice, such as laminin, fibronectin, or collagen.

Traction force microscopy (TFM[137,138]) makes use of soft gels with embedded fluorescent beads to serve as fiduciary markers. Careful analysis of bead deformations allows measurement of the forces exerted by cells on the substrate. A related technique involves growing cells on elastic micro pillars and imaging the deformation of these pillars[139]. TFM measurements of neurons in culture has been employed to map the forces neuronal growth cones exert on their environment[28], and to demonstrate that even individual exploratory filopodia deform their substrate in a stiffness-dependent manner[29].

Mechanical perturbations can be applied to a cell in culture via a variety of methods. In some early studies exploring the influence of physical forces on neuronal growth, Dennis Bray used glass needles to exert tension on the processes of developing neurons, demonstrating that axons grow or even form in response to increased mechanical tension[140]. Neurons have since been exposed to host of other mechanical stimuli, including membrane stretch with osmotic shock[141], and indentation with an AFM cantilever[142]. Neurons respond to these diverse stimuli with an immense variety of active responses, indicating that they contain sensitive and fast machinery for sensing and responding to a wide variety of mechanical perturbations.

1.3.2 How do cells sense mechanics?

Motile cells constantly interact with the extracellular matrix (ECM) via integrin-containing adhesive contacts— focal adhesions in most cells, and point contacts in neurons. Actomyosin forces generated within the cell are converted into forward motion by the resistance provided at these adhesion sites. Many of the proteins which link adhesion complexes to the actin cytoskeleton are themselves mechanosensitive, such as such as talin[143], thus the maturation and stabilization of adhesions is a mechanosensitive process dependent on these actin generated forces[144]. The amount of resistance encountered in the ECM can feed back onto focal adhesions, helping to control their assembly, maturation, and turnover (reviewed in Reference [145]). Focal adhesion dynamics affect cytoskeletal structure and cellular morphology. These structural changes (along with other signalling cascades directly activated at focal adhesions) ultimately feed back onto the gene expression programs that control cell fate and behaviour[145,146].

In one of the first demonstrations of focal adhesion mechanosensitivity, Pelham and Wang found that focal adhesions of fibroblasts cultured on soft substrates turn over more quickly and do not mature into the stable, elongated forms seen on stiff substrates[147]. These structural changes can be related directly to the classical morphological influence of substrate-stiffness: stiff substrates induce highly spread cells with strong stress fibres coupled to robust and mature focal adhesions; weaker and more transient adhesions on soft substrates lead to cell rounding. However, different cells seem to be tuned to distinct stiffness regimes, and, for different cell types, these changes in morphology occur at different 'critical stiffnesses'[148].

In growth cones, which lack stress fibres or the massively accreted focal complexes seen in fibroblast like cells, a 'motor-clutch' model has been proposed. This model connects

actin polymerization, retrograde flow rates, and the loading point contacts, to suggest a mechanistic explanation of the different growth behaviours seen on soft and stiff substrates[29]. Experiments with embryonic chick CNS neurons seemed to validate aspects of this model. These experiments suggested that a critical threshold in substrate stiffness, which segregated growth cone behaviour into two regimes, occurred for these cells at around 1 kPa[29].

Additionally, mechanosensitive proteins localized to focal adhesions can directly initiate intracellular signalling cascades. For example, phosphorylation of the key signalling protein focal adhesion kinase (FAK) increases on stiff substrates[149,150].

Non-migratory cells, such as those in large epithelial tissue sheets connected by adherens junctions, are also mechanosensitive, and large scale forces and tensions transmitted through tissues are critical in development[151,152], for example tension can orient cell divisions in epithelial sheets[153].

1.3.2.1 Mechanosensitive Ion Channels

In addition to mechanosensing at adhesion complexes, many cell types contain additional dedicated mechanosensory elements. Mechanosensitive ion channels (MSCs) are defined as ion channels that can be modulated over their entire dynamic range by mechanical force alone. Mechanosensitive ion channels allow cells to respond rapidly (on timescales of milliseconds) to specific external mechanical cues, including shear forces, osmotic pressure, and touch sensation. They are present both in nonspecialized cells and in dedicated mechanosensory cells, and likely represent an ancient and critically important mode of response to rapidly changing environmental conditions[154,155].

Of particular relevance to this thesis is the recently discovered mechanosensitive ion channel Piezo1[156,157]. Piezo1 functions as 900 kD homotrimeric channel with a unique architecture that resembles a propeller with three curved blades surrounding a central pore[158,159]. It is sensitive to a wide variety of mechanical perturbations, including osmotic shock[160,161], shear stress[162], positive or negative pressure applied in a patch pipette, indentation[163,164] or pulling forces[165], or cell stretching[166].

Piezo1 is widely expressed in mammalian tissues[167], and Piezo1 knockout mice are embryonic lethal due to catastrophic failures in vascular development[168]. Already in the short time since its discovery Piezo1 has been associated with a number of human diseases. Specifically, gain-of-function mutations that disrupt red blood cell volume

homeostasis lead to dehydrated hereditary stomatocytosis[169], and Piezo1 mutations also result in lymphatic dysplasia[170].

A significant effort has been made to determine the mechanism by which Piezo1 channels are gated. Syeda and colleagues reconstituted Piezo1 in lipid droplets to show that lipid bilayer tension alone was able to activate Piezo1[160]. Thus Piezo1 can be gated purely via forces transmitted through the bilayer, but it is unclear if this is actually how it is gated *in vivo*. Several studies have indicated that cytoskeletal elements impact Piezo1 gating[163,164]. Cox et al. postulated a mechanoprotective role for the cytoskeleton, and demonstrated that Piezo1 is activated at lower pressures in cytoskeletal free blebs then in cytoskeleton-linked HEK293 cell membranes[164]. Conversely, Gottleib et al, found that application of the actin polymerization inhibitor cytochalasin D strongly reduced current amplitudes[163].

The confounding factor in these seemingly contradictory results could relate to methodology[171]. In the experiments described above, Cox et al., used cell attached patches to both apply pressure and record currents. Gottleib et al., recorded whole cell currents from cells mechanically stressed by indentation; and in fact a strong influence of cytochalasin D was not observed when Piezo1 was activated in cell-attached patches. There are many differences between the patch environment and a whole cell recording, including; for example in whole cell recordings where the cell is stressed by indentation, the activating force has to propagate from the indentation site, and that processes may depend on the cytoskeleton.

Piezo1 gating is also sensitive to changes in membrane lipid composition, for example, a disruption of membrane cholesterol domains impairs mechanotransduction and Piezo1 signalling[172,173]. To complicate matters further, structural studies have found that the large Piezo1 channel deforms the membrane significantly, suggesting that membrane curvature may contribute significantly to its activation energy [174].

Most studies have examined Piezo1 gating in response to specific external mechanical stimuli. Recently, Ellefsen and colleagues examined the endogenous activity of Piezo1—that is, Piezo1 activity in response to internally generated forces. They found Piezo1 signals mainly localized around focal adhesions, though how the force generated at focal adhesions is transmitted to the Piezo1 protein remains unclear[175].

Finally, studies of Piezo1's mechanism and activity have been facilitated by the recent discovery of pharmacological agents capable of activating Piezo1 currents without the need for mechanical stimuli. The first of these was the small molecule agonist Yoda1,

discovered in a marathon chemical screen[176]. Yoda1 seems to physically bind to the Piezo1 channel[161], and consistent with this a Yoda1 analogue (Dooku1), seems to competitively inhibit Yoda1-induced activation, suggesting a specific binding site[177]. More recently, another family of small molecule agonists, termed Jedi1 and Jedi2 have been reported, which seem to have a distinct binding site and Piezo1 activation mechanism to Yoda1[178]. These compounds not only offer powerful tools for studying Piezo1, but are also potentially therapeutically interesting given Piezo1's many roles in human diseases.

1.3.3 Membrane tension

The transmission of mechanical stimuli directly via changes in membrane tension is one mechanism proposed for the gating of many MSCs, including Piezo1 channels.

All biological cells are contained within a semipermeable lipid bilayer, which is under lateral tension. In a system comprised only of lipids, such as might be encountered in a simple vesicle, this tension arises from a force balance: there is an attractive force between hydrophobic tails largely due to entropic exclusion of water molecules, and a repulsive force between the negatively-charged hydrophilic head groups. In this case, membrane tension is a simple global parameter, equilibrating quickly over the surface of the vesicle, like the increasing tension in a balloon as more air is added[179].

In a cell, however, the situation is much more complex. The membrane is crisscrossed by proteins, and tethered to the underlying cytoskeleton. This intrinsic coupling of lateral bilayer tension (T_m) to a membrane-cytoskeletal friction (γ) means that is not always clear what is meant when membrane tension is referenced in a biological context. Usually, in biological cells, 'tension' refers to the 'apparent membrane tension', which is the sum of the tension in the lipid bilayer, and the membrane-cytoskeletal adhesion term ($T = T_m + \gamma$) [180].

Several methods have been developed to perturb and measure membrane tension in living cells. These are reviewed extensively elsewhere[181]. For adherent cells, pulling thin tethers of membrane using a bead caught in an optical trap (Figure 1.7) or stuck on an AFM cantilever, are among the most common methods. The membrane tension exerts a force on the bead, pulling it away from the centre of the optical trap, or deforming the AFM cantilever.

Optical tweezers provide the most quantitative readout of membrane tension, and the theoretical underpinnings of extracting tension values from these experiments have been extensively developed[182,183]. The force, F, exerted by the membrane tether on the bead held in the optical trap can be obtained by measuring the deflection of the bead from the centre of a trap (Δx) with previously measured spring constant k. Generally it is assumed that the tether is free of cytoskeletal elements, though this assumption may not always be valid[182]. Minimization of the Helfrich bending energy of the membrane results in

$$F = 2\pi\sqrt{2TB} \quad (1)$$

Where $T = T_m + \gamma$, the effective membrane tension which sums the contribution of bilayer tension and membrane-cytoskeletal coupling. Decoupling these terms requires measurement of the membrane radius, R, in which case:

$$T = \frac{F}{2\pi R}, B = \frac{FR}{2\pi} \quad (2)$$

T_m and γ can then be separated by measuring membrane tethers in cytoskeletal free blebs[184] (which should represent T_m only).

A critical limitation of the optical tweezers method is it lacks detailed spatial or temporal resolution. An optical probe has recently been developed with the aim of providing higher resolution measurements[185].

While membrane tension is recognized as a critical parameter involved in modulating cell shape, motility, and behaviour (reviewed in Reference [181]), much remains unknown about the nature and regulation of membrane tension in living cells. For example, is not well understood how membrane tension relates to other mechanical parameters such as substrate stiffness. It has been generally been assumed that changes in membrane tension equilibrate swiftly and globally across the surface of biological cells, thereby providing a mechanism for swift propagation of mechanical signals[180]. However, recent studies have called this into doubt, indicating that the barriers provided by transmembrane proteins inhibit the fast dissipation of tension, thus suggesting that increases in tension might serve as local, rather than global, signals[186].

1.4 The importance of mechanical signals in RGC axon growth and guidance

This thesis builds on work completed in the Franze lab that has demonstrated a critical role for mechanosensing, and for the MSC Piezo1 in particular, in axon guidance in the

Xenopus optic pathway. In this section I will discuss our studies of the *in vitro* mechanosensitivity of *Xenopus* RGC axon, and what has been found about the mechanical environment encountered by these axons during their development. Some of the *in vitro* data shown here were collected during my MPhil degree, and some during the beginning of my PhD; I have made every effort to make clear which results are mine and when the experiments were conducted. A statement of contributions can be found at the end of the Section 1.4.1.

1.4.1 RGC mechanosensitivity *in vitro*

I studied RGC mechanosensitivity *in vitro* by explanting *Xenopus* eye primordia onto 100 Pa (soft) and 1 kPa (stiff) hydrogel substrates. I observed a robust and complex response to substrate stiffness[123]. The extent of outgrowth on laminin was strongly affected, with axons on soft substrates exhibiting less overall outgrowth (Figure 1.8 Ai, Aiii). We observed the same effect on fibronectin, which engages a different population of integrins than laminin (Figure 1.8Ai, Aiii). Tracking axonal growth trajectories revealed that, while axons on soft substrates actually moved more quickly, they grew in a much less directed manner (Figure 1.8B) and therefore covered less ground than those grown on stiff substrates.

Substrate properties also influenced fasciculation of RGC axon bundles—that is, the tendency of axons to preferentially grow in tight bundles adhered to other axons. On soft substrates, axons had a reduced tendency to fasciculate. Fasiculation is likely an important parameter in axon guidance, and may also be important in regulating axonal responses to chemical guidance cues. This is because adherence to homophilic cell-cell adhesion molecules like L1CAM, in place of ECM molecules like laminin, is a critical signal; for example, addition of L1 can convert Sema3A responses from repulsive to attractive[77].

Together, these results suggested that on stiff substrates, axons grow in a more directed manner, cover ground more efficiently, and seem to have a higher tendency to follow the trajectories of preceding axons. In contrast, on soft substrates, axons exhibited what could be termed ‘wandering’ or ‘exploratory’ behaviour, showing an increased tendency to change direction, and a reduced tendency to follow the trajectories of preceding axons.

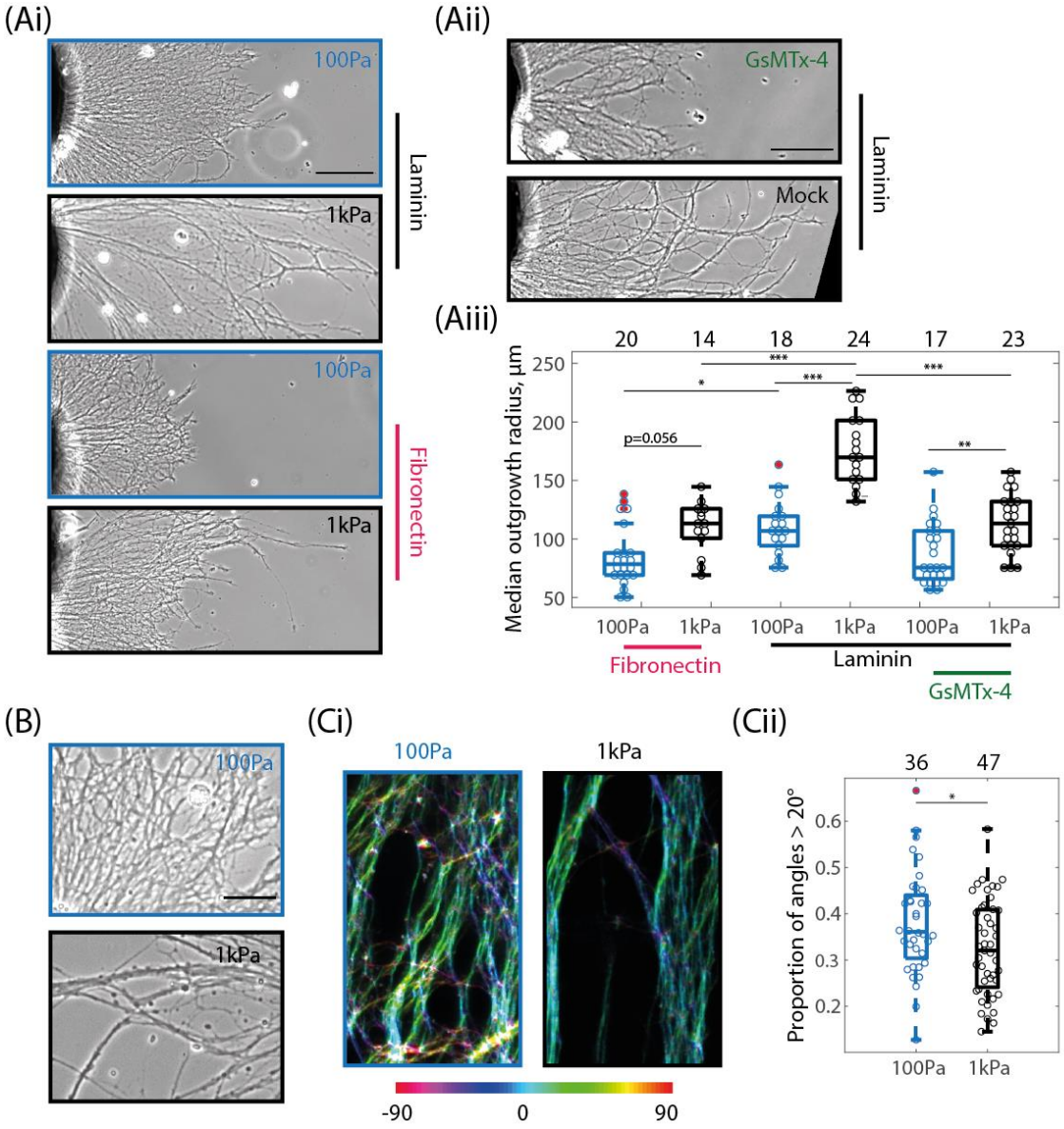

Figure 1.8: RGCs sense and respond to their mechanical environment

Figure 1.8: (continued)

*Substrate stiffness influences RGC axon growth and fasciculation. (Ai) RGC axon growth on different substrate: the black hemisphere to the left in these images is the side of the explanted eye primordium; a dense meshwork of axons emerges from the explant and grows across the gel. Axons from explants grown on stiff (1 kPa, black outlines) substrates are significantly longer after 24 hours than those from explants grown on soft (100 Pa, blue outlines). The same behaviour is observed on substrates coated with both laminin and fibronectin. Scale is 100 µm. (Aii) The MSC inhibitor GsMTx-4 inhibits axon outgrowth (experiments conducted on a laminin substrate). The images shown are both on 1 kPa substrates and the scale bar is 100 µm. (Aiii) Quantification of axon outgrowth on soft and stiff substrates in different conditions. Fibronectin data are from three biological replicates, laminin data from four replicates, treated in the GsMTx-4 condition with a concentration of GsMTx-4 between 0.5 and 5 µM, as the potency of the drug depended critically on batch number and how long it had been stored. Number of explants analysed in each condition are stated above each boxplot. Data were assessed with an ANOVA ($p = 1.2e^{-19}$) followed by a Bonferroni post hoc test For the values shown on the plot: On fibronectin: $p_{soft \rightarrow stiff} = 0.056$; on laminin: $p_{soft\ ctrl \rightarrow stiff\ ctrl} = 2.1e^{-08}$, $p_{soft\ ctrl \rightarrow soft\ GsMTx\text{-}4} = 0.067$, $p_{soft\ GsMTx\text{-}4 \rightarrow stiff\ GsMTx\text{-}4} = 0.0089$, $p_{stiff\ ctrl \rightarrow stiff\ gsMTx\text{-}4} = 2.1e^{-08}$, and comparing between adhesion conditions, $p_{stiff\_fn \rightarrow stiff\_ln} = 2.2e^{-08}$, $p_{soft\_fn \rightarrow soft\_ln} = 0.03$). A complete table of the statistics for this figure can be found in Appendix 1.1 (Table 6). (B) Representative images from explants grown on 100 Pa (blue outline) and 1 kPa (black outline) substrates demonstrating characteristic morphologies. On soft substrates, axons appear less tightly bundled. (C) Directionality of axon growth was quantified by examining local angular orientation of axon segments using the ImageJ plugin OrientationJ. (Ci) Sample regions from explant cultures stained for tubulin to visualize axons. The axons have been pseudo-coloured to show their angular orientation. The colormap indicates angle, where 0° would indicate an axon growing vertically. (Cii) Angular distributions were wider for regions analysed on soft substrates. Each point represents the proportion of angle values greater than |20°| for an individual region of axons. Images were taken from three biological replicates. The number of images used is shown above each boxplot. P = 0.025, two sample t-test. With the exception of the images in (B), the data in this figure were published in [123], and methodological details related to experiments and analysis procedures can be found therein. *p< 0.05, **p<0.01, ***p<0.001.*

Finally, we examined the behaviour of RGCs on substrates that were fabricated with a gradient in stiffness. Axon bundles showed a preference for the softer side of gradient substrates *in vitro*, indicating that, in principle, gradients of tissue stiffness could provide a directional guidance cue to growing axons (Figure 1.9).

Statement of contributions: Analysis of axon outgrowth on laminin with and without GsMTx-4 treatment was first conducted during my MPhil (Figure 1.8Aii). Analysis of axon outgrowth on fibronectin was conducted during my PhD. For clarity of comparison, all images in (Figure 1.8 Ai) come from the same experiment (which was conducted during my PhD). Images in (Figure 1.8 B) were randomly selected from an experiment conducted during my PhD that required explant growth on soft and stiff substrates. Orientation analysis in (Figure 1.8 C) was conducted during my PhD; images of tubulin stained axons were acquired by Eva Pillai, and I completed the downstream orientation analysis. Data in Figure 1.9 was obtained during my MPhil. These data were published in [123], with the exception of the images in (Figure 1.8 B), which were taken for an unrelated experiment.

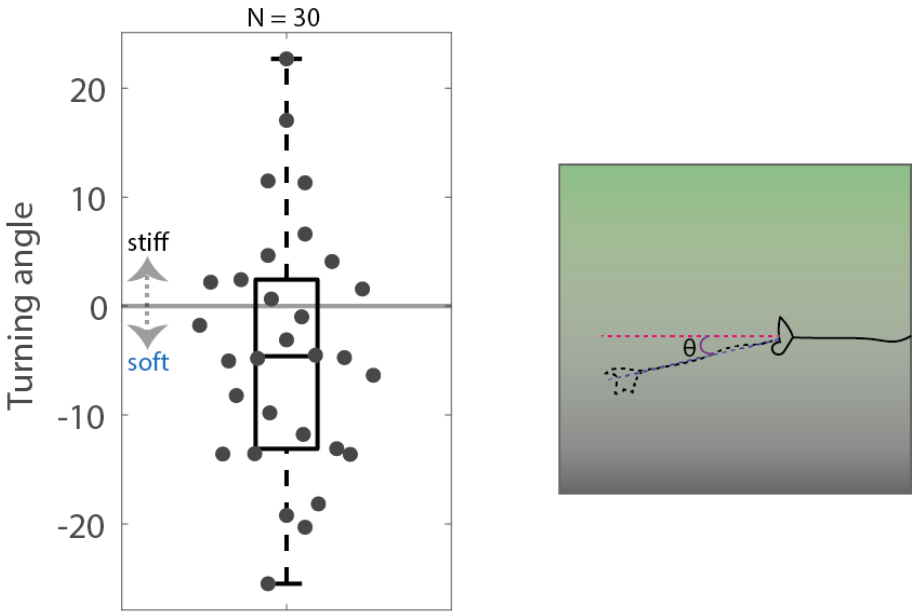

Figure 1.9: RGC growth on gradient substrates

Analysis of RGCs grown on substrates with a gradient in stiffness found that there was a trend towards turning to the softer side of the substrate (here negative angles). Turning angles describe the angular deflection of the axon's final growth trajectory from a hypothetical straight growth trajectory. The cartoon to the right explains the experimental setup and analysis: axons grow on a gel with a gradient in stiffness. Growth is recorded for one hour, after which the final trajectory of the axon (blue dashed line) is compared with the trajectory that would have been taken if the axon had continued straight (red dashed line), yielding a turning angle θ. Data were collected from 30 axons imaged over seven separate experimental days. P = 0.07, one-sample t-test. This data was published in [123].

1.4.2 The mechanical environment of the *Xenopus* optic tract

The ability of gradients in substrate stiffness to actually provide directional guidance to RGCs requires that these gradients are present *in vivo*. My colleagues have measured the physical properties of the *Xenopus* brain, and have shown that it presents a complex, heterogeneous mechanical environment. Moreover, they have demonstrated the developmentally regulated emergence of gradients in tissue stiffness that are well positioned to guide growing RGCs[123,132].

The *Xenopus* brain surface can be exposed by removing the eye, skin, and dura from one side of the embryo. This enables *in vivo* measurement of the brain using AFM. AFM measurements conduced in developing *Xenopus* embryos revealed a gradient in substrate stiffness in the *Xenopus* brain. Time lapse AFM showed that the formation of this gradient preceded the turning of RGC axons at the mid-optic tract bend in their trajectory (Figure 1.6, Figure 1.10). The gradient was correlated with a corresponding gradient in cell

density. Disrupting this gradient, by either mechanically stiffening regions of the brain[123], or disrupting mitosis and therefore the asymmetric cell division that establishes the causative cell density gradient[132], resulted in aberrant axon pathfinding.

(A)

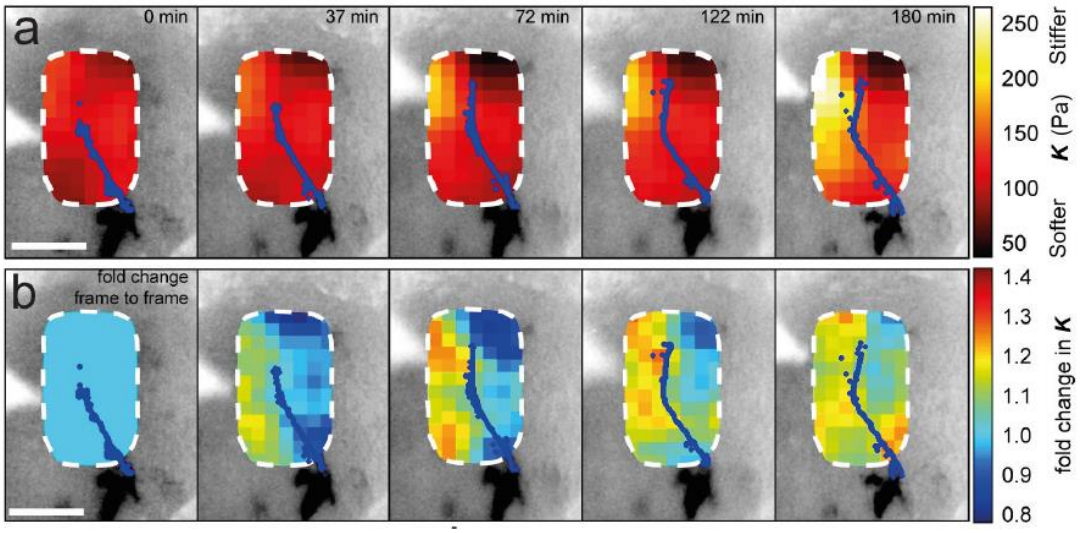

Figure 1.10: The *in vivo* mechanical environment of RGC axons

Xenopus RGCs navigate a heterogeneous and changing mechanical environment. (A) Stills from a timelapse in vivo AFM experiment, reproduced from [132]. In this experiment the stiffness of the brain of a live, developing embryo was mapped with AFM repeatedly over several hours in order to understand changes in brain mechanical properties during development. The heat maps in (a) show raw stiffness values, with darker colours indicating softer tissue, and lighter colours indicating stiffer tissue. Heat maps in (b) show the same data presented as the fold changes in stiffness from the first time point, with warmer colours indicating a higher fold change. The timepoints cover the time period relevant to RGC growth through the mid-optic tract bend, and RGC axons are pseudo-coloured in dark blue. The environment through which RGC axons grow stiffens over time, and a stiffness gradient emerges. Scale bars are 100 µm. Here K represents reduced apparent elastic modulus; please see the text for the relation of K to G (Section 7.2.1).

1.5 Outlook

Mechanically signalling, in particular axon guidance via an instructive gradient in tissue stiffness, seems to be an important regulator of axon growth in the developing *Xenopus* optic pathway.

Chemical guidance cues are highly sensitive to environmental perturbations. Chemical and mechanical guidance signals necessarily converge on many common signalling cascades, particularly those involved in the regulation of the cytoskeleton. Given these factors, and the mechanosensitivity of RGC axons, I hypothesized that the physical environment of RGCs should not only directly impact their growth trajectories but also

influence growth cone responses to chemical guidance cues. In this thesis I have therefore addressed the following questions

1) Do changes in the stiffness of a neuron's substrate influence its response to the chemical guidance cue Sema3A?
2) If so, what biochemical changes does the mechanical environment induce in the growth cone that lead to an altered response to Sema3A?
3) Mechanosensitive ion channels, and in particular Piezo1, are important for *Xenopus* RGC mechanosensivity; do they play a role in any substrate-stiffness dependent modulation of the Sema3A response?

2 METHODS

Unless otherwise specified, all solutions are from Sigma.

2.1 Xenopus husbandry, dissection, and cell culture

All animal experiments described in this thesis were conducted in compliance with the Ethical Review Committee of the University of Cambridge and Home Office Guidelines. Mixed sex *Xenopus* eggs were obtained and fertilized *in vitro*. Briefly, newly laid eggs were washed in 1x Modified Barth's Saline (MBS)*, and distributed among several petri dishes. Fresh testes stored in testes solution (1x MBS + 20% foetal calf serum and 0.05 mg/mL gentamycin) were macerated. A few drops of testes were added to each dish of eggs. After stirring and a 3 minute incubation, distilled water was added to activate the sperm. After ~30 minutes, the fertilized eggs were transferred to 0.1x MBS. Embryos were subsequently kept in 0.1x MBS at 12-16°C and washed daily until they were used.

Unless otherwise specified, experiments used explants from embryos at stage 35/36 (All stages are reported according to the Nieuwkoop and Faber[103]). Prior to dissection, embryos were anesthetized in 20% w/v tricaine methanesulfonate solution (MS222, pH 7.6-7.8, with 1x Penicillin-Streptomycin-Amphotericin B (PSF, Lonza*)), and were immobilized onto Sylgard lined petri dishes using a bent 0.2 mm insect pin (Austerlitz). Using a 0.1 or 0.15 mm insect pin (Austerlitz) in a pin holder, intact eye primordia were removed and placed immediately into 60% L-15 (pH 7.6-7.8, with 1x PSF, referred to as '*Xenopus* culture media').

Eye primordia were placed, with the lens facing upwards, onto glass or hydrogel substrates. Glass substrates had been incubated at room temperature with 10 µg/mL Poly-D-Lysine (PDL, MW 70-150 kDa) diluted in Phosphate Buffered Saline (PBS) for 30 minutes, washed, and then incubated in 5 µg/mL Laminin in PBS for 30 minutes. For gels, incubation times were overnight (PDL) and two hours (Laminin), with the same concentrations. Immediately (glass) or 2 hours (gels), after plating, explants were moved to a 20°C incubator. Unless otherwise stated, explants were cultured in *Xenopus* culture media (see above), and experiments were conducted after ~20-24 hours in culture.

*A 10x stock solution of MBS comprised: 88 mM NaCl, 1 mM KCl, 2.4 mM NaHCO3, 1 mM HEPES, 0.82 mM $MgSO_4$, 0.33 mM $Ca(NO_3)_2$, 0.41 mM $CaCl_2$, pH 7.6

*1x PSF: 1% v/v of a 100x solution containing: penicillin (10,000 U/mL), streptomycin (10,000 µg/mL), amphotericin B (25 µg/mL)

2.2 Fabrication of compliant culture substrates

Polyacrylamide hydrogels of single or gradient stiffness were prepared as previously described[123,147]. Gels were polymerized between a 'bottom' and a 'top' coverslip, with the top coverslip determining the size of the gel. For most experiments, 19 mm diameter bottom and 18 mm diameter VWR no. 1.5 glass coverslips were used. For optical tweezers experiments, gels were made in 35 mm diameter no. 0 glass-bottomed dishes (MatTek) with an 18 mm top coverslip. For Biopen experiments wide (50 mm) diameter glass-bottomed dishes were used (MaTek) with an 18 mm top coverslip.

Both coverslips were first washed in 70% ethanol and water and then dried. Bottom coverslips were wiped with a cotton bud dipped in 1M NaOH, allowed to dry, and then incubated in (3-aminopropyl)trimethoxysilane for three minutes. After thorough washing in double distilled water (ddH_2O), they were incubated in 5% glutaraldehyde solution for 30 minutes, and then washed thoroughly. Top coverslips were treated with Rain-X (Shell) for ≥10 minutes.

Gel Premixes were made fresh for each batch of gels using 40% acrylamide and 2% bis-acrylamide (Thermo Fisher) diluted in PBS according to the proportions in Table 1, and subsequently degassed in a vacuum chamber for 3-7 minutes. Proportions for gel premixes had previously been determined using AFM to confirm gel stiffnesses.

Table 1: Acrylamide proportions for gels

Shear Storage Modulus (G', in Pa)	% Acrylamide	% Bis-Acrylamide
100*	5	0.04
1100*	7.5	0.06
3350	7.5	0.2
9700	12	0.2

*For two-stiffness gels (see below), 5 µL of PBS were substituted with 5 µL of 1% w/v fluorescein 0,0'-dimethacrylate in either 100 or the 1 kPa premix.

To initiate crosslinking, 5 µL of freshly prepared 1% ammonium persulfate (APS) followed by 1.5 µL of 0.3% N,N,N',N'-tetramethylethylenediamine (TEMED, Thermo Fisher) were added to each 500 µL premix. Premixes were mixed thoroughly by gentle pipetting.

For single stiffness gels, a droplet of premix was placed onto the bottom coverslip, and the top coverslip placed on top. The volume of the droplet determines the thickness of the gel. Gels used for most experiments were over 80 µm thick; with the exception of gels used for the optical tweezers experiments, which were 20 µm thick.

For some experiment I fabricated gels containing both soft and stiff regions in the same dish. These were not used to expose cells to a stiffness gradient and thus I call them 'two-stiffness gels' rather than gradient gels. These were fabricated by depositing a 12 µL droplet of 100 Pa premix and one of 1 kPa premix next to each other and then placing the top coverslip over both to create one gel with two distinct stiffness regions, separated by a relatively small gradient region. As the fluorescein label was only incorporated into one premix, fluorescein fluorescence could be used to distinguish the different stiffnesses. To control for the potential influence of gel-incorporated fluorescein on imaging experiments, I switched which premix contained the fluorescein between replicates.

After the residual premix had solidified, gels were rinsed in PBS, and then treated with hydrazine hydrate for 3-4 hours, followed by one hour in 5% acetic acid (Acros Organics). Prior to coating with adhesion molecules as described above, gels were sterilized under UV illumination for 30 minutes. Gel elastic moduli were periodically confirmed using AFM with the assistance of Joy Thompson.

2.3 Molecular Biology

2.3.1 Constructs

DNA constructs used for experiments in this thesis are listed in the following table.

Table 2: DNA constructs

Construct	Source	Notes and Modifications

pGP-CMV-NES-jRCaMP1b	Addgene plasmid #63136; This construct was deposited by the Douglas Kim lab	For use in *Xenopus*, the jRCaMP1b insert was subcloned into a PCS2+ vector.
PCS2+	PCS2+ vector construct was a gift from the lab of Christine Holt	
mCherry-PCS2+	mCherry-PCS2+ plasmid was a gift from the lab of Christine Holt	

The jRCaMP1b insert was subcloned into the PCS2+ vector to allow *in vitro* transcription from the SP6 transcription start site. Subcloning was completed using standard restriction enzyme based methods. Briefly, the jRCaMP1b insert was extracted from the pGP-CMV-NES vector via restriction digestion with Afe1 and Not1-HF, and the PCS2+ vector was prepared via digestion with Stu1 and Not1-HF (all restriction enzymes from New England Biolabs). Both fragments were run on 1.5% agarose gels, and retrieved using a gel extraction kit (Qiagen or New England Biolabs). The insert was ligated into the vector using a T4 DNA ligase based ligation kit (TAKARA). The ligation product was transformed into Library Efficiency® DH5α™ cells (Thermo Fisher) via 45 seconds of heat shock at 45°C, and transformed cells were spread onto media plates (Luria Broth (LB, Invitrogen) + Bacto-Agar (BD)) containing 100 µg/mL of ampicillin and allowed to grow overnight at 37°C. Individual colonies were selected, and amplified via shaking incubation overnight at 37°C in 5 mL of LB + 100 µg/mL ampicillin in a round bottom conical tube. Plasmid DNA was subsequently extracted using a Miniprep kit (Qiagen or New England Biolabs). DNA was digested with BstX1 + Nde1 and separately with Not1-HF + HindIII-HF, and subsequently run on a 1.5% agarose gel (all restriction enzymes from New England Biolabs). Clones which displayed the correct band sizes upon restriction digestion were sent for Sanger sequencing. Constructs were sequenced using the SP6 and M13 standard primer sites present in the PCS2+ vector. Sequencing was completed by the Sanger Sequencing Facility at the Department of Biochemistry (University of Cambridge).

2.3.2 RNA synthesis

RNA was synthesized via *in vitro* transcription beginning from the SP6 transcription start site present in the PCS2+ vector. Briefly, constructs were first linearized via restriction enzyme digestion using Not1-HF. The mMESSAGE mMACHINE SP6 Transcription Kits (Invitrogen) were used according to manufacturer instructions, constructs were then polyadenylated using the Poly(A) Tailing Kit (Invitrogen). Polyadenylated RNA was purified over a column using the RNA clean-up protocol from the Qiagen RNeasy Mini Kit (Qiagen), and eluted in RNase-free water.

The final capped, polyadenylated RNA product was aliquoted and stored at -80°C.

2.3.3 Morpholinos

Translation blocking morpholinos designed against *Xenopus tropicalis* and later *Xenopus laevis piezo1* were used (MO-pz1.t, and MO-pz1.l, respectively). The nucleotides at which these two morpholinos differ in sequence are highlighted. The scrambled morpholino was a standard scrambled control. All morpholinos were obtained from Gene Tools LLC.

Table 3: Morpholino sequences

Morpholino	Sequence	Fluorescent Tag
MO-pz1.l	5’- C**G**CA**C**AGGACTTGCAGTTCCATCCC -3’	Lissamine
MO-pz1.t	5’- C**A**CA**G**AGGACTTGCAGTTCCATCCC -3’	Fluorescein
MO-scr	5’ – CCTCTTACCTCAGTTACAATTTATA – 3’	Fluorescein

2.4 Microinjection

Xenopus embryos at the four cell stage were injected in both dorsal blastomeres (BM) with an RNA, morpholino, and/or fluorescent dextran. Injected compounds and the amounts injected are listed below.

Table 4: Injected constructs

Construct/Compound	Amount injected (BM= Blastomere)	Notes

jRCaMP1b RNA	1-5 ng/BM	Different batches likely had different amounts of polyadenylation, so it was necessary to adjust the amount injected at times to maintain an adequate fluorescent signal
Mcherry RNA	~1 ng/BM	
Tetramethylrhodamine (TMR)-dextran, MW 3,000 (ThermoFisher)	5 nL of 0.2% w/v per BM	
Morhpolinos	15 ng/BM	

For injection, *Xenopus* embryos were acquired immediately after fertilisation. One cell stage embryos were stripped of their jelly coats by a gentle shaking incubation in 2% w/v L-Cysteine in 0.1x MBS, pH 8.00 for 2-3 minutes. Embryos were allowed to develop to four cell stage, at which point dorsal blastomeres can be distinguished by their lighter colour and smaller size. For injection, embryos were transferred to 4% w/v Ficoll PM400 (pH 7.5, with 1x PSF) in 0.1x MBS + 1x PSF in an injection dish with a plastic grid taped to the bottom to hold the embryos in place.

Glass capillary tubes (1.0 mm OD by 0.5 mm ID, Harvard Instruments) were pulled into needles and loaded with the relevant injection solution. Needles were held in a micromanipulator and manually broken with forceps. Droplet size was calibrated in mineral oil via a reticule in the microscope eyepiece so that a volume of ~5 nL per droplet was injected. The injection device used was a FemtoJet (Eppendorf) or a Picospritzer (WPI), connected to a compressed nitrogen gas cylinder (BOC).

Injected embryos were left to recover in Ficoll solution for 2-4 hours at room temperature, transferred to 0.1X MBS, and placed at 14-16 ºC. Prior to dissection, embryos were screened on a fluorescence stereomicroscope, and embryos with a good fluorescence signal and correct fluorescence distribution pattern (indicating that the dorsal blastomeres had in fact been successfully injected) were selected for experiments.

2.5 Electroporation

Targeted electroporation of morpholinos was conducted as has been previously described[187]. The electroporation solution contained 0.1 mM morpholino; when an additional fluorescence label was needed, the morpholino diluted in a solution of 0.2% 3 kDa fluorescein or tetramethylrhodamine (TMR) tagged dextran.

Briefly, the vitelline membrane was removed from embryos which were then anesthetized in MS222 solution as described previously, and placed belly up in a cross-shaped chamber gouged into Sylgard. The embryo was positioned in the main channel of this chamber. 0.5 mm wide platinum electrodes were positioned on either side of the embryo in the cross channel. Glass capillaries (1 mm OD x 0.5 mm ID, Harvard Instruments) were pulled into thin needles and loaded with electroporation solution. The needle was held in a micromanipulator and connected to a picospritzer (Intracel). The needle was manually broken, and subsequently inserted between the eye closest to the positive electrode and the brain of the embryo. Eight pulses of solution were dispensed from the needle, immediately followed by eight 50 ms 18 V electrical shocks spaced by 8 seconds. Electric pulses were controlled by a square wave pulse generator (Intracel).

After electroporation, embryos were returned to 0.1x MBS and placed at 14-16 ºC.

2.6 Collapse and Turning Assays

2.6.1 Collapse Assays

Collapse assays were conducted and analysed as previously described[115]. Eye primordia explants dissected from stage 35/36 embryos were cultured for ~18-20 hours. A stock solution of human Sema3A-Fc (hereafter just Sema3A, R&D Systems) was prepared by diluting the protein in PBS+ 0.1% BSA, and then filter sterilizing to minimize clumping. Immediately before the assay, Sema3A was diluted in *Xenopus* culture media to twice the desired final concentration. The final concentration of Sema3A used is stated explicitly for each experiment. It should be noted that different batches of Sema3A exhibit some variation, thus quantitative comparisons of absolute collapse rates are only drawn between data from experiments conducted with the same batch of Sema3A within a relatively restricted timeframe.

Just prior to each experiment, the Sema3A and control solutions were assigned pseudonyms. The 2x Sema3A and control solutions were then added 1:1 into the dishes in a blinded manner. Cells were incubated in Sema3A or control solution for 10 minutes,

immediately fixed in 2% paraformaldehyde (Fisher) + 7.5% sucrose for 20-30 minutes, and then washed in PBS.

To quantify collapse assays, I manually inspected cultures and counted the number of collapsed and healthy growth cones. Growth cones with two or fewer filopodia and no visible lamellipodia were considered collapsed. Only growth cones from isolated axons or axon bundles were counted. Examples of collapsed and healthy growth cones can be seen in (Figure 3.1).

Pre-treatments of axons with pharmacological compounds prior to collapse assays were conducted as follows:

Yoda1 (Abcam): 2.5 µg/mL Yoda1 added 10 minutes prior to addition of Sema3A. (For these assays the Sema3A solution also contained Yoda1, such that the concentration of Yoda1 remained constant for the duration of the assay).

1H-[1,2,4]Oxadiazolo[4,3-a]quinoxalin-1-one (ODQ, Abcam,): 200 nM or 500 nM ODQ was added 20 minutes prior to the addition of Sema3A. (For these assays the Sema3A solution also contained ODQ, such that the concentration of ODQ remained constant for the duration of the assay).

2.6.2 Biopen

Preliminary experiment with the Biopen (Fluicell) were conducted at the Fluicell headquarters in Gothenburg, Sweden. Eye primordia were dissected from embryos at stage 35/36 and plated into 50 mm glass dishes. Samples were visualized using phase contrast illumination on a inverted microscope (Nikon). The Biopen device has four channels which can be loaded with different solutions. For these experiments we loaded the device with ddH_20 (for osmotic shock), fluorescein (to visualise the region of stimulation), and culture media (60% L15 + 1x PSF, as a control). The device was used according to manufacturer instructions, and the 'turning assay' experiment was conducted over approximately 30 minutes of stimulation.

2.7 Note on other pharmacological treatments

Several different pharmacological treatments were used for various experiments. For overnight treatment of eye primordia explant cultures, treatments were added after the explants had been allowed to adhere to the substrate for two hours at room temperature, immediately before placing them in the incubator.

2.8 Immunocytochemistry (ICC)

Cultures were fixed in 2% PFA + 7.5% sucrose (the sucrose prevents osmotic disruption of the neurons) for 20 minutes and then washed with PBS. Cultures for which the membrane was permeabilised were then incubated for 5 minutes at room temperature with 0.1% Triton-X. If cultures were permeabilised, all washing steps from this point used PBS + 0.001% Triton-X (PBST); cultures that had not been permeabilised were washed with PBS without Triton. All cultures were then blocked for 45 minutes at room temperature in 5% Goat serum in PBST (permeabilised), or PBS (non-permeabilised). After thorough washing, the primary antibody diluted in blocking solution was added and cultures incubated overnight at 4°C. Cultures were washed again and then incubated for 45 minutes at room temperature with the secondary antibody again diluted in blocking solution. If phalloidin was used to stain actin, after two short washes, cultures were incubated for 5 minutes in alexa fluor 488 conjugated phalloidin (ThermoFisher A12379). Cultures were then washed thoroughly with PBS or PBST, and mounted on coverglass with a drop of Fluoromount-G (ThermoFisher). For the experiments involving ODQ treatment, 200 nM or 500 nM ODQ was added 30 minutes prior to fixation.

Table 5: Antibodies

In the following table, Gt = goat, Rb = rabbit, Ms = mouse, AF = Alexa Fluor®.

Antibody	Dilution
Proteintech 60067-1 Ms α neuropilin-1, extracellular epitope	1:500 (1:100, high concentration mentioned in text)
ABCAM, ab81321* Rb α neuropilin-1, intracellular epitope	1:100
Proteintech 10135-1-AP* Rb αVAMP2 antibody	1:400
Abcam 12416 Rb α cGMP (antibody no longer available from manufacturer)	1:30
Abcam 150115, Gt α Ms IgG AF 647	1:1000
Abcam 175471 Gt α Rb IgG AF 568	1:000
Abcam 175660	1:1000

Gt α Ms IgG AF 405	
Abcam 175471 Gt α Rb IgG AF 568	1:1000

*aliquots of indicated antibodies were a gift from Roberta Cagnetta (Holt Lab)

2.9 Optical imaging assays

2.9.1 Imaging of ICC experiments

For imaging fixed cells on hydrogels, the coverslip containing the hydrogel was inverted over a drop of fluoromount-G onto a glass-bottom dish. Cells were then imaged on an inverted microscope through the glass.

Immunostainings for cGMP:

Imaging was conducted on a Zeiss inverted microscope equipped with a metal halide lamp (Zeiss) and a 63x N.A. = 1.4 oil immersion objective. Images were collected via a sCMOS camera (Andor, Zyla 4.2). Settings (exposure time and lamp intensity) were established at the beginning of each imaging session and maintained constant throughout.

Growth cones were selected under bright field. Isolated growth cones that did not appear to have been disrupted during the fixation and staining process were selected. Two dishes were always prepared for each condition. Where possible, growth cones were imaged from a minimum of 3 separate explants in each dish.

Immunostainings for neuropilin-1 and VAMP2:

Imaging was conducted on an inverted microscope (Leica) equipped with a metal halide lamp (Leica) and a 63x N.A. = 1.4 oil immersion objective. Images were collected via a sCMOS camera (Hammasatu Orca-Flash 4.0). Settings (exposure time and lamp intensity) were established at the beginning of each imaging session and maintained constant throughout.

Growth cone selection was completed as above. Where dual channel imaging was conducted (i.e. in the neuropilin-1 staining experiments) control images were taken to ensure that there was no bleed through between channels.

2.9.2 Imaging of TMR-dextran loaded growth cones for morphological analysis

TMR-Dextran containing growth cones were imaged live. Imaging was conducted on an upright Nikon microscope equipped with a xenon arc lamp (Sutter Instruments, USA) , a 60x/N.A. = 1 dipping objective, standard DSRED filter set, and CCD camera (Andor iXon). Isolated growth cones were selected for imaging, similarly to growth cone selection for ICC experiments.

2.9.3 Calcium imaging

Calcium imaging of explants from jRCaMP1b injected embryos was conducted using a Nikon upright microscope equipped with an CCD camera (Andor, UK) and a xenon arc lamp (Sutter Instruments, USA), and a 60x/N.A. = 1 dipping objective. Images were taken every 2-3 seconds, with large exposure times (300-500 ms) and low illumination intensities, as these were the conditions which were found to optimize neuron survival during long imaging periods. All calcium imaging experiments were conducted in standard culture media which contains 2 mM Ca^{2+}.

2.9.4 Membrane potential dye imaging

The membrane potential dye (MPD) used was Component A from the FLIPR Membrane Potential Assay Kit Red (Molecular Devices). The aliquot used was a kind gift from Benjamin Gaub (ETH Zurich).

The stock was diluted in 10 mL of Live Cell Imaging Solution (LCIS, Invitrogen,**),** and aliquots frozen. For imaging, this stock was added at 1:125 concentration to *Xenopus* RGC cultures from stage 35/36 embryos. For these experiments embryos were cultured on ‘two-stiffness’ gels, so that both stiffness could be imaged in the same dish. Immediately before imaging *Xenopus* culture media was exchanged for LCIS, MPD was then added, and allowed to incubate for 15-20 minutes at room temperature. Imaging was conducted with the same microscope, lamp, and objective as the calcium imaging above.

2.9.5 Calpain activity assays

These experiments used explants from stage 35/36 embryos cultured on glass for ~20 hours.

Calpain activity was assayed using the fluorogenic protease substrate CMAC, *t*-BOC-Leu-Met (7-Amino-4-Chloromethylcoumarin, *t*-BOC-L-Leucyl-L-Methionine amide),

referred to as *t*-BOC (ThermoFisher). 10µM *t*-BOC was added to cultures. Imaging was conducted on an inverted Leica microscope using a 60x N.A. 1.4 objective and sCMOS camera (Hammasutu Orca-Flash 4.0). Illumination was provided by a metal halide lamp (Leica) and the signal filtered through a standard DAPI filter set.

For control experiments, assays were conducted in the presence of 1 µM Calpastatin peptide (CPI), a cell-permeant peptide that inhibits both m and µ- calpain. For these experiments, the culture media was doped with 0.01% Pluoronic^{TM} F-127 (ThermoFisher), to increase cell permeability. This was not used in experiments excluding CPI, as it was not needed for *t*-BOC entry into the cells, and was observed to have mildly adverse effects on cell survival (observational, data not shown).

For experiments studying the effect of Yoda1 on Calpain, 2.5 µg/mL Yoda1 or a mock solution was added to the culture simultaneously with the *t*-BOC.

2.10 FliptR experiments

Xenopus eye primordia explant cultures from stage 35/36 embryos were cultured for 24 hours. Flipper–TR (Spirochrome) was added at a final concentration of 1 µM. Cultures were incubated with the probe for 30 minutes before imaging, and the probe was not washed out prior to imaging.

FliptR incubated samples were imaged on an upright two-photon microscope (LaVision) in the Cambridge Advanced Imaging Centre. Analysis was conducted using FLIMfit[188]. Imaging experiments were conducted mainly by Ryan Greenhalgh and Kevin O'Holleran, and analysis was conducted by Ryan Greenhalgh.

2.11 Optical tweezer experiments

Optical tweezers measurements were conducted in collaboration with the lab of Ulrich Keyser at the Cavendish Laboratory at Cambridge. The microscope used for the experiments was custom built by Jeffrey Mc Hugh and Professor Kurt Andresen (Visiting Professor Cavendish Laboratory, Gettysburg College) to enable both optical tweezers measurements and fluorescence imaging of axons. The portion of this section pertaining to the technical specifications of the optical tweezers setup was written with significant assistance from Jeffrey Mc Hugh. An overview of the imaging setup can be seen in Figure 2.1. Optical tweezers were formed by focusing a 1064nm infra-red laser though a 60x NA 1.2 objective (Olympus, Japan). The setup is directly illuminated from above with a white

light source (Edmund Optics, USA). The position of the particle is monitored by a CMOS camera (Mikrotron, Germany). The camera uses a previously described autocorrelation method[189] to track bead position at 500 fps with sub-pixel accuracy. Position is converted to force through the stiffness, k = 0.1 pN nm^{-1}, of the optical trap, which is determined by fitting a Lorentzian function to the power spectral density of the stochastic motion of a trapped bead. The beads could be simultaneously visualized using a separate CCD camera.

Explant cultures from stage 35/36 embryos were prepared on no. 0 coverslips. For these experiments, explants from embryos injected with 0.2% TMR dextran were used to enable visualization of the axons. To pull tethers, 2 µm diameter streptavidin coated polystyrene beads (Kisker, Germany) were incubated with biotinylated Concanavalin A (conA, Vector Laboratories) which adheres strongly to sugars exposed on cell membranes[190]. Single beads were captured in an optical trap and moved into position over an axon. Beads were touched to the axon to allow them to stick to the membrane, which could be seen via a reduction in the Brownian motion of the bead. To pull the tether, the sample was then moved using a piezo stage at a speed of 0.0005 µm ms^{-1} over a distance of 10 - 20 µm. The bead position was continuously recorded throughout the experiment. As the position of the trap was constant, the force exerted on the trap could then be calculated simply as $F = k\Delta x$. Where Δx is the deflection of the bead position from the known trap location. Following tether pulling, the stage was raised until that the bead stuck to the gel (which they did readily), so that the stage could be moved into a good position to capture fluorescence images.

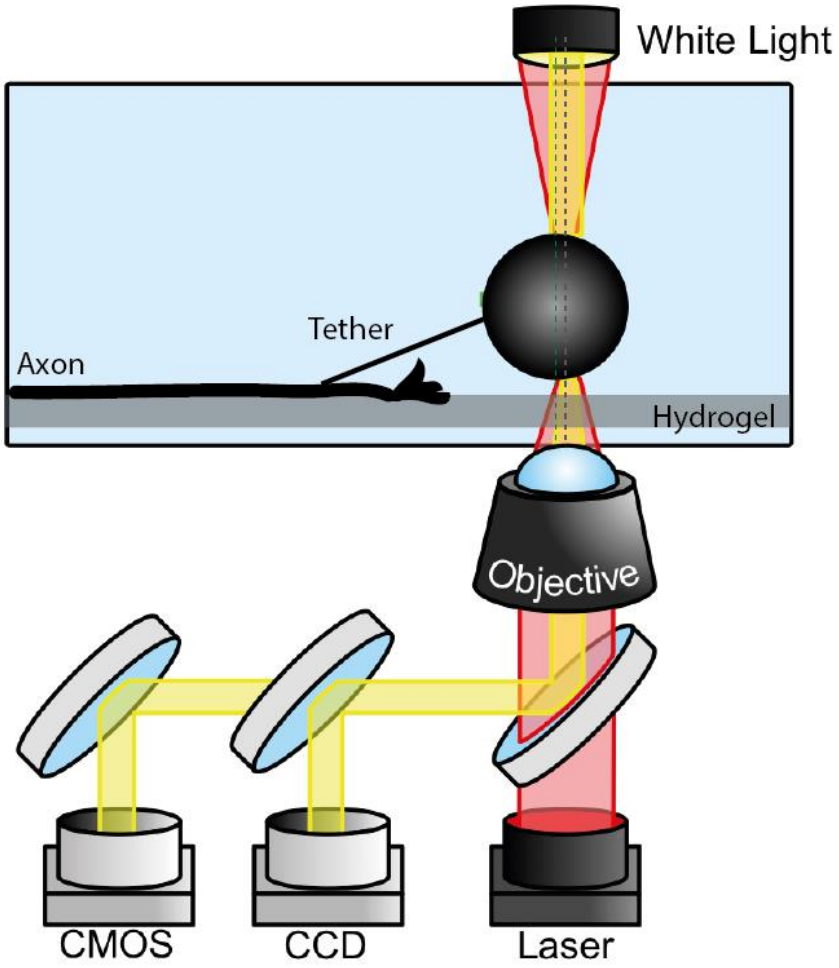

Figure 2.1: Optical tweezers setup for membrane tension measurements

Figure 2.1: (continued)

The majority of this figure was drawn by Jeffrey Mc Hugh. An optical trap formed by focusing an infrared laser through an objective is used to pull tethers from RGC axons grown on compliant hydrogels. Bead position is monitored via white light transmitted to a CMOS camera, and biological structures were visualised in bright field via a CCD camera. The bead is pulled slightly out of the trap by the tether (compare the green dashed line indicating the bead centre, and the grey dashed line indicating the trap centre) The force F exerted by the tether on the trap can then be calculated with the spring constant k of the trap.

Data processing and analysis of optical tweezers data was conducted by Jeffrey Mc Hugh.

2.12 Patch clamp electrophysiology

The patch clamp setup used for these experiments was built by Hélène Gautier.

Cultures of *Xenopus* RGCs from stage 35/36 embryos were prepared. Immediately prior to experiments, *Xenopus* culture media was exchanged for an external solution comprising: 115 mM NaCl, 4 mM KCL, 5 mM HEPES, 10 µM Glycine, 10 mM Glucose,

3mM $CaCl_2$, and 3 mM $MgCl_2$, adjusted to pH 7.2, 250 mOsm. Cells were visualized on an inverted microscope (Zeiss).

Glass capillaries (1.5 OD x 0.86 ID, Harvard Apparatus) were pulled to a resistance of approximately 15-18 MΩ, and loaded with an internal recording solution comprising: 100 mM potassium gluconate, 8 mM KCL, 5 mM NaCl, 1.5 $MgCl_2$, 20mM HEPES, 10 mM EGTA (pH 7.2), 2 mM ATP, 0.3 mM GTP, 2 mM Lucifer Yellow, adjusted to pH 7.2, 250 mOsm.

Currents were recorded after seal formation using an EPC10 USB (HEKA) digital amplifier, controlled via PatchMaster software (HEKA).

All recordings were made in whole cell mode. Resting membrane potential was recorded over extended measurements in current clamp. Prior to and following each membrane potential recording, the health of the cell and seal was assessed by running a voltage ramp protocol in voltage clamp mode, wherein the voltage was increased in 10 mV steps from -60 mV to +30 mV (see also Figure 4.6). Recordings in current clamp were recorded at a sampling frequency of 20 kHz, IV traces in voltage clamp were sampled at 50 kHz.

2.13 Analyses

All custom written MATLAB (Mathworks, USA) scripts are available on the Franze Lab Github or in the appendix to this thesis.

2.13.1 Sholl analysis

Sholl analysis was completed in FIJI using the Sholl Analysis plugin[191]. Briefly, images were filtered through the a FFT bandpass filter (FIJI) to correct for uneven background illumination, and were then manually thresholded in FIJI. A circle was fit to the explant, which the outer radius of the circle ($r = \sqrt{Area/\pi}$) set as the starting radius of the analysis. The outer radius of the analysis was set as a point beyond the reach of the longest axon from the explant under consideration. Circles were drawn with 5 µm spacing.

Data here are shown both as profiles (a plot of distance from explant vs number of axons/axon bundles crossed at that distance), and as ‘median outgrowth radius’. The later was calculated as the median radius at which an intersection was reported for that explant.

2.13.2 Intensity analyses

For the analysis of intensity values from growth cones stained with antibodies or loaded with fluorescent dextran, first a background region was selected from each image and the average intensity in this region subtracted for each image. Growth cones were then segmented in a semi-automated manner. Fluorescence intensity/unit area was then calculated for this segmented region.

For analysis of membrane potential dye and t-BOC assays, a 'background' region was manually selected from each image, and the background subtraction was completed as in the preceding analysis. Lines were drawn across axons or filopodia, thickened to approximately 11 px. Intensity profiles were taken and averaged over the line thickness.

This mean intensity profile was fit to a Gaussian function $I = \alpha e^{\left(-\left(\frac{x-\beta}{\gamma}\right)^2\right)} + B$, where α, the height of the Gaussian was then used to represent the intensity of that axon/filopodium. See explanatory diagram in Figure 4.7.

2.13.3 Statistics

Data were assessed for normality with a one-sample Kolmogorov-Smirnov test. If data distributions were not found to deviate significantly from normal, and one or two conditions were compared, comparisons were made with a one or two sample t-test; otherwise a Wilcoxon rank sum test was used. In the case that more than two groups were compared, data was analysed with an ANOVA followed by a Bonferroni post-hoc test.

Collapse assay data was assessed using χ^2 tests.

N-numbers, and numbers of biological replicates are stated explicitly in the captions of each figure.

3 SUBSTRATE MECHANICS ALTERS THE NEURONAL RESPONSE TO SEMA3A

3.1 Introduction

The influence of guidance cues on neuronal growth cones has been studied primarily in *in vitro* culture conditions, using neurons cultured on glass or tissue culture plastic. Such assays have proven enormously useful at isolating the influence of individual chemical cues; however, they also place growth cones in a very specific, catastrophically non-physiological mechanical environment. Glass and plastic reach into the gigapascals in elastic modulus, many orders of magnitude stiffer than the soft brain tissue which comprises these cells' *in vivo* surroundings[192].

The following chapter addresses whether substrate stiffness by itself modulates how growth cones respond to the chemical guidance signal Sema3A.

3.2 The collapse response to Sema3A is reduced on soft substrates

I assayed the response of *Xenopus* RGCs grown on polyacrylamide substrates of different stiffnesses to the guidance cue Sema3A. Hydrogels were fabricated with shear (storage) moduli (G', see Section 1.3.1 for definitions of mechanical terms and units) of 100 Pa and 1 kPa, my 'soft' and 'stiff' conditions respectively. These stiffnesses were selected due to their proximity to the *in vivo* lower and upper bounds of embryonic *Xenopus* brain tissue elasticity[123].

Collapse assays have been used extensively to identify guidance cues[193] and to dissect neuronal responses to chemical guidance signals such as semaphorins[115,194] and ephrins[195,196]. In this experiment, a bulk concentration of a cue is applied uniformly to a population of axons, which are then fixed after a set amount of time. If the growth cones express a receptor that induces a repellent response to the cue, filopodia retract and the lamellipodial actin meshwork is disassembled, a process driven by cytoskeletal

modulators[56] as well as massive endocytosis[51–53], and referred to as growth cone collapse. The proportion of growth cones that collapse is taken to indicate how strongly a population of cells responds to the guidance cue. In the following experiments, 'Collapsed' growth cones are defined as those exhibiting two or fewer filopodia and no visible lamellipodia (Figure 3.1A).

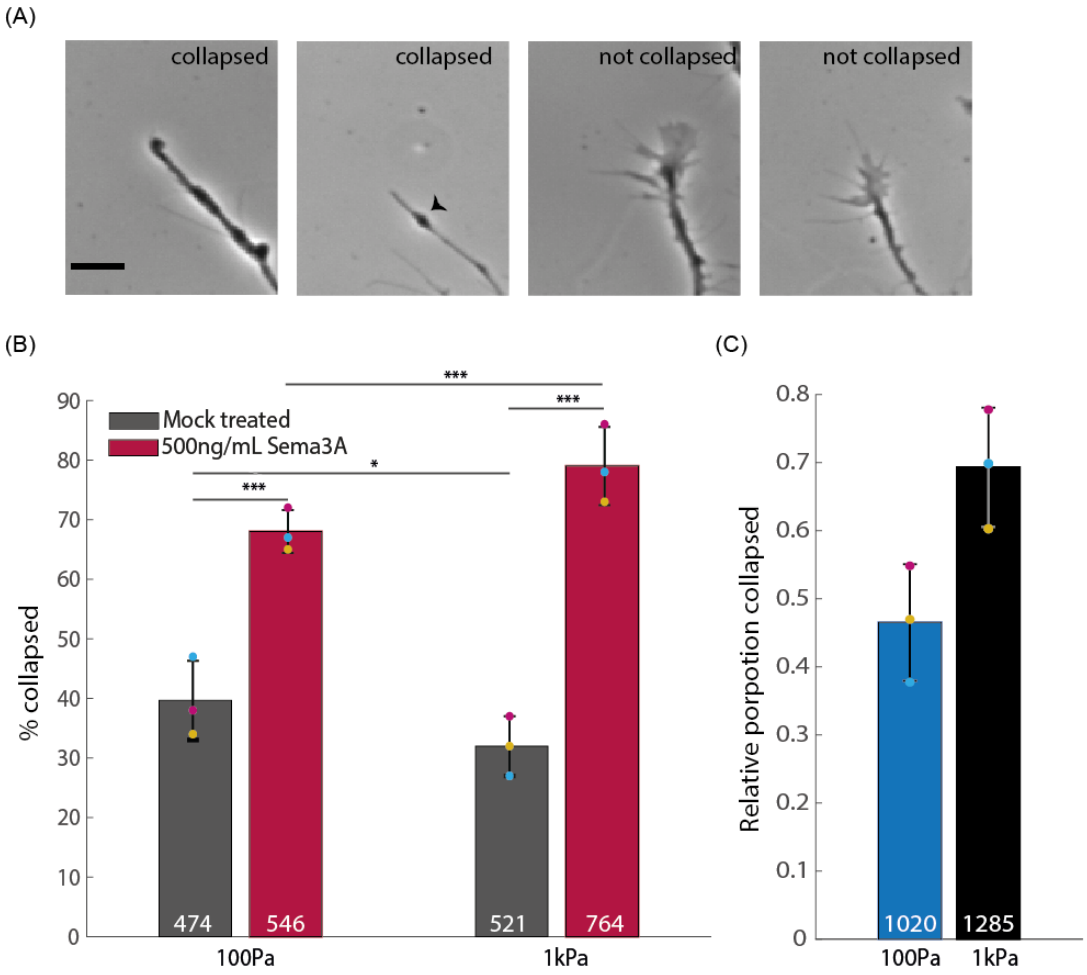

Figure 3.1: RGC growth cones collapse less in response to Sema3A on soft substrates.

Figure 3.1: (continued)

*Collapse assays reveal a reduced response to Sema3A in RGC growth cones cultured on soft, as compared to stiff, substrates. (A) Examples of collapsed (two left) and un-collapsed (two right) growth cones from a culture grown on a soft gel. Scale is 20 μm. The second collapsed growth cone displays a characteristic retraction bulb (arrow head). (B-C) Collapse assays on soft and stiff substrates. (B) Mock (vehicle) and 500 ng/mL Sema3A conditions are shown separately. Bar height represents the mean of three independent experiments. Collapse proportions for each of the three replicates are scattered on the bars and colour-coded by experiment. Numbers on bars indicate total number of growth cones counted for that condition from all experiments. Error bars represent the standard deviation among the three proportions. P-values in (B) result from Pearson Chi-Square tests conducted on pooled growth cone numbers. A table containing all χ^2 statistics and p-values can be found in Appendix 3.1 (Table 8). For the comparisons shown on the plot: $p_{softS3A\text{-}stiffS3A} = 2.8e^{-05}$, $p_{softS3A\text{-}softMock} = 3.5e^{-22}$, $p_{stiffS3A\text{-}stiffMock} = 7.4e^{-66}$, $p_{softMock\text{-}stiffMock} = 0.015$. (C) The same data is displayed as proportion collapsed relative to control, calculated as $\frac{\%collapsed_{Sema3A} - \%collapsed_{mock}}{100 - \%collapsed_{mock}}$. Bar heights, error bars, and data points from each replicate are presented as in B. Numbers on the bars are total growth cone numbers, in this case the sum of the growth cone numbers in the Sema3A and control condition for the relevant stiffness. *p<0.05, ***p<0.001.*

A significantly smaller proportion of growth cones collapsed in response to the same dose of Sema3A when grown on 100 Pa substrates than when grown on 1 kPa substrates (Figure 3.1 B,C). On stiff substrates, an average of 79% of growth cones collapsed in response to 500 ng/mL Sema3A applied for 10 minutes, whereas 68% did so in the soft condition. For clarity here collapse proportions are presented both as raw proportions and as the relative proportion collapsed, quantified as $\frac{\%collapsed_{Sema3A} - \%collapsed_{mock}}{100 - \%collapsed_{mock}}$. By taking into account the proportion that collapse under mock treated conditions, this metric reflects the proportion that collapse out of the growth cones that are actually available for collapse. Applying this metric, the relative collapse proportions were on average 0.47 on 100 Pa substrates and 0.69 on 1 kPa substrates.

3.2.1 Experimenter bias in counting collapse assays does not alter results

Growth cones were counted manually in the collapse assays. While all assays were initially blinded, it was in many cases obvious whether a dish had been exposed to Sema3A, particularly on stiff substrates. Moreover, explants grown on 100 Pa and 1 kPa substrates have very different characteristic morphologies (See Figure 1.8). It was therefore usually impossible to remain fully blinded for the duration of the counting. To confirm that experimenter bias had not distorted these results, I tested the effects of fully blinding the experiment. I conducted collapse assays on 100 Pa, 1 kPa, and 10 kPa substrates, and took phase contrast images of the growth cones around each explant during the counting. The captured regions were sufficiently small that neurite morphology could not be used to determine the substrate or condition. I randomized the images,

counted growth cones a second time, and compared the randomized results to my initial counts (Figure 3.2). The initial (not blinded) count classified 66%, 83% and 87% of growth cones as collapsed on 100, 1 kPa, and 10 kPa substrates respectively. The blinded count classified 76%, 92%, and 91% in the same conditions.

These results indicate that the difference in collapse proportion on different substrates is not an artefact of experimenter bias. There was a trend towards counting more growth cones as collapsed in the blinded conditions: counting from images rather than on the microscope means that one is restricted to a single focal plane. Filopodia are very thin, and even slightly out of focus filopodia might have therefore been not seen, leading to more growth cones categorized as collapsed.

Additionally, there was very little difference in collapse proportion between populations cultured on 10 kPa gels and 1 kPa gels. This is consistent with the weak traction forces exerted by neurons[197], which should preclude them from sensing differences between two very stiff substrates.

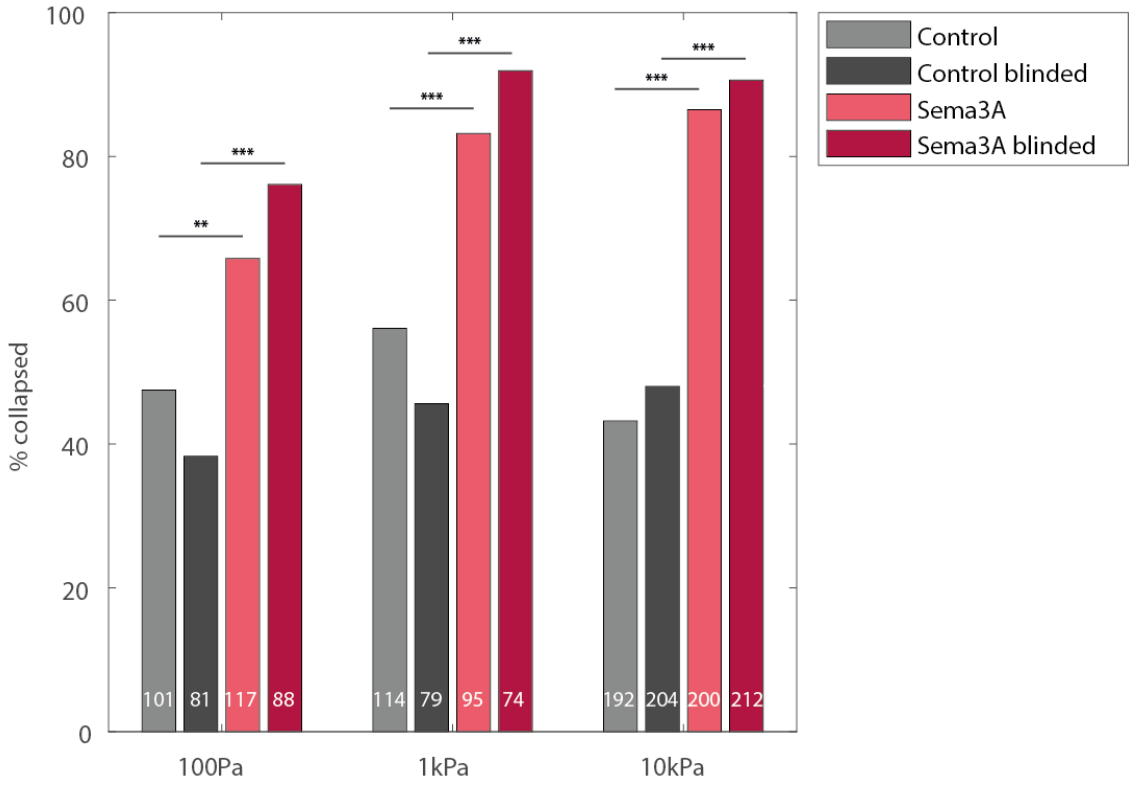

Figure 3.2: Blinded and not blinded collapse assays show similar results

Figure 3.2: (continued)

Xenopus RGC growth cones were collapsed with 400 ng/mL Sema3A. Numbers on bars indicate total number of growth cones counted for that condition. A total of 819 and 558 growth cones growth cones were counted in the not blinded and blinded conditions, respective. Note that there was only one replicate of this experiment. For clarity, not all significant statistical comparisons have been presented on the figure. A table of all comparisons can be found in Appendix 3.1 (Table 7). No comparisons between blinded and not blinded conditions for same group (substrate stiffness and sema3A/mock) were significant though this could be due in part to low growth cone numbers in the blinded condition. P-values result from Pearson Chi-Square tests. For the significance bars displayed on the graph; for not blinded tests: $p_{100PaS3A\text{-}100PaMock} = 6.5e^{-03}$, $p_{1kPaS3A\text{-}1kPaMock} = 2.9e^{-05}$, $p_{10kPaS3A\text{-}10kPaMock} = 2.3e^{-19}$*; for blinded tests:* $p_{100PaS3A\text{-}100PaMock} = 6.3e^{-07}$, $p_{1kPaS3A\text{-}1kPaMock} = 8.4e^{-10}$, $p_{10kPaS3A\text{-}10kPaMock} = 3.9e^{-21}$*. *p<0.05, ** p< 0.01, ***p<0.001.*

3.2.2 Stiffness-dependence of the collapse response persists at both high and low Sema3A concentrations

It has been proposed that Sema3A can induce growth cone collapse via at least two distinct mechanisms, and that the concentration of Sema3A is important in determining which signalling pathways will be activated. In particular, at low concentrations of Sema3A, the response is strongly dependent on local protein synthesis, whereas this requirement diminishes at higher Sema3A concentrations[198].

My initial experiments were conducted at a high concentration of Sema3A, 500 ng/ml, that induces very high rates of collapse. As lower concentrations of Sema3A are likely to be more physiologically relevant, and to explore whether the substrate-stiffness effect was more or less pertinent to one of these signalling pathways, I performed additional collapse assays with 150 ng/ml of Sema3A. As expected, a smaller proportion of growth cones collapsed at the lower Sema3A concentration; however, the effect of substrate stiffness was maintained. At the lower concentration, the relative proportion of growth cones collapsing on soft substrates was on average 0.3, compared with 0.5 on stiff substrates (the raw rates of collapse were 58% vs 66% of growth cones collapsing on soft and stiff substrates respectively) (Figure 3.3).

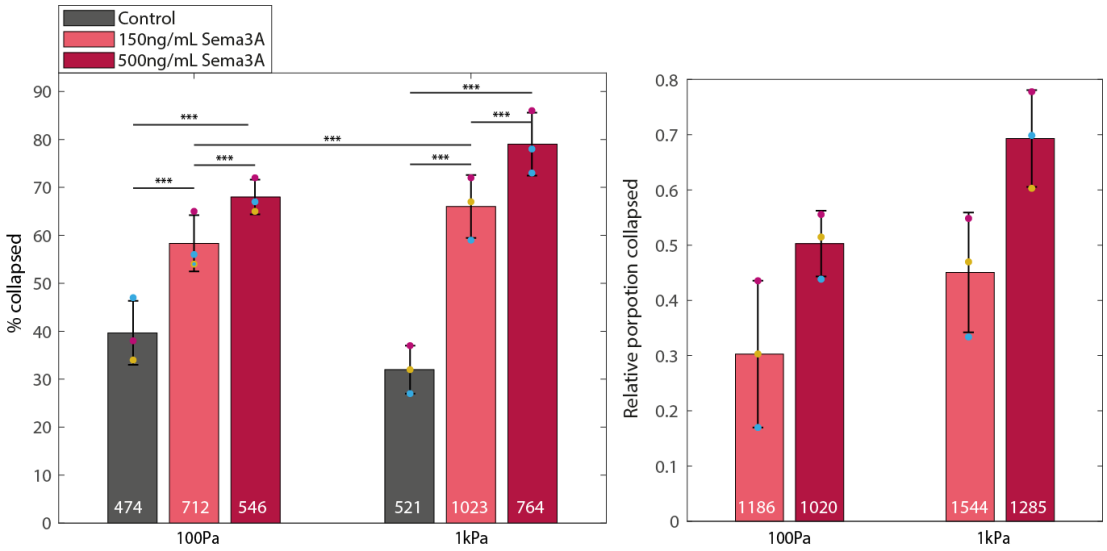

Figure 3.3: Substrate stiffness influences the collapse response at both high and low Sema3A doses

*Collapse assays with different concentrations of Sema3A indicate that substrate stiffness influences growth cone collapse to a similar degree across a range of doses. The data for the 500 ng/mL condition is identical to that in Figure 3.1. Left panel: data are shown as percent collapsed. Right panel: data are shown as relative proportion collapsed. For both plots, data points for each of three biological replicates are scattered on the plots and colour-coded by experiment. Numbers on bars indicate the total number of growth cones counted from all experiments for that condition. Bar heights indicate the mean, and error bars represent the standard deviation among these three measurements. P-values on the left plot result from a Pearson Chi-Square test conducted on pooled growth cone numbers. For clarity, not all significance bars are shown on the figure. A table containing all χ^2 statistics and p-values can be found in Appendix 3.1 (Table 8). In addition to values listed in the legend of Figure 3.1 for the 500 ng/mL data: $p_{softS3A\_150\text{-}stiffS3A\_150}$= 0.0002, $p_{softS3A\_150\text{-}soft\_Mock} = 1.6^{e\text{-}12}$, $p_{stiffS3A\_150\text{-}stiff\_Mock} = 1.9e^{-43}$, $p_{softS3A\_150\text{-}softS3A\_500}$ = 0.00067, $p_{stiffS3A\_150\text{-}stiffS3A\_500} = 3.5e^{-07}$. ***p<0.001.*

3.3 Asymmetric stimulation with Sema3A

3.3.1 Turning assays

Collapse assays are very useful at obtaining a gross estimation of changes in the responsivity of cells to Sema3A. However, they can only provide a limited amount of information as the readout of a collapse assay is binary (collapsed or not collapsed) whereas growth cone responses are very complex. Another assay, often used in parallel with collapse assays, is the turning assay[43,115,199]. In turning assays, guidance cues are applied asymmetrically, with a lower concentration of cue reaching the growth cone. This more closely mimics how Sema3A and other secreted guidance cues are presumed to function *in vivo*[200].

In the classical turning assay, a gradient of the cue is established by repeated pulsatile ejection of tiny volumes from a glass micropipette (Figure 3.4A). Under traditional culture conditions, on a glass substrate functionalised with laminin, *Xenopus* RGCs respond to Sema3A by adjusting their growth trajectory ~15-20° away from the source of Sema3A[115].

During my MPhil research in 2014, I began a series of turning assays using RGCs cultured on 300Pa hydrogels or on glass substrates. Initial results suggested a trend towards reduced turning angles for axons grown on the soft substrates, which seemed to exhibit an attenuated, though still repulsive, turning angle as compared to those grown on glass (these data are reproduced from my MPhil thesis in Figure 3.4B).

Turning assays have been crucial for many seminal discoveries in the axon guidance field; however, they are also problematic, particularly if one wishes to make detailed quantitative comparisons among conditions[201]. In particular, they have a very low throughput, as the dish is quickly contaminated with whatever simulant is used in the pipette. Even more concerning, the absolute concentration and gradient of the cue experienced at the growth cone is strongly influenced by parameters that are difficult to control, such as small differences in pipette tip aperture and smoothness, and the height of the pipette above the dish[201]. An additional concern with hydrogels is that, in contrast to glass, the surface above which the chemical is dispensed is permeant, which may additionally disrupt fluid flow and/or adsorb some of the guidance signal. While early turning assay results were promising, the experiments were not sufficiently numerous or controlled to draw precise conclusions.

In a first attempt to gain a more controlled environment I built a turning assay setup on a fluorescence-enabled microscope with the aim of including a fluorescent label to allow me to visualize the gradient of guidance cue produced in each experiment. I tested this setup with fluorescent dextran of different molecular weights. However, there was large variation in the reliability of the gradient, and fluorescent dextrans of different molecular weights exhibited very different behaviours, confirming the concern that the actual gradient generated in this system is difficult to predict (Figure 3.4C).

3.3.2 Biopen trial

An alternative approach is to avoid diffusion-controlled gradient formation completely using a microfluidic option. The Biopen (Fluicell AB), is a small microfluidic system

designed for precise stimulation of a cell or group of cells. It has several advantages for our purpose: the solution is ‘vacuumed’ back into the device, meaning that an indefinite number of assays can be conducted in the same dish. The Biopen also allows stimulation with a precise concentration and localisation of the cue. As the device does not rely on diffusion, the concentration does not need to be estimated, and the size and charge of the stimulant are irrelevant (Figure 3.4D)

I conducted preliminary tests with the Biopen at the Fluicell office in Gothenburg, Sweden, with the technical advice and assistance of Daniel Fjällborg and Matija Rojnik. These tests proved promising, and we induced directed turning of an RGC growth cone in response to an osmotic gradient by positioning the growth cone at the edge of the regions of stimulation (Figure 3.4E). There was not sufficient time to repeat Sema3A turning assays with this device prior to the submission of this thesis. These experiments are ongoing.

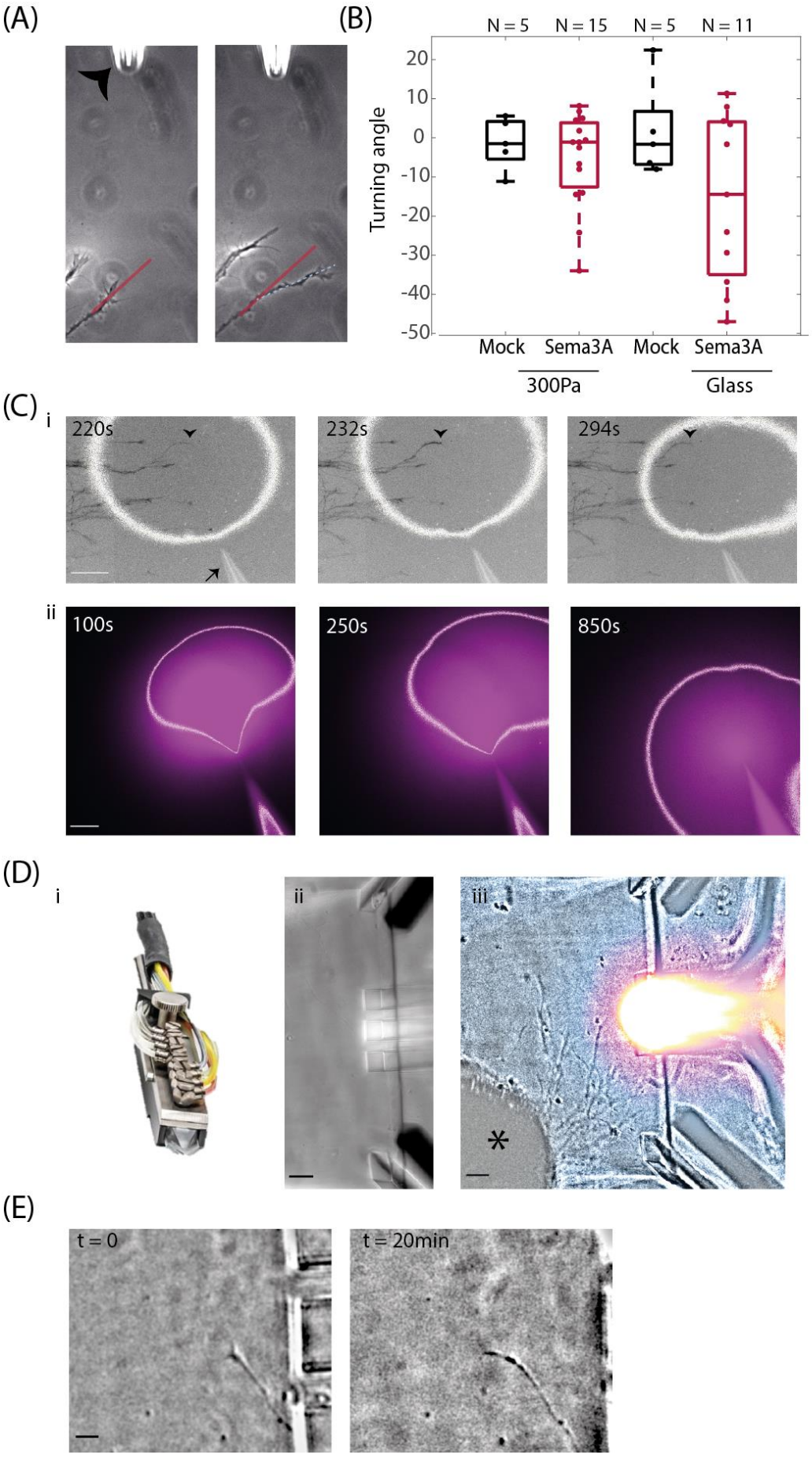
(A)
(B)
N = 5
N = 15
N = 5
N = 11
Turning angle
20
10
0
-10
-20
-30
-40
-50
Mock
Sema3A
Mock
Sema3A
300Pa
Glass
(C)
i
220s
232s
294s
ii
100s
250s
850s
(D)
i
ii
iii
(E)
t = 0
t = 20min

Figure 3.4: Turning assay optimisation and Biopen trials

Preliminary turning assays suggest that Sema3A is may be less strongly repellent for growth cones cultured on soft substrates. (A) The classical turning assay: growth cones cultured on glass turn away from a Sema3A source. Sema3A is dispensed from a glass capillary (black arrow, left image) positioned ~100 µm from the growth cone. After ~1 hour of growth, the growth cone's final trajectory (light blue dashed line in right panel) is compared to its initial growth trajectory (red line), to give a turning angle. (B) Turning assays on glass and 300 Pa substrates. Turning angles were assessed after ~1 hour of stimulation. Negative turning angles indicate turning away from the pipette, positive angles toward the pipette. Note the high variability of turning angle. Each dot represents the turning angle of a neurite exposed to either Sema3A or a vehicle control, and the total number of neurites (N) is stated above each boxplot, data come from experiments conducted over 8 separate experimental days. No significant differences were found between groups (ANOVA, p= 0.14). ***These experiments were completed during my MPhil thesis*** *(Ci) Stimulation of RGCs from a needle (arrow, first image) loaded with Sema3A and a 3 kD fluorescein-tagged dextran. The white outline indicates the area filled by dextran fluorescence ('edges' LUT in Fiji). Neurites express a genetically encoded calcium indicator (jRCaMP1b); the LUT is inverted such that darker colours indicate higher calcium concentrations. The neurite indicated with a black arrowhead makes a calcium transient, possibly in response to Sema3A. Scale is 50 µm. (Cii) Imaging fluorescent dextrans of different molecular weights reveals high levels of variability in the setup: the shape of the gradient was unstable, and also varied depending on the molecular weight of the dextran, as would be expected for a facilitated diffusion process. The needle was loaded with 150 kD Tetramethylrhodamine (TMR)-dextran (magenta) and 3 kD fluorescein-dextran (white outline). Scale is 50 µm. (D) The biopen device; (Di) image from Fluicell website (*https://fluicell.com/products-fluicell/biopensystems/*) showing the Biopen tip, (Dii) close up of device tip, and (Diii) positioning of the Biopen tip proximal to an eye primordium (*) from which RGC axons extend. The bright field image has been filtered through a Fourier bandpass filter (Fiji) to make the axons easier to see. The device is dispensing fluorescein (heat map) to visualize the stimulation region. Scale bars are 50 µm. (E) A trial 'turning assay' using the Biopen. In this assay, ddH_20 was used as a guidance cue. The growth cone was positioned at the edge of the biopen stimulation region, and exposed to water for 20 minutes. Water induces an osmotic response in the growth cone and the growth cone turns away. Scale bar is 10 µm.*

3.4 Chapter conclusions and outlook

The data presented here demonstrate that neuronal growth cones respond differently to the chemical guidance cue Sema3A depending on the rigidity of the substrate over which they are growing. This effect persists at both high and low concentrations of Sema3A, and preliminary results suggest that it may also hold true for turning behaviour induced by asymmetric application of Sema3A (which can, to a degree, be thought of as a spatially restricted partial collapse[69,115]).

On soft substrates, growth cones not only collapsed less in response to Sema3A, but also seemed to have an elevated basal rate of collapse. That is, under mock treated conditions there was a higher proportion of collapsed growth cones on soft substrates (39%) than on stiff (31%) ($p = 0.015$). This could relate to the effect of substrate stiffness on growth cone morphology, which will be explored more fully in the next chapter.

Several different mechanisms could explain the reduction in collapse response on soft substrates. One possibility, which is not explored in this thesis, is that substrate stiffness alters the timescale of collapse in response to Sema3A. Growth cone collapse in response to Sema3A is not permanent; growth cones subsequently recover and continue growing. 10 minutes after addition of Sema3A, the point at which growth cones were fixed in the assays presented here, was previously identified as the time point at which maximal collapse was observed[115]. It is possible that the timing of responses is altered so that, at this time point, growth cones on soft substrates either have not yet collapsed to the maximum level, or have already recovered from a very transient collapse. This possibility could be assessed via time lapse microscopy of collapsing growth cones; I have not yet conducted these experiments. For collapse assays, being able to average over an entire dish of neurites is of great importance to the accuracy of the assay. This is due both to high variability to the fact that the guidance cue is pipetted into the dish, which means that there will be some variation regarding when different growth cones encounter the cue and what concentration they initially encounter. Using the Biopen to conduct collapse assays on individual growth cones or small groups thereof would circumvent the latter problem, and allow accurate recording of the temporal dynamics of growth cone collapse in response to specified Sema3A concentrations in well-controlled experimental conditions.

A second possibility is that the neurons that do respond to Sema3A have not changed at all in the degree of responsiveness, but rather that the number of neurons capable of responding (with collapse) to Sema3A has changed. RGs do not represent a biochemically homogeneous population. For example, there is a dorsoventral gradient of ephrin expression in the *Xenopus* retina, and RGCs with cell bodies in different locations in the retina respond differently to application of Ephs[117]. It is conceivable that on soft substrates a proportion of the neurons have lost their responsivity to Sema3A, for example, the proportion of neurons expressing Sema3A receptors might be altered.

Finally, the growth cone population as a whole could be less responsive to Sema3A, due to a global change in the levels of some relevant parameter(s). The fact that Sema3A collapse is affected similarly at different concentrations (when the response is transduced via different intracellular signalling cascade), may indicate that substrate stiffness affects the response at the level of a global parameter which functions upstream of much of the intracellular signalling cascade. Several second messengers have been identified as

critical controllers of the Sema3A response, which would be candidates for such a parameter.

The next section will explore these possible mechanisms and attempt to demonstrate the changes in downstream signalling that may lead to alterations in the response to Sema3A.

4 SUBSTRATE STIFFNESS MODULATES SECOND MESSENGERS CRITICAL FOR RESPONSES TO AXON GUIDANCE CUES

4.1 Introduction

In this Chapter I explored the intracellular changes which substrate stiffness might induce in the growth cone in order to alter the Sema3A response.

I began with a more detailed exploration of differences in growth cone morphology on soft and stiff substrates, in order to first rule out large scale changes in growth cone morphology. I also assessed Sema3A receptor expression.

As my results from these experiments suggested that neither morphological differences nor differences in receptor expression were likely to be the primary cause of the stiffness-dependent alteration of the Sema3A response, I then focused on where the mechanochemical signalling cascade induced by changes in substrate stiffness might converge on the Sema3A signalling cascade. Sema3A stimulation induces a complex sequence of intracellular events, ultimately converging on cytoskeletal modulators to induce the changes in growth cone morphology that lead to collapse or repulsion[56,57,97]. Several 'master regulators' of the Sema3A response have been identified; in particular, these include the levels of intracellular calcium and cyclic nucleotides, as well as membrane potential [44,45,48,84] (See also Section 1.1.4). I therefore continued by measuring basal levels of these parameters as a function of substrate stiffness.

4.2 Growth cone morphology

Many cell types undergo dramatic morphological changes, including flattening and spreading, on stiffer substrates[148,202]. Morphological differences between growth cones

in soft and stiff conditions could complicate the counting of collapse assays. Such changes could also influence the Sema3A response more fundamentally, for example by altering the number of accessible guidance cue receptors. In the case of turning assays, a difference in growth cone area or complexity could affect growth cones' gradient-sensing ability: to sense a gradient, a structure must be able to determine a difference in concentration across its width, which means that larger growth cones could potentially sense shallower gradients[203,204]. Finally, signals transduced from filopodia are thought to be critical for growth cone responses, meaning that lower complexity growth cones with fewer filopodia could be less environmentally sensitive[205–207].

To explore what morphological variation I might observe between growth cones cultured on 1 kPa and 100 Pa substrates, I imaged RGC growth cones from embryos that had been injected with a tetramethylrhodamine (TMR)-conjugated dextran. The dextran should fill the cytoplasm uniformly without specifically interacting with any subcellular structures, an assumption generally supported by the uniform appearance of dextran filled growth cones (Figure 4.1A). Assuming that exocytosis rates are similar on the two substrates, pixel intensity/area serves as a metric of growth cone height, and this did not seem to vary significantly between growth cones from populations on soft and stiff substrates (Figure 4.1B). It should be noted, however, that this assumption does not take into account the potential mechanical regulation of exo/endocytosis rates. The assumption that exo/endocytosis rates are similar on different substrates is nontrivial, and a robust assessment of growth cone height would require either measuring exo/endocytosis rates, or using a method of growth cone height determination that cannot be influenced by cell behaviour, such as volume exclusion of an inert dye or raster scanning with an AFM[208,209]

I used this same dataset to analyse additional aspects of growth cone morphology. Unsurprisingly, growth cones from 1 kPa substrates were slightly larger, with an average spread area of 70 ± 28 μm^2, as compared to 55 ± 22 μm^2 for those on 100 Pa substrates (mean ± standard deviation, Figure 4.1Ci).

I next wanted to determine whether growth cone complexity was affected by substrate stiffness. The ratio of perimeter to surface area, taken as a gross measurement of morphological complexity, was not significantly different between different substrates (Figure 4.1Cii). To look at morphological differences in more detail, I analysed local curvatures of the growth cone outlines. Curvature was calculated approximately every micron along a smoothed growth cone outlines, via a function that fits polygons to sets

of points along the outline and then calculates curvatures from the polygons (LineCurvature2D, Dirk-Jan Kroon).

In Figure 4.1Di, an outline is overlaid over an inverted fluorescence image of a growth cone, and colour-coded to represent positive (blue) and negative (red) curvature. Green lines are surface normals, distributed sparsely for clarity. Note that the initial segmentation used to generate growth cone outlines was not able to capture thin filopodia; therefore, points where filopodia protrude often appear simply as regions of very high curvature. The line at which the growth cone was segmented from the axon shaft was not excluded from the analysis; however, it appears similar in all growth cones and its effect on results was presumed to be negligible.

The mean curvature was similar on soft and stiff substrates. The summed curvature however was higher on stiff substrates, as was the number of times the curvature switched between positive and negative values for a given growth cone, and these two parameters scaled with the length of the growth cone perimeter (Figure 4.1Dii-iii, Figure S 1, Figure S 2). Taken together, these results indicated that growth cones on stiff substrates have a greater spread area, and that the complexity of the perimeter scales with the increasing growth cone size.

Many morphological parameters such as filopodia number and cytoskeletal structure, were not captured by this analysis. More sophisticated analyses, such as machine learning based algorithms[210] or principal component analysis[211], would likely reveal additional differences in growth cone morphology between growth cones on soft and on stiff substrates. Nevertheless, as none of the morphological differences observed by eye or detected by this analysis should preclude growth cones on soft substrates from sensing Sema3A, other factors must contribute to the stiffness-dependent regulation of the Sema3A response.

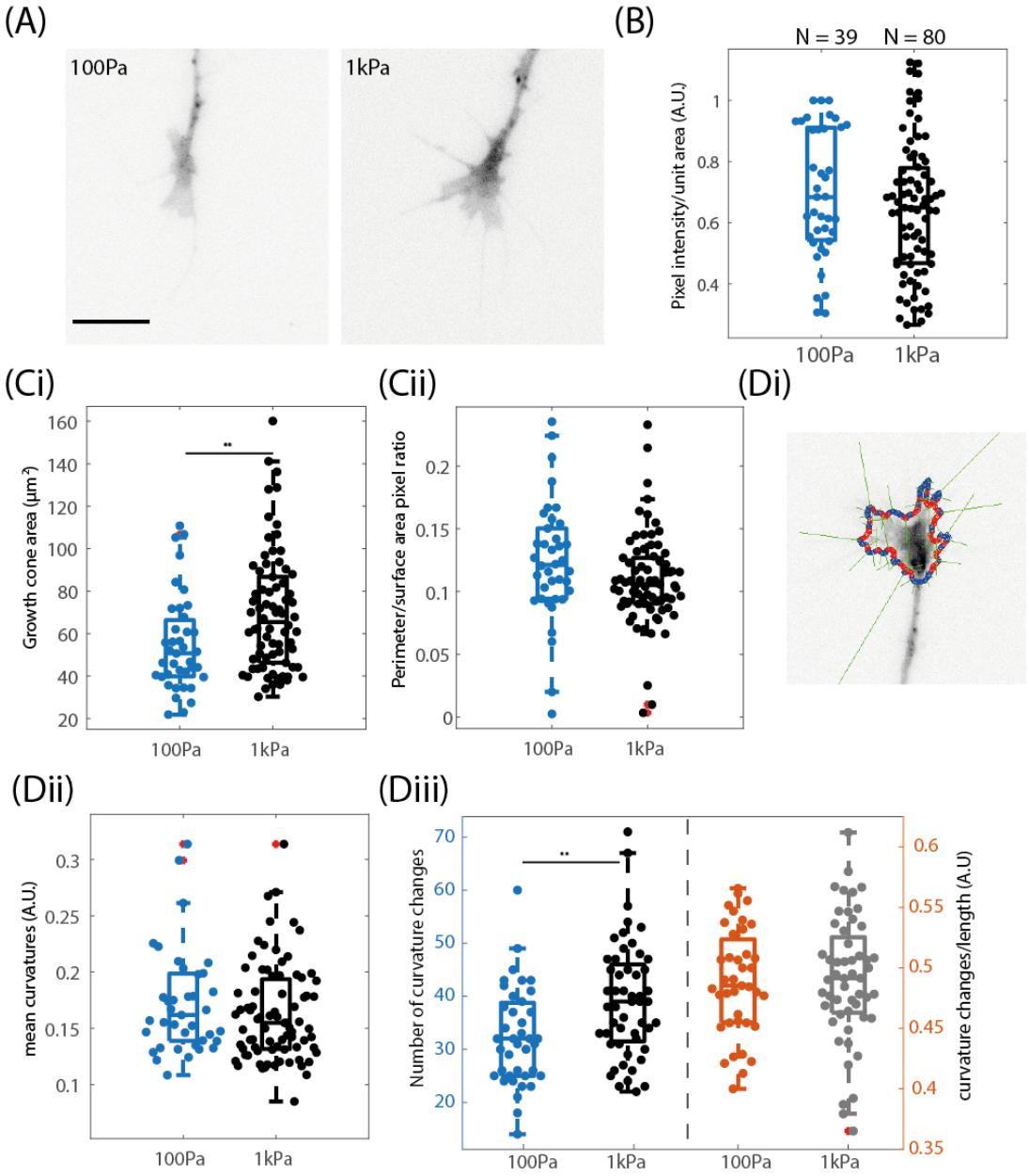

Figure 4.1: Growth cones on 1 kPa substrates are larger than those on 100 Pa substrates

Figure 4.1: (continued)

*Morphology of growth cones cultured on soft and stiff substrates. (A) Example images of TMR-dextran filled growth cones on 100 Pa and 1 kPa substrates. The dark puncta visible in the axons are likely secretory or transport vesicles, which tend to indiscriminately accumulate any injected compound. Scale bar is 10 µm. (B) Pixel intensity/unit area. Each point represents the value for a single growth cone. Mean normalised pixel intensity does not change with substrate stiffness (p = 0.65). Data come from three biological replicates and the numbers of growth cones analysed (N) are displayed above each boxplot. The same growth cones were used throughout the morphological analysis, so these numbers apply to B, C, and D as well. (C-D) Additional morphological analysis (Ci). Growth cone spread area was higher on stiff substrates (p = 0.0051). (Cii) Perimeter to surface area ratio did not differ between growth cones on 100 Pa and 1 kPa substrates (p = 0.073) (Di). Representative dextran filled growth cone showing the principle of the curvature calculation. Perimeters were smoothed, and a curvature value calculated for every 5 points (~every 1 µm) of the outline. The outline on the image shows points at which curvature was determined for this growth cone with red = negative and blue = positive curvature. Green lines are surface normal vectors. (Dii) There was no significant difference between mean curvature values on soft and stiff substrate (p = 0.087). (Diii) The number of curvature inflections was higher on stiff substrates (blue to black bar, p = 0.0021); this difference scaled with outline length, disappearing when the number of curvature inflections was normalised to length (orange to grey bar, p = 0.83). See also Figure S 2. All p-values result from a two sample t-test *p<0.05, **p<0.01, ***p<0.001.*

4.3 Substrate stiffness does not alter neuropilin 1 expression

The minimal Sema3A receptor complex comprises a dimer of Npn1 and PlxA1 trimers[71]. Changes in receptor expression or distribution could alter the ability of neurons to respond to Sema3A; indeed, developmentally regulated increases in receptor expression are responsible for the onset of Sema3A responsivity in *Xenopus* RGCs[115]. Particularly given recent evidence that substrate stiffness alters developmental timescales in neurons (Eva Kreysing, personal communication), changes in receptor expression seemed like a potentially simple explanation for the differing Sema3A response between 1 kPa and 100 Pa substrates.

I therefore used quantitative immunofluorescence (QIF) to analyse levels of Npn1 on soft and stiff substrates. I used two antibodies, both of which identified the correct band in western blots against protein extracts from *Xenopus* head tissue (Figure 4.2C and Max Koppers, personal communication). In addition to total levels of Npn1, I hoped to observe any changes specifically in the membrane associated fraction of Npn1, as Npn1 must be inserted in the membrane to facilitate Sema3A signalling. The two antibodies, denoted Npn1-Int (Abcam) and Npn1-Ex (Proteintech) recognize an intracellular and an extracellular epitope respectively. I stained both permeabilised (5 minutes with 0.1% Triton-X) as well as non-permeabilised growth cones with both antibodies. In permeabilised case, I expected to stain the entire population of Npn1, including that which is not localized to the cell membrane (i.e. not available to bind Sema3A). In the non-

permeabilised case, I expected that most of the antibody would not enter the cell; therefore, I should see staining only with the antibody that binds the extracellular epitope, and it should stain only the fraction of Npn1 that is being presented on the cell membrane.

As can be seen in Figure 4.2Aii, Npn1-Ex failed to stain non-permeabilised growth cones, and this was true even at high antibody concentrations and strong illumination, indicating that perhaps it is not suitable for ICC under these conditions. Staining intensity with Npn1-Ex did not differ between *permeabilised* growth cones on soft and stiff substrates; however, given its failure to stain non permeabilised growth cones this should be interpreted with caution (data not shown). Nevertheless, this antibody worked well in western blots (Figure 4.2C); observationally, there was little difference in Npn1 band intensities in western blots conducted on protein lysates from embryos with impaired mechanosensing (embryos in which the mechanosensitive ion channel (MSC) Piezo1 had been knocked down) (Figure 4.2C). This suggests, at least, that MSC activity is not directly affecting the quantity of Npn1. (The potential influence of MSC activity on the Sema3A response will be the subject of Chapter 5.)

Staining with Npn1-Int was punctate with a diffuse background, an expected distribution for Npn1[115]. Analysis of Npn1-Int fluorescence intensity determined no major difference in mean intensity (averaged over growth cone area) between growth cones cultured on different substrates (Figure 4.2Bii).

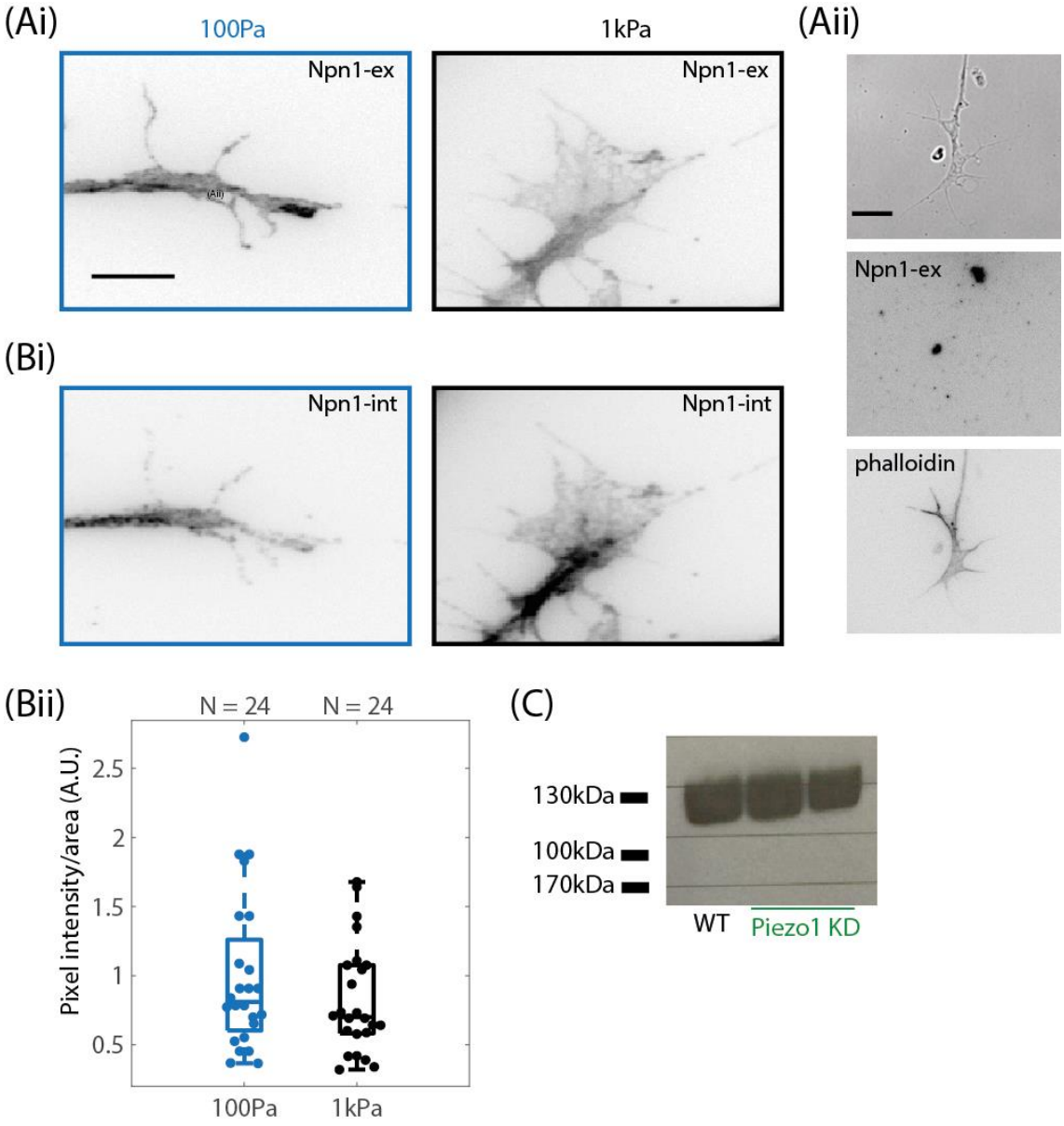

Figure 4.2: Npn1 expression does not vary with substrate stiffness

Figure 4.2: (continued)

Mean fluorescence intensity of Npn1 staining did not vary between growth cones cultured on soft and stiff substrates. (A-B) Representative images from immunostainings with (Ai) Npn 1-ex and (Bi) Npn-int in permeabilised growth cones on 100 Pa and 1 kPa substrates. Scale bar is 10 µm, and applies to Ai and Bi. (Aii) A representative non-permeabilised growth cone stained for actin (phalloidin) and Npn1-ex. The top panel shows the growth cone under bright field illumination. Under these conditions, Npn1-ex does not stain anything, suggesting that it is unsuitable for ICC and that the signal observed in the permeabilised growth cones may be non-specific. Scale bar is 10 µm; growth cone is on a 100 Pa substrate. Lack of staining in the non-permeabilised condition was observed in three biological replicates. (Bii) Quantification of fluorescence intensity of Npn1-Int in growth cones cultured on soft and stiff substrates. No significant difference was observed in mean fluorescence intensities on soft and stiff substrates (p = 0.24, two sample t-test). Each point represents a single growth cone. Data from one biological replicate. Growth cone numbers (N) analysed for each condition are indicated above the boxplots (C) Western blot indicating that Npn1-ex recognizes the expected band size in protein lysates from Xenopus head tissue. This antibody is anticipated to recognize a band of 130 kD. Right two lines are from embryos injected with two different translation-blocking morpholinos against the mechanosensitive ion channel Piezo-1. Western blot courtesy of Katrin Mooslehner.

4.4 Cyclic GMP levels are elevated on soft substrates

Cyclic nucleotide levels are critical regulators of guidance cue responses. An elevation of the intracellular concentration of cGMP occurs immediately after growth cones are stimulated with Sema3A. This likely proceeds via the activity of the soluble guanylyl cyclase (sGC, also known as the nitric oxide sensitive guanylyl cyclase), though phosphodiesterase inhibition is also a possibility[48,80]. Moreover, pharmacological elevation of cGMP is sufficient to switch the growth cone response to Sema3A from repulsive to attractive[48,212]. *In vivo*, biological systems can tune cGMP levels to adjust the response of different cells, or even subcellular compartments, to Sema3A. For example, in mammalian cortical apical neurons Sema3A repels axons, but attracts dendrites, a difference that is due to higher levels of sGC in dendrites[80].

Quantitative immunocytochemistry (QICC) of growth cones on 100 Pa and 1 kPa substrates found that those on softer substrates had a consistently higher basal level of cGMP (Figure 4.3A,B). cGMP on the 100 Pa substrates also seemed to be clustered into more plentiful and more intense punctae, perhaps representing hotspots of cGMP production. It is not possible to knock out cGMP production in order to validate this staining, however, acute treatment of growth cones with an inhibitor of cGMP synthesis (ODQ, 1*H*-[1,2,4]Oxadiazolo[4,3-*a*]quinoxalin-1-one, a selective inhibitor of sGC[213]) significantly decreased the signal (Figure 4.3C).

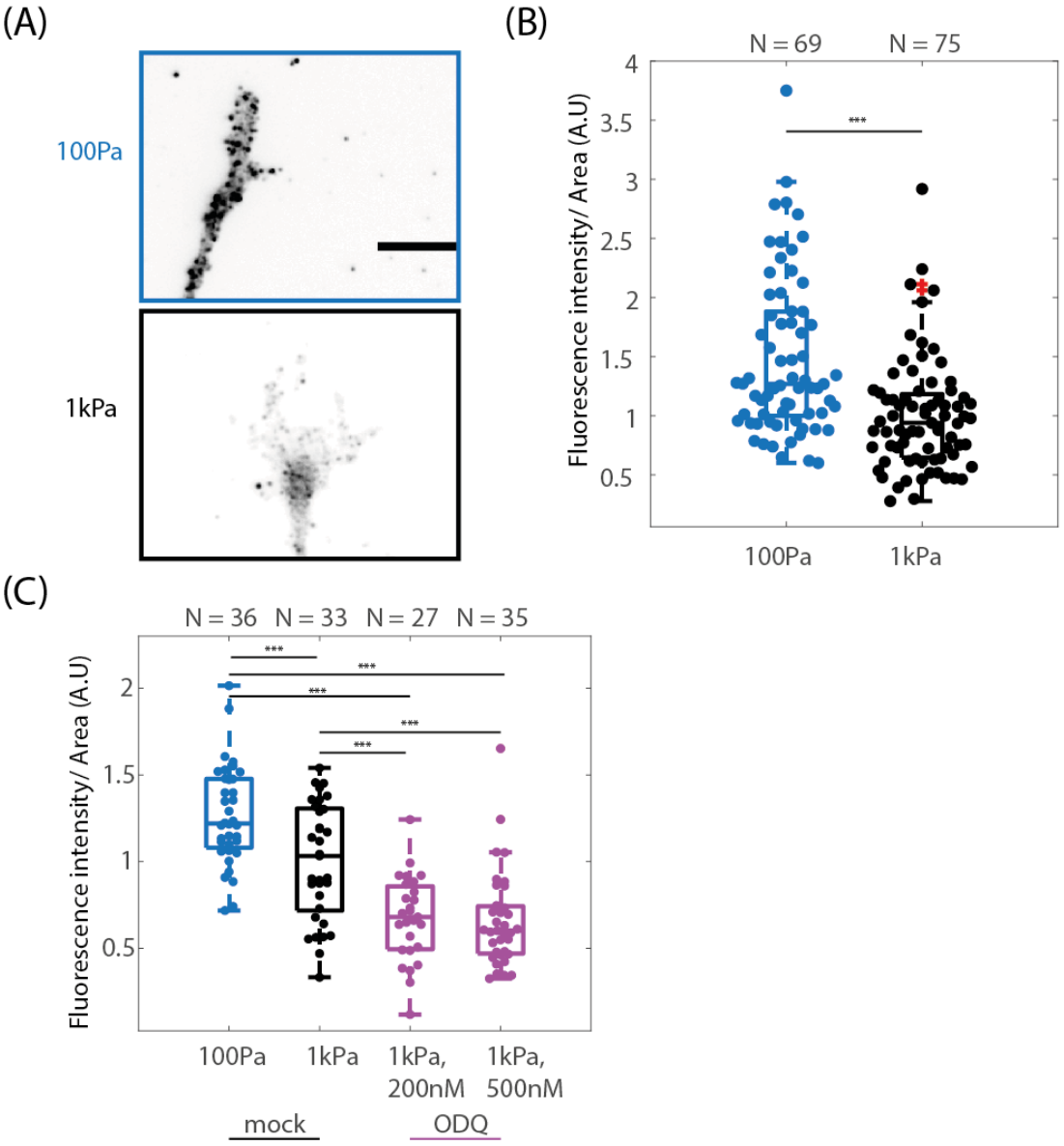

Figure 4.3: cGMP levels are higher in growth cones on soft substrates

Figure 4.3: (continued)

*QICC indicates that cGMP levels are elevated in growth cones on soft substrates. (A) Inverted fluorescence images of representative growth cones on soft (blue outline) and stiff (black outline) substrates. Both growth cones are displayed with the same LUT; scale is 10 µm (B) Quantification of fluorescence intensity. The number of growth cones analysed (N) is noted above each boxplot. Data come from three biological replicates. As the data for 100 Pa growth cones were not normally distributed the comparison was made with a Wilcoxon rank sum test, $p = 7.0e^{-07}$. (C) Growth cones treated with ODQ show a significant decrease in cGMP. ODQ was added 30 minutes prior to fixation, to mimic the conditions experienced by growth cones in the collapse assays described in the following section. Significance stars are indicated with the caveat that these data are from a single replicate. No significant difference was identified in cGMP levels between growth cones treated with 200 nM and 500 nM ODQ (p = 1). The number of growth cones analysed (N) is noted above each boxplot. Data were assessed with an ANOVA ($p =3.6e^{-16}$), followed by a Bonferroni post hoc test: $p_{100\text{-}1kPa} =7.4e^{-04}$, $p_{100pa\text{-}\ 1kPa\_200nMODQ} = 3.8e^{-09}$, $p_{100pa\text{-}1kpa\_500nMODQ} = 3.8e^{-09}$, $p_{1kpa\text{-}\ 1kPa\_200nMODQ} = 8.5e^{-05}$, $p_{1kpa\text{-}1kpa\_500nMODQ} = 8.6e^{-06}$. ***p< 0.001.*

4.5 Pharmacological modulation of cGMP differentially affects the collapse response on soft and stiff substrates

To further explore the role of cGMP in the substrate-stiffness sensitivity of the Sema3A response, I conducted collapse assays on 100 Pa and 1 kPa substrates in the presence of increasing levels of ODQ (decreasing cytosolic cGMP).

Excessively low levels of cGMP should prevent growth cones from collapsing in response to Sema3A: a cGMP elevation is necessary for the Sema3A response, and growth cones become insensitive when this is disallowed. In contrast, elevated levels of cGMP convert the turning response from repulsive to attractive. Under conditions of high intracellular cGMP we would therefore expect that growth cones should also not collapse in response to Sema3A, as Sema3A initiates a growth-promoting signal cascade under these conditions. Therefore, in response to a titration of cGMP levels the expected collapse response is parabolic[48] (Figure 4.4A).

On 1 kPa substrates, the proportion of growth cones collapsing after Sema3A treatment decreased as cGMP was reduced, the expected response for a population of growth cones with moderate levels of cytosolic cGMP in the unperturbed state, and similar to previously published literature with cells grown on glass substrates[84]. At 500nM ODQ, Sema3A application no longer had a significant effect on growth cones (Figure 4.4B).

In contrast, on 100 Pa substrates, the collapsed proportion did not change significantly with decreasing cGMP levels, though there was a trend towards slightly increased collapse in the ODQ treated populations, which may have been obscured by variation among the three replicates. Moreover, the difference in collapse proportion between growth cones on soft and stiff (Figure 3.1) disappeared at 200nM ODQ, and at 500nM

ODQ growth cones on soft substrates collapsed significantly more than those on stiff substrates (Figure 4.4B).

As previously mentioned, sGC, the guanylyl cyclase inhibited by ODQ, is likely the guanylyl cyclase involved in the obligate cGMP elevation downstream of Sema3A stimulation. Thus addition of ODQ both lowers basal cGMP and probably also reduces the Sema3A induced cGMP elevation.

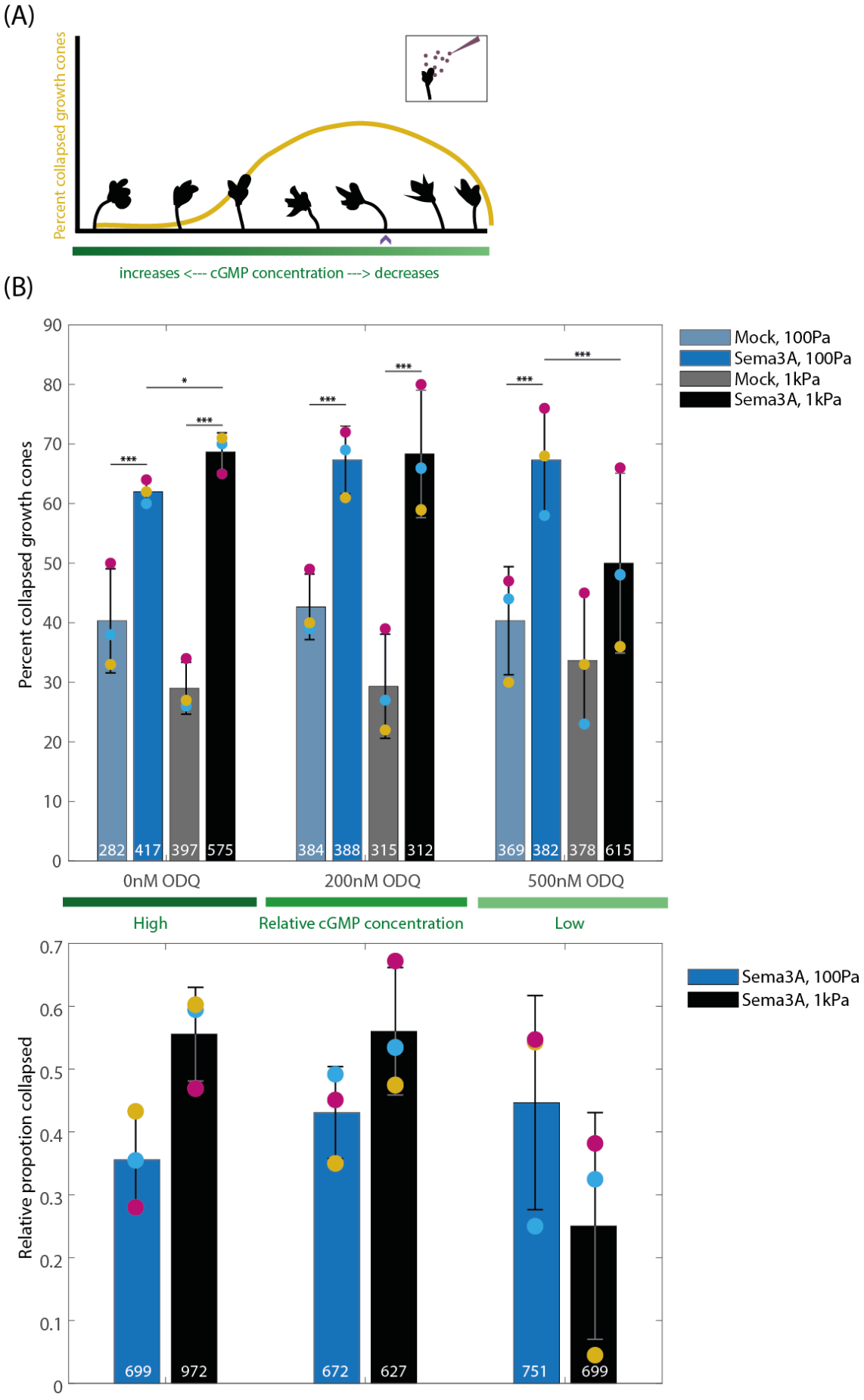
(A)
Percent collapsed growth cones
increases <--- cGMP concentration ---> decreases
(B)
Percent collapsed growth cones
Mock, 100Pa
Sema3A, 100Pa
Mock, 1kPa
Sema3A, 1kPa
282
417
397
575
384
388
315
312
369
382
378
615
0nM ODQ
200nM ODQ
500nM ODQ
High
Relative cGMP concentration
Low
Relative propotion collapsed
Sema3A, 100Pa
Sema3A, 1kPa
699
972
672
627
751
699

Figure 4.4: Growth cone collapse behaviour responds differently to cGMP modulation on 100 Pa and 1 kPa substrates

Reducing intracellular cGMP levels promotes collapse on 100 Pa substrates and inhibits it on 1 kPa substrates. (A) Cartoon of the expected Sema3A response as growth cone cGMP varies. Under 'standard' conditions (a glass substrate), Sema3A strongly repels growth cones (purple arrowhead, outlines indicate growth cone responses to asymmetric stimulation from the right as indicated in the inset). When cGMP is elevated, growth cones turn towards Sema3A, and when cGMP is reduced, the response diminishes in degree and is ultimately abrogated entirely. The collapse response (yellow line) should follow a parabolic distribution, with no collapse both when Sema3A functions as an attractive cue and when levels of cGMP are too low to permit growth cones to respond to Sema3A. Figure inspired by [48]. (B) Collapse assays on 100 Pa and 1 kPa substrates with 200nM or 500nM ODQ, which blocks production of cGMP. Bars indicate the mean of three biological replicates. Data are shown as raw proportions (top graph) and relative collapse proportion (bottom graph); the two plots share the x-axis labels in the middle. Proportions from each of the three replicates are scattered on the bars and colour-coded by replicate. Numbers on bars indicate the total number of growth cones counted for that condition, pooled from all three replicates. Increasing ODQ corresponds to reduced cGMP. P-values result from a Pearson Chi-Square test conducted on pooled growth cone numbers. For clarity, not all significance bars are included on the figure. A table containing all χ^2 statistics and p-values can be found in Appendix 4.2 (Table 9). For those values shown on the plot (subscripts indicate stiffness, ODQ condition, and Sema3A condition, in that order): $p_{soft\_ctrl\_ctl \rightarrow soft\_ctrl\_sema} = 2.6e^{-08}$; $p_{stiff\_ctrl\_ctl \rightarrow stiff\_ctrl\_sema} = 3.1e^{-31}$, $p_{soft\_200nM\_ctl \rightarrow soft\_200nM\_sema} = 3.0e^{-13}$; $p_{stiff\_200nM\_ctl \rightarrow stiff\_200nM\_sema} = 5.9e^{-23}$; $p_{soft\_500nM\_ctl \rightarrow soft\_500nM\_sema} = 2.5e^{-09}$; $p_{soft\_ctrl\_sema \rightarrow stiff\_ctrl\_sema} = 0.05$; $p_{soft\_500nM\_sema \rightarrow stiff\_500nM\_sema} = 1.3e^{-04}$. * p<0.05, ** p< 0.01, *** p< 0.001.

4.5.1 Simple model for substrate stiffness dependent regulation of Sema3A collapse

These results suggest that substrate stiffness may set the biochemical state of the growth cone by tuning the levels of key biological regulators such as cGMP. In this hypothesis, growth cones on soft and stiff substrates sit on different points of the response curve to Sema3A introduced in Figure 4.4A, and therefore their response to changing parameters is accordingly different. A simple visual representation of this hypothesis is shown in Figure 4.5. Growth cones on softer substrates begin with a higher level of cGMP. As cGMP is pharmacologically reduced in these growth cones, the collapse response to Sema3A increases. In contrast, growth cones on stiff substrates begin with a lower level of cGMP, a level of cGMP which induces approximately the maximum repulsive or collapsing response. As cGMP is decreased in these growth cones, the response to Sema3A is gradually reduced as the growth cones signalling capability is diminished.

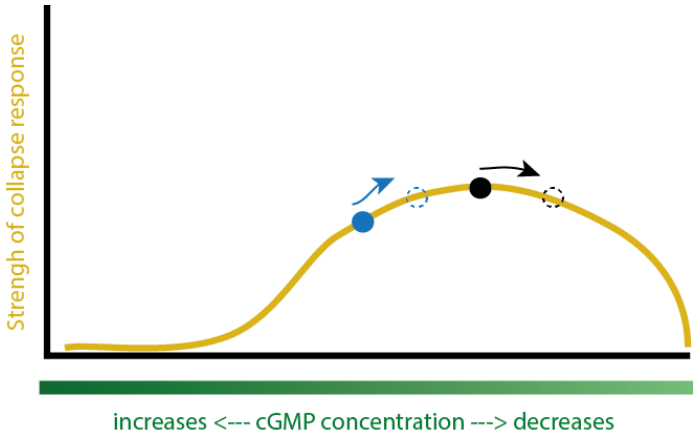

Figure 4.5: Simple model for substrate stiffness dependent regulation of Sema3A

Growth cones on soft substrates (blue dot) sit at a different point on the Sema3A state function than growth cones on stiff substrates (black dot). Thus as cGMP concentration decreases (arrows), growth cones on soft move toward the state of maximum responsivity to Sema3A, whereas growth cones on stiff substrates move towards a regime of lowered collapse response (new growth cone states shown as circles with dashed outlines).

4.6 Resting membrane potential is more depolarized on soft substrates

The membrane potential of active cells is highly regulated during development, maturation, and activity[214,215], and neurons typically hold a resting potential of -90 to -60mV across their membrane[216]. Fluctuations in membrane voltage are critically important for activity of mature neurons (in the form of action potentials). In the case of developing neurons, several chemical guidance cue responses have been shown to proceed via modulations in membrane potential, with repulsive responses inducing hyperpolarization and attractive responses depolarization[48,49]. This membrane potential change is required for neurons to respond to guidance cues; thus, for example, clamping neuronal membranes to their resting potential prevents cells from responding to Sema3A[48]. It is proposed that elevations of cGMP in response to Sema3A cause hyperpolarization via Cl^- channels. When cGMP reaches a critical level, Protein Kinase G (PKG) is activated, which activates Na^+ channels and leads to depolarization and attractive turning[48] (also see Figure 1.4).

I hypothesized that the difference in basal levels of cGMP observed between growth cones on soft and stiff substrates might result in changes in resting membrane potential of these neurons, further priming these growth cones to respond differently to Sema3A stimulation.

4.6.1 Electrophysiology

Patch clamp electrophysiology[217] is the gold standard for accurate recording of membrane potential. I first attempted to perform whole cell patch clamp recordings with the assistance of Hélène Gautier. As the cell bodies of *Xenopus* RGCs are inaccessible in my culture system due to their location inside the eye primordium explant, it was necessary to patch the axons themselves. This introduced a serious technical challenge: *Xenopus* RGC axons are <1 µm in diameter. This is on par with the aperture diameter of the narrower acceptable patch pipettes; smaller pipette diameters do not allow proper recording.

The success rate of clamping axons was thus extremely low; very often they were simply aspirated into the pipette or otherwise visibly damaged. Moreover, the quality of the recordings often degraded over time. This degradation was sometimes visible in the voltage trace as creeping, permanent depolarizations, which I took to indicate either a dying cell or a degrading seal (i.e. the cell was no longer properly clamped). At other times, I-V curves (a ramped voltage pulse intended to measure the activity of K^+ and Na^+ channels in the axons) showed significant deterioration after the voltage recording as compared to before it.

The few successful recordings suggested resting membrane potentials of around -59mV, a reasonable value for embryonic neurons. However, there were insufficient suitable recordings of this type (7 total) to identify differences in membrane potential on soft and stiff substrates. I therefore turned to optical voltage imaging.

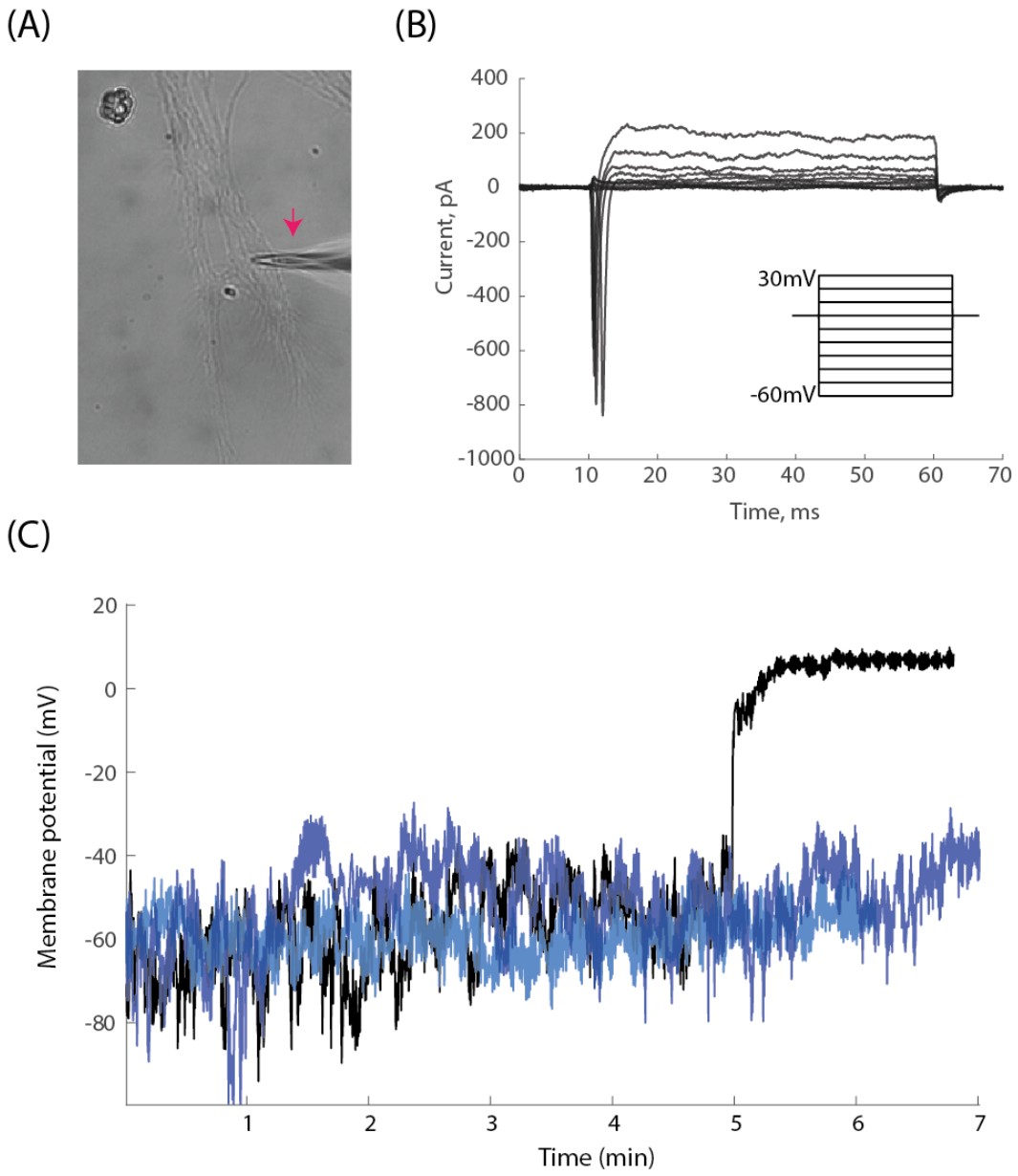

Figure 4.6: Pilot studies with single-cell patch clamp electrophysiology

Patch clamp recordings from Xenopus RGC axons. (A) Image showing a patch pipette (pink arrow) sealed to a Xenopus RGC in a bundle of RGCs. (B) Sample IV curve generated in whole cell voltage clamp mode by ramping up the voltage from -60 mV to 30 mV in steps of 10 mV (inset protocol). The trace demonstrates the robust presence of sodium and potassium channels to confirm the seal and the health of the patched neuron. (C) Resting membrane potential recordings of RGC axons continuously monitored in current clamp. Blue traces are from axons on 100 Pa gels, black trace from an axon on a 1 kPa gel. In the black trace, the seal is likely lost at the 5 minute mark.

4.6.2 Optical membrane potential imaging

Dyes for optical imaging of membrane potential lack the quantitative rigor of electrophysiology, but can provide excellent comparative data. I used a dye developed for a fluorometric imaging plate reader assay, which has previously been employed in

imaging experiments in neurons[218]. The dye is a lipophilic, anionic, bis-oxonol dye (referred to as membrane potential dye (MPD)). It enters cells preferentially when the membrane is more depolarized, and, upon entering the cell, its fluorescence increases due to contact with cytosolic proteins[219].

MPD gave an excellent fluorescence signal, which stabilised within ~15 minutes (Figure 4.7A,B). After at least 20 minutes of incubation with the dye, regions of axons on soft and stiff gels were imaged. For analysis, lines were drawn through filopodia and axons, and each intensity profile was fit with a Gaussian.

In both filopodia and axon shafts, the relative intensity was significantly higher on softer substrates, indicating a more depolarized resting membrane potential (Figure 4.7D).

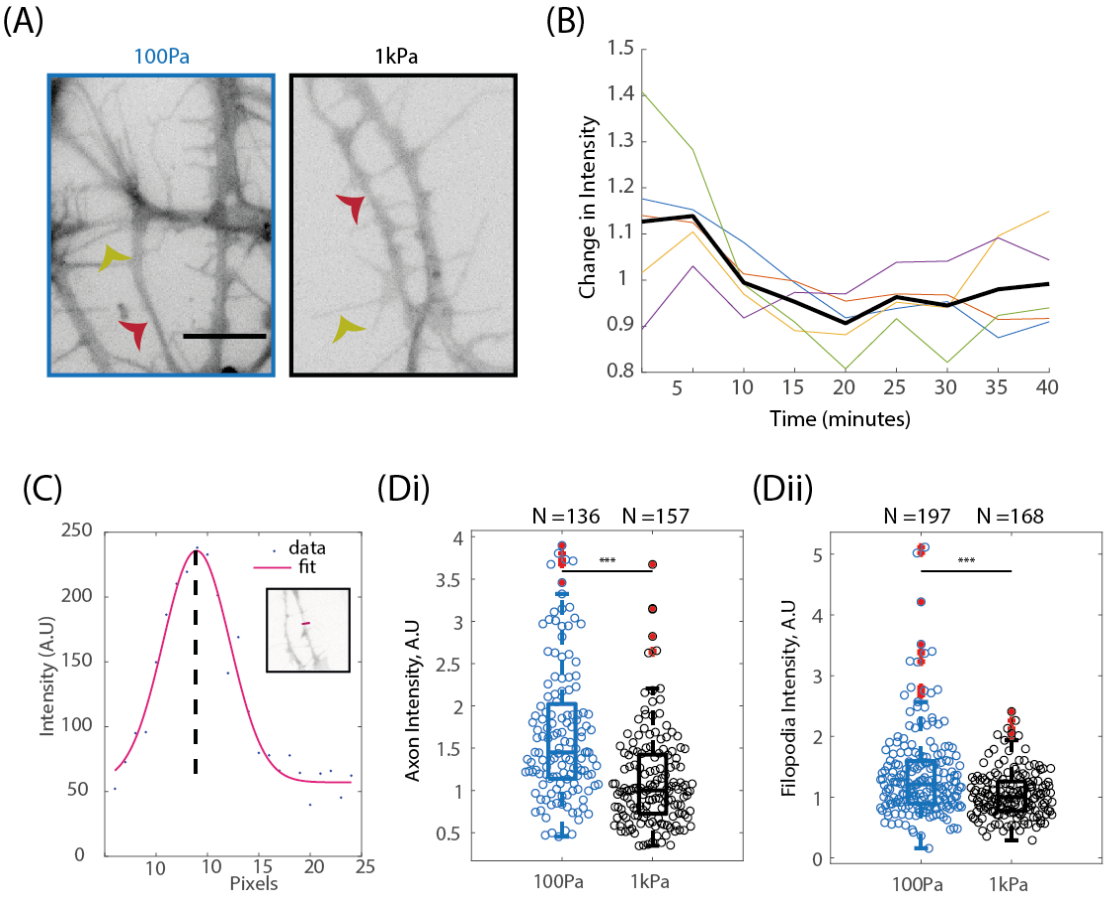

Figure 4.7: Resting membrane potential is more depolarized on soft substrates

Figure 4.7: (continued)

RGCs from cultures treated with MPD were imaged on soft and stiff substrates. (A) Sample images of regions on soft (left, blue outline) and stiff (right, black outline) substrates, imaged with MPD. Images are inverted fluorescence images such that darker colours indicate more depolarized membranes. Scale bar is 10 µm. For the analysis, I took line profiles across axon shafts (red arrowheads) and filopodia (yellow arrowheads) (B) Sample traces of fluorescence intensity over time, showing that intensity is largely stable after about 15 minutes under gentle imaging conditions that do not kill the cells. Coloured lines indicate traces from five different regions of interest that were imaged every five minutes over a 40 minute period. Values for each region were individually normalised to the mean intensity value for that ROI. The thick black line is the mean of the coloured lines. These data are from a single replicate. (C) Example Gaussian fit to an intensity profile from an axon (inset). Axons or filopodia were fit to $I = \alpha e^{\left(-\left(\frac{x-\beta}{\gamma}\right)^2\right)} + B$. *(Di),(Dii) Relative intensity at the peak of the Gaussian fit (α) are shown for axons (Di) and filopodia (Dii). In each case the values are relative to the median value on the 1 kPa substrate; this normalization was made separately for each replicate to control for variations in imaging conditions. For both axons and filopodia, intensity values on soft substrates were significantly higher (Di,* $p = 2.2e^{-11}$; *Dii,* $p = 3.9e^{-06}$*), indicating a more depolarized membrane. P-values results from a Wilcoxon rank sum test, as data were not normally distributed. Data come from three biological replicates, and the total number of axons or filopodia analysed (N) is indicated above each boxplot.*

4.7 Spontaneous calcium activity is increased on soft substrates

Most axon guidance cues, including Sema3A, provoke an influx of calcium into the growth cone, and localised increases in Ca^{2+} are sufficient to produce directional movement of growth cones[45,46,220]. As discussed in the preceding section, in the case of Sema3A, this calcium influx is thought to proceed downstream of cyclic nucleotide induced changes in membrane potential[48].

Growing neurons also exhibit a rich variety of spontaneous calcium transients, which are critical for cell fate decisions, growth, and pathfinding[221–224].

To examine calcium signalling in these cells, I injected *Xenopus* embryos with an mRNA encoding the calcium indicator, jRCaMP1b[225]. I imaged these neurons over long time scales (up to 80 minutes) with low temporal resolution (usually 0.2-0.4hz)—that is, a temporal resolution slow compared to the timescale of action potentials, but sufficient to capture the spontaneous calcium activity in embryonic neurons that typically occurs on the timescale of seconds[222].

These experiments revealed a wealth of complex calcium behaviours, which seemed particularly diverse on soft substrates. Spontaneous transients were of varying timescales and intensities. Some began in the growth cone and propagated in a retrograde manner towards the cell body (Figure 4.8B), while others began somewhere in the axon shaft and propagated bidirectionally towards both the soma and the growth cone (Figure 4.8A). Yet

others were spatially contained to just the growth cone or a single filopodium. This variety is consistent with previous observations of calcium transients in *Xenopus* neurons[226]. More frequently on soft substrates (observationally), an axon would make one or several strong calcium transients that proceeded cell death (Figure 4.8Cii, and Figure 4.9A). These events seemed distinct from general phototoxicity-induced cell death that could be observed at the end of long imaging periods or under harsher imaging conditions. Behaviours such as pruning or retraction of misprojecting or improperly synapsed axons are essential for proper neuronal development,[227] and these events could represent an *in vitro* equivalent of such behaviours.

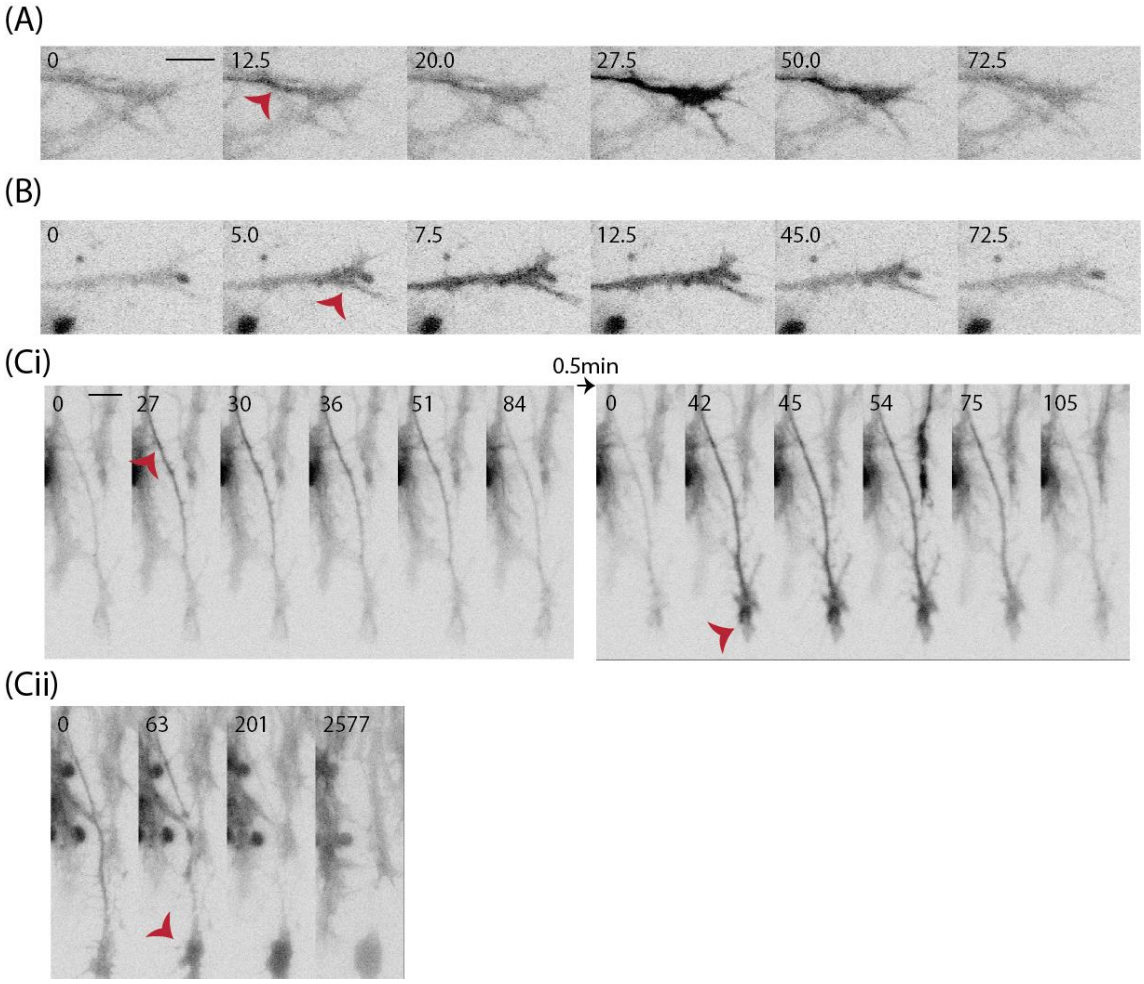

Figure 4.8: Diversity of spontaneous calcium activity in RGC neurons

Figure 4.8: (continued)

A variety of calcium transient types were observed, which operated on different timescales and in different spatial compartments (A-C) inverted fluorescence images of growth cones loaded with jRcAMP1b. (A) This transient began with a slight elevation in the axon hillock region (red arrowhead) which later became a strong global transient. Scale bar is 10 µm and applies also to B. (B) This transient began in the growth cone and propagated towards the soma. This was perhaps the most commonly observed transient type. (C) A series of interesting calcium behaviours in the same growth cone: (Ci) a transient which begins in the axon shaft and fails to propagate to the growth cone, followed soon by a larger transient which fills both growth cone and axon, and (Cii) about eight minutes later a 'terminal' calcium transient which ultimately results in cell death. Another dead cell is visible to its left, possibly indicative of accumulating photo-damage as this was near the end of the imaging period. The onset of each behaviour is indicated with a red arrow. Scale is 10 µm. (A-C) Time stamps are in seconds. Note that the time intervals are not equal, but rather intended to most clearly show the transients. These examples are all from neurons on 100 Pa substrates.

I manually counted calcium transients on 100 Pa and 1 kPa substrates. As it is difficult to properly discern the total number of axons in the dense axon outgrowth of eye primordia cultures, the proportion that make transients cannot be easily calculated. I therefore analysed 'active' axons that made at least one transient during the imaging period and counted the total number of transients made by each active axon. This analysis did not discriminate between transients that propagated long and short distances. (The imaging was generally not of high enough spatiotemporal resolution to discern transients that were restricted to filopodia only and therefore these were excluded. Transients had to fill at least the growth cone to be counted.) Consistent with what can be seen simply by eye (Figure 4.9Ai), active axons made more spontaneous calcium transients on soft substrates (Figure 4.9Aii).

By eye, transients on soft substrates also often appeared more intense, though ratiometric imaging would be required to properly quantify this effect. It is also possible, for example, that axons on soft substrates more enthusiastically translate the calcium indicator.

Prolonged imaging can be damaging to cells, and my imaging periods were quite long, generally at least an hour. I observed that, under gentle illumination conditions, the number of transients appeared to decrease gradually throughout imaging. If imaging conditions were made more aggressive (i.e. more intense illumination, or using a green calcium indicator), the transient number instead increased dramatically, concordant with an increase in global intracellular calcium levels, and the neurites quickly assumed a blebbed morphology and died.

To determine the influence of prolonged imaging on transient frequency in my cultures, I quantified transient numbers in the first and final 15 minutes of a 90 minute period

without imaging in the interim time. I compared these data to transient numbers in the first and final 15 minutes of axons that were imaged throughout a 90 minute period without break. Axon populations that had been 'rested' during the interim displayed the same frequency of transients in both periods, whereas axons that had been imaged throughout displayed a significant decrease in transient number (Figure 4.9B). It should therefore be noted that the results in Figure 4.9A come from an analysis over an imaging period of one hour, over which time some damage will likely have been accrued by the axons.

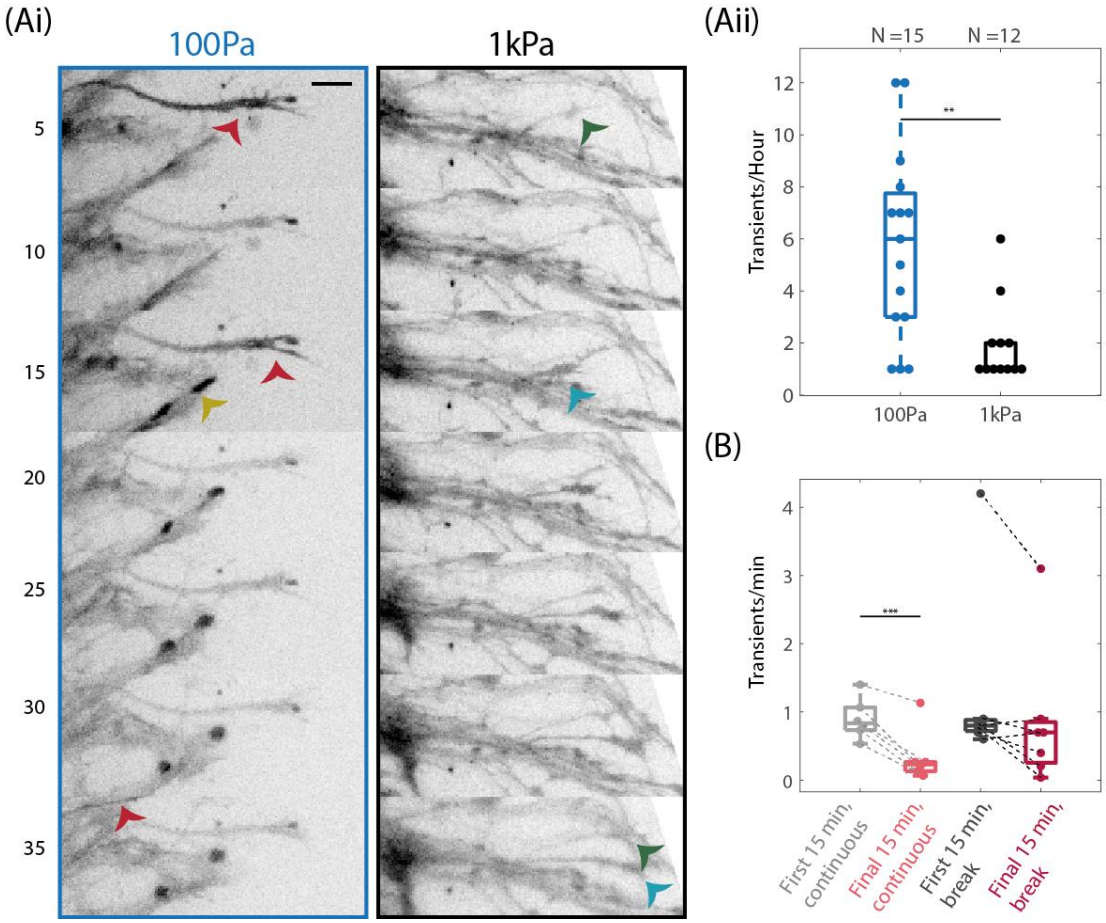

Figure 4.9: Growth cones on soft substrates make more frequent spontaneous calcium transients

Figure 4.9: (continued)

*Growth cones expressing jRcAMP1b were imaged on soft and stiff substrates. (Ai) Inverted fluorescence images showing characteristic behaviour of growth cones on 100 Pa and 1 kPa substrates. Growth cones on 100 Pa substrates (left, blue outline) make frequent transients. Transients are indicated by red arrows. The yellow arrow indicates a growth cone that fills up with calcium and then dies; by the final frame is has become two blebs. On stiff substrates (right, black outline) growth cones grow in a more directed, rapid manner, and make fewer transients. The initial and final positions of two rapidly growing growth cones indicated by the blue and green arrowheads. Frames are separated by 5 minutes each (timestamps to left), and the scale bar (applicable to all images) is 10 µm. (Aii) Transients counted per hour in axons that exhibited at least one transient. Each dot represents an individual axon. Axons made significantly more frequent transients on soft substrates (p = 0.0024, two sample t-test). The number of axons analysed (N) is indicated above the boxplot. These axons were derived from a total of five and seven movies on 1 kPa and 100 Pa substrates, respectively, which were acquired across three separate days of experiments. (B) Long imaging periods result in a decrease in transient frequency. The frequency of transients counted in the first and final 15 minutes in growth cone populations that were either imaged at a frame rate of 0.3 or 0.4 for 90 minutes ('continuous') or imaged for two 15 minute periods with a one hours break between the two imaging periods ('break'). Dashed lines connect the first and final fifteen minute measurements for the same regions. Transient numbers in the first and final 15 minutes of 'continuous' movies were significantly different (p = 6.0e^{-04}, paired sample t-test), and this difference was not present in the 'break' condition (p = 0.06, paired sample t-test). For this experiment all cultures were on 100 Pa substrates. Five movies were analysed in the 'continuous' condition, and seven in the 'break' condition, from data for each condition were collected across three separate days of experiments; however data for 'break' and 'continuous' condition were not collected on the same days. **p<0.01, *** p<0.001.*

4.7.1 Two-day old cultures on stiff substrates do not exhibit an increase in transient frequency.

Substrate stiffness can influence cell maturation and differentiation, and neurons mature faster on softer substrates (Eva Kreysing, personal communication). To see if neurons on 1 kPa substrates begin to exhibit more frequent transients if they were given longer to grow, I kept cultures on 1 kPa substrates and conducted calcium imaging after 20 hours (my usual imaging period was ~18-24 hours after plating), and again after ~44 hours. After 44 hours, these cultures had very few robust transients; small 'flickers' were sometimes observed. Although is possible that development *in vitro* does entirely recapitulate the expected developmental time course of neurons, these experiments suggested that the observed difference in calcium transient frequencies is a function of neuronal mechanosensing rather than maturity.

4.8 Chapter conclusions and outlook

My data show that RGCs cultured on softer substrates contain elevated levels of growth cone intracellular cGMP, more depolarized membranes, and an increased frequency of spontaneous calcium transients. Based on what is known about the Sema3A signalling

cascade, all of these findings are consistent with each other[48]: elevated intracellular cGMP leads to a more depolarized membrane which creates a more permissive environment for the activation of voltage gated calcium channels. This in turn may lead both to the higher levels of spontaneous calcium transients observed on soft substrates, and to a reduction in the degree of repulsion induced by Sema3A response

CGMP, calcium, and membrane potential all seem to be homeostatic parameters, the levels of which are subject to tight regulation. Thus by adjusting these parameters, changes in substrate stiffness set the growth cone/axon in a different biochemical state, priming them to respond differently to chemical guidance cues and likely other biochemical stimuli as well.

4.8.1 Calcium and growth cone morphology

The increased calcium transients observed here may have an important connection to the characteristic neurite morphologies observed on soft and stiff substrates[123]. *In vivo* and *in vitro,* growth cones that make more frequent calcium transients grow less directly, exhibiting more frequent stalling and retraction[223,224]. Indeed it has been proposed that at 'decision points' in their growth trajectory, such as when they encounter the optic chiasm, growth cones slow down[32] concordant with an increase in calcium activity[224]. On soft substrates, *Xenopus* RGCs exhibit less directed growth and fasciculate less[123] (Figure 1.8).

Interestingly, increased calcium transients are generally associated with an expansion in growth cone size and complexity[228,229]. I observe that growth cones on 1 kPa substrates are larger than those on 100 Pa substrates; however, it is difficult to extrapolate that result to the *in vivo* situation with any degree of clarity*:* growth cones in a 3D environment may behave very differently. Moreover, spatially restricted filopodial calcium transients may be more important for regulating growth cone morphology than the larger transients examined here.

Ultimately, these results show that substrates stiffness profoundly alters calcium dynamics in RGC growth cones. A more precise understanding would require an in-depth analysis to disentangle different types of calcium transients and elucidate signalling micro domains associated with the stiffness-regulated calcium behaviours.

4.8.2 Outlook

These mechanics-dependent shifts in cGMP levels, membrane potential, and calcium signalling strongly suggest that substrate stiffness modulates the Sema3A response by influencing these well characterized regulators of the Sema3A signalling cascade. I next asked what signalling pathways were responsible for inducing these substrate-stiffness dependent biochemical changes, and I explored first the possibility of a role for mechanosensitive ion channel activity.

5 THE ROLE OF PIEZO1 IN THE MECHANICAL REGULATION OF AXON GUIDANCE

5.1 Introduction

Knockdown (KD) of the mechanosensitive ion channel Piezo1 results in severe pathfinding defects in the *Xenopus* retinotectal system, indicating that it may participate in the mechanical regulation of axon guidance (Section 1.4 and Reference [123]). We previously exploited the MSC blocker GsMTx-4[230,231], which, similar to Piezo1 KD, confounded RGC growth *in vivo. In vitro,* GsMTx-4 induced significant growth reduction of RGC axons*;* GsMTx-4 treatment on stiff substrates resulted in a phenotype similar to that of axons growing on soft substrates. These results led us to speculate that Piezo1 was more active on stiff substrates and played an instructive role in the regulation of outgrowth in these cells[123].

GsMTx-4 is not specific against Piezo1—it blocks multiple classes of mechanosensitive ion channels, and is thought to influence channel gating by altering the local lipid environment[232]. In order to gain a clearer idea of the role of Piezo1 in growth and guidance regulation in RGC axons, I used two different approaches: injection or electroporation of a translation blocking morpholino against Piezo1, or treatment with a recently discovered, specific pharmacological agonist of Piezo1, Yoda1[161,176], to alter Piezo1 signaling in *in vitro* RGC cultures.

5.2 Morphological effects of Piezo1 manipulation

5.2.1 Influence of Piezo1 knockdown on axon morphology

We previously employed a Piezo1 morpholino[123] to study the influence of Piezo1 knockdown on axon growth and pathfinding. This morpholino was based on the sequence

of *X. tropocalis piezo1*; with the publication of a more thoroughly annotated genome for *X. laevis*[233] my colleague Eva Pillai redesigned our morpholino to remove two mismatches in order to increase specificity and to reduce the possibility of off-target effects (this new morpholino will be referred to as MO-pz1.l and the old as MO-pz1.t, distinguishing those designed against the *X. laevis* and *X. tropicalis* sequences).

Western blots for Piezo1 using head tissue from embryos injected with either MO-pz1.l or MO-pz1.t demonstrated a knockdown of 48% ± 17% or 22% ± 16% respectively, compared to tissue injected with a control morpholino (standard scrambled control, MO-scr) (Figure 5.1A).

Embryos with Piezo1 knocked down exhibit a variety of characteristic morphological defects, among which, unfortunately, are underdeveloped and poorly pigmented eyes. Interestingly, the retinal pigmented epithelia (RPE) often adheres poorly to the underlying tissue in these embryos, resulting in a fluid filled cavity between the RPE and the eye, and possibly indicating severe adhesion defects. Together, however, these factors makes culturing of eye primordia difficult, and those which do grow often extend very few axons, which makes morphological analysis difficult.

To circumvent these technical issues, which seemed to be particularly severe for embryos injected with MO-pz1.t, I used targeted electroporation[187] at a later developmental stage (~28) to introduce morpholinos together with a rhodamine or fluorescein-tagged dextran (to more clearly visualize transfected cells) into RGCs. I then dissected and cultured explants a few days later at stage 35/36.

Examples of explants from electroporated embryos grown on glass are shown in Figure 5.1B and C. In general, axons which displayed strong fluorescence from MO-pz1.t or MO-pz1.l did not appear visibly different than axons containing MO-scr. Several factors might contribute to this observation. First, with electroporation it is impossible to control the exact amount of MO in any particular axon. Therefore, it is hard to have a sense of the severity of knockdown in any particular neurite. This is also true of MO injection; however, at least in that case one is able to allay this concern by averaging over a large population. Secondly, as compared to injection, the perturbation is introduced much later, possibly after a significant amount of Piezo1 has been synthesized (to my knowledge data is not available on protein turnover rates of Piezo1). Finally, these KD axons are growing among a much larger population of wild-type axons. Cell-cell adhesion is very important

for the growth of theses axons[234,235], and some of the growth phenotypes may be emergent effects that can only be observed in larger populations of knockdown axons.

Therefore it seemed important to be able to grow cultures with more homogeneously knocked-down Piezo-1. Fortunately, explants injected with the new morpholino, MO-pz1.l, grew better in culture compared to the previous experiments with MO-pz1.t, even though on average this morpholino seemed to knock down Piezo1 to a greater extent (Figure 5.1Aii). I was therefore able to acquire sufficient images to complete a morphological analysis of explants in which we expect that the vast majority of the neurites contain the MO.

To make quantitative comparisons of the extent of neurite outgrowth, I performed a Sholl analysis as previously[123,191]. Briefly, in this analysis concentric circles are drawn every 5 µm, using the perimeter of the explant as the starting radius (Figure 5.2B). The number of times each circle crosses an axon or bundle of axons is counted, resulting in profiles as in Figure 5.2C.

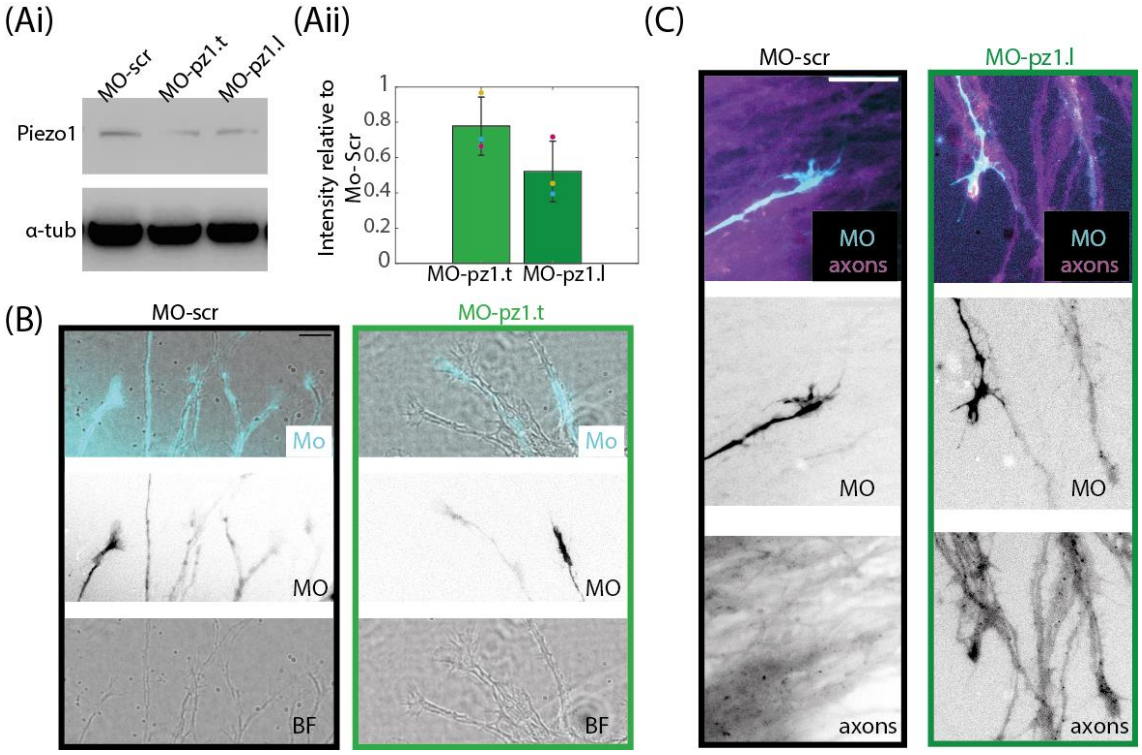

Figure 5.1: Validation of Piezo1 knockdown, and neurite morphology of MO electroporated embryos

Figure 5.1: (continued)

Piezo1 morpholino injection reduces Piezo-1 levels in Xenopus head tissue, but does not seem to alter morphology of sparsely transfected axons (Ai) representative western blot of Xenopus head tissue from embryos injected with 15 ng/BM MO-scr, MO-pz1.t, and MO-pz1.L. Piezo1 was detected using a polyclonal antibody (NBP1-78446, Novus Biological, 1:500). (Aii) Quantification of morpholino knockdowns from three western blots, in each case intensity values were normalized to α-tubulin levels (ab7291, Abcam, 1:10000). Intensity values from the MO-scr lane were set to one. Bar heights show the mean of three replicates, dots represent individual values from each of the three replicates, colour-coded by replicate. In each case, lysates were loaded in duplicate or triplicate, and each dot thus represents the average of 2 or 3 lanes. MO-pz1.l induced a significant knockdown ($p = 6.9e^{-04}$, one sample t-test on pooled relative intensity values from all blots, 8 total measurements). MO-pz1.t induced a less severe effect which did not reach the threshold of significant (p = 0.08, one sample t-test on pooled relative intensity values from all plots, 8 total measurements), Western blots were completed by Eva Pillai and Katrin Mooslehner, and quantification of signal intensity was performed by Katrin Mooslehner. (B-C) Images of axons from embryos electroporated with MO-pz1.L and MO-pz1.t. Electroporation results in a random subset of axons labelled. As fluorescence from the morpholinos was very weak, the signal from the co-electroporated fluorescent dextran is shown. (B) RGC axons from embryos electroporated with MO-scr or MO-pz1.t, and co-electroporated with TMR-dextran. Variation in the degree of uptake by individual axons is clearly visible. Scale bar is 20 μm. (C) RGC axons from embryos electroporated with MO-scr or MO-pz1.l. In this case embryos were injected at the four cell stage with TMR-dextran to label all cells and later electroporated with MO-pz1.l and FITC-dextran. Scale bar is 20 μm.

Preliminary experiments were conducted on glass substrates; here, I observed a striking morphological difference; explants from embryos injected with MO-pz1.l had significantly longer outgrowth than those from MO-scr embryos (Figure 5.2).

Next I completed the same experiments on 100 Pa and 1 kPa substrates. Surprisingly, in contrast to explants on glass, explants on hydrogels substrates did not seem to exhibit a strong growth response to Piezo1 knockdown; I did not observe any significant differences in outgrowth between MO-scr and MO-pz1.l injected explants on gels (Figure 5.3). However, the total number of explants analysed in this experiment was quite low, and additional replicates will be important to clarify this result.

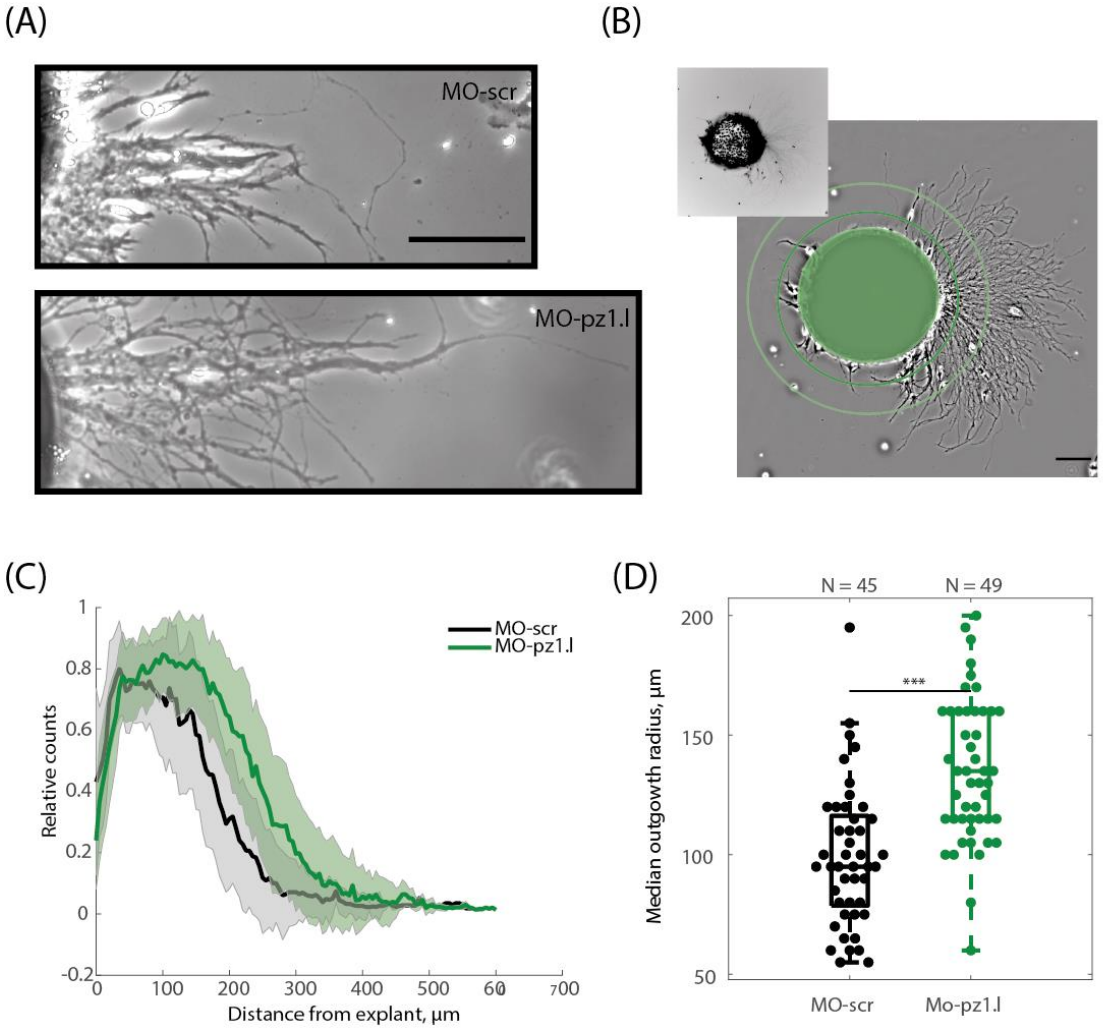

Figure 5.2: Piezo1 knockdown promotes RGC outgrowth on glass substrates

*On glass, axons from MO-pz1.l injected explants exhibited higher rates of outgrowth than those from MO-scr injected explants. (A) Images of representative explants from MO-scr and MO-pz1.l injected embryos; Scale is 100 µm. (B) A MO-pz1.l explant is shown to demonstrate the principle of Sholl analysis: concentric circles are drawn emanating from the outer radius of the explant, and the number of axons/axon bundles that each circle crosses is counted. The explant has been filtered through a Fourier bandpass filter to accentuate axons and eliminate fluctuations in background intensity. Inset: morpholino fluorescence is still visible, though very faint, in the axons under these imaging conditions. Scale bar is 100 µm. (C) Outgrowth profiles from explants on soft and stiff substrates. The line represents the median number of axons/axon bundles crossed at each radius where R= 0 is the outer radius of the explant (i.e. solid green circle in B). The profile for each explant was first individually normalized by dividing by the number of counts at the radius with the greatest number of counts for that explant. Shaded regions represent standard deviations. (D) Median radii of outgrowth (the median radius from the explant at which a circle crosses an axon/axon bundle) for explants on soft and stiff substrates. Each dot represents the median outgrowth radius for a single explant. The total number of explants analysed in each condition (N) is indicated above each boxplot. Data come from four biological replicates. ***p = 5.2e^{-08}, two sample t-test.*

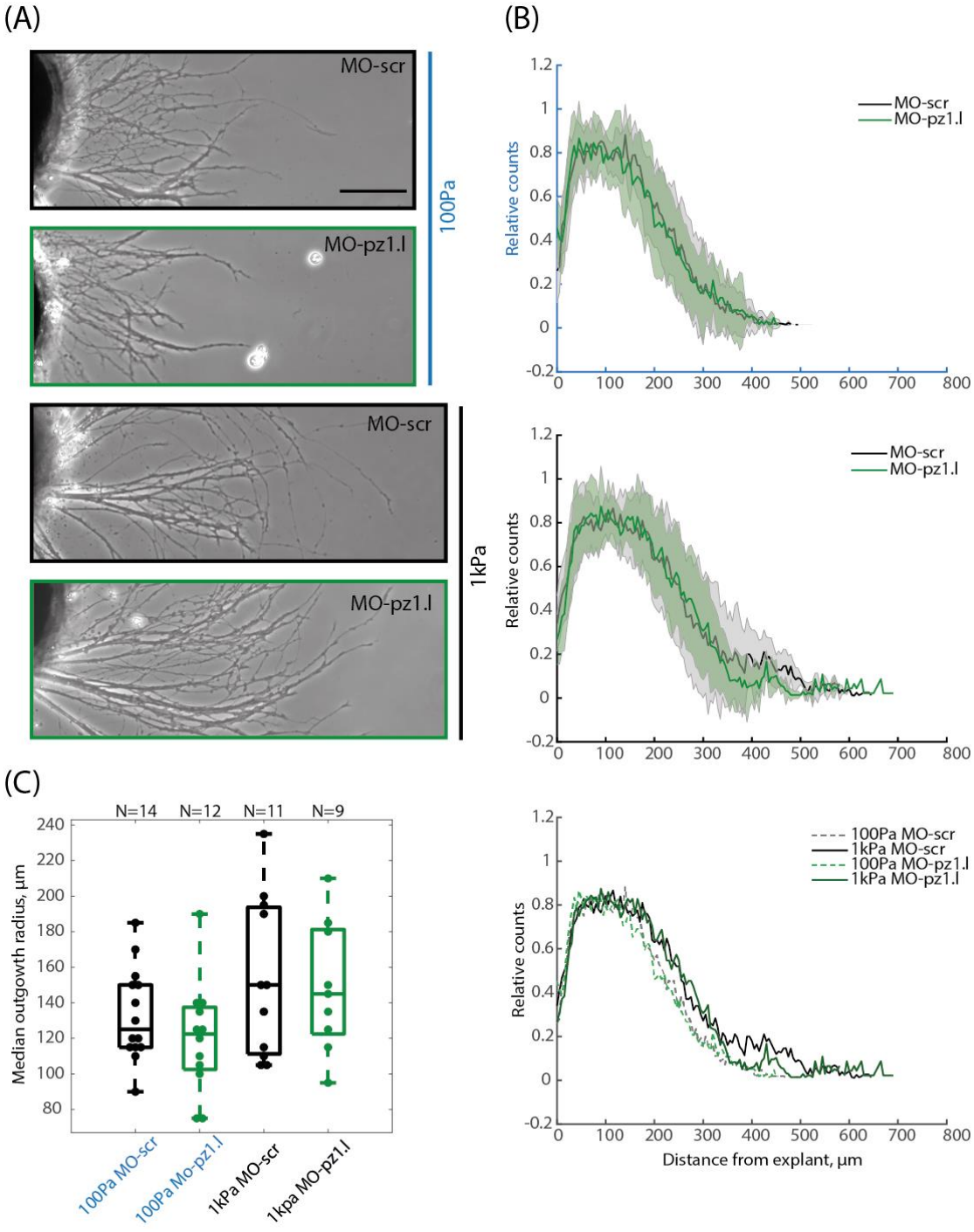

Figure 5.3: Piezo1 knockdown does not significantly alter RGC outgrowth on 100 Pa and 1 kPa gels

Figure 5.3: (continued)

Unlike on glass, explants from embryos injected with MO-pz1.l did not demonstrate increased axon outgrowth compared to those from MO-scr injected embryos when grown on 1 kPa or 100 Pa substrates. (A) Sample images of axons on 100 Pa (blue line) or 1 kPa (black line) substrates from MO-scr (black outlines) and MO-pz1.l (green outlines) injected embryos. Scale bar is 100 µm (B) Traces showing sholl profiles of explants; as described in the caption to Figure 5.2, the line represents normalized medians, and shaded regions show standard deviations. The top two plots show M0-scr and MO-pz1 conditions separately for 100 Pa and 1 kPa substrates, the bottom plot shows all conditions on the same plot, with error bars removed for clarity. (C) Median outgrowth radii of explants on 1 kPa and 100 Pa substrates. An ANOVA identified no significant differences between groups (p = 0.1). In this case, the difference between outgrowth on 1 kPa and 100 Pa substrates was not significant overall. This is possibly due to low explant numbers due to adhesion difficulties. The numbers of explants analysed in each condition (N) is noted above each boxplot. Data came from three biological replicates, but due to the aforementioned adhesion difficulties, in some of the conditions explants rom only two replicates could be analysed.

5.2.2 Chronic Yoda1 treatment induces a reduction in RGC outgrowth

Our previous work using the MSC blocking drug GsMTx-4, which inhibits RGC outgrowth (Figure 1.8), together with the confounding effect of Piezo1 KD on axon pathfinding[123] strongly suggested an important role for this MSC in regulating RGC outgrowth. Thus I wanted to further explore the role of Piezo1 in RGC mechanosensitivity and the Sema3A response. I therefore used the recently discovered Piezo1 agonist Yoda1[176]. Yoda1 is a small molecule thought to bind to the Piezo1 protein, increasing the opening probability of the channel and slowing inactivation kinetics[161]. It has proven very useful for studying the signalling modalities[236] and biophysical properties of the channel[178], though its exact mechanism of action has yet to be elucidated.

On glass substrates, explants incubated overnight in the presence of Yoda1 exhibited reduced outgrowth, apparently consistent with the increased outgrowth observed upon Piezo-1 inhibition. A concentration titration found that this effect increases proportionally to the concentration of Yoda1 added to the culture (Figure 5.4). At intermediate concentrations of Yoda1, axons were visibly normal except for the reduction in outgrowth. At the highest concentration of Yoda1 (2.5 µg/mL); however, axons began to display signs of distress, including varicosities along their length, a hallmark of ultrastructural damage in neurons that is observed under a range of disease and stress conditions *in vitro* and *in vivo* [237–240].

I observed the same growth effect on 100 Pa and 1 kPa substrates: incubation with 2.5 µg/mL Yoda1 resulted in a strong reduction in outgrowth (Figure 5.5). As with the

2.5 µg/mL treated cultures on glass, these explants were visibly pathological, with axons displaying frequent varicosities (Figure 5.5A).

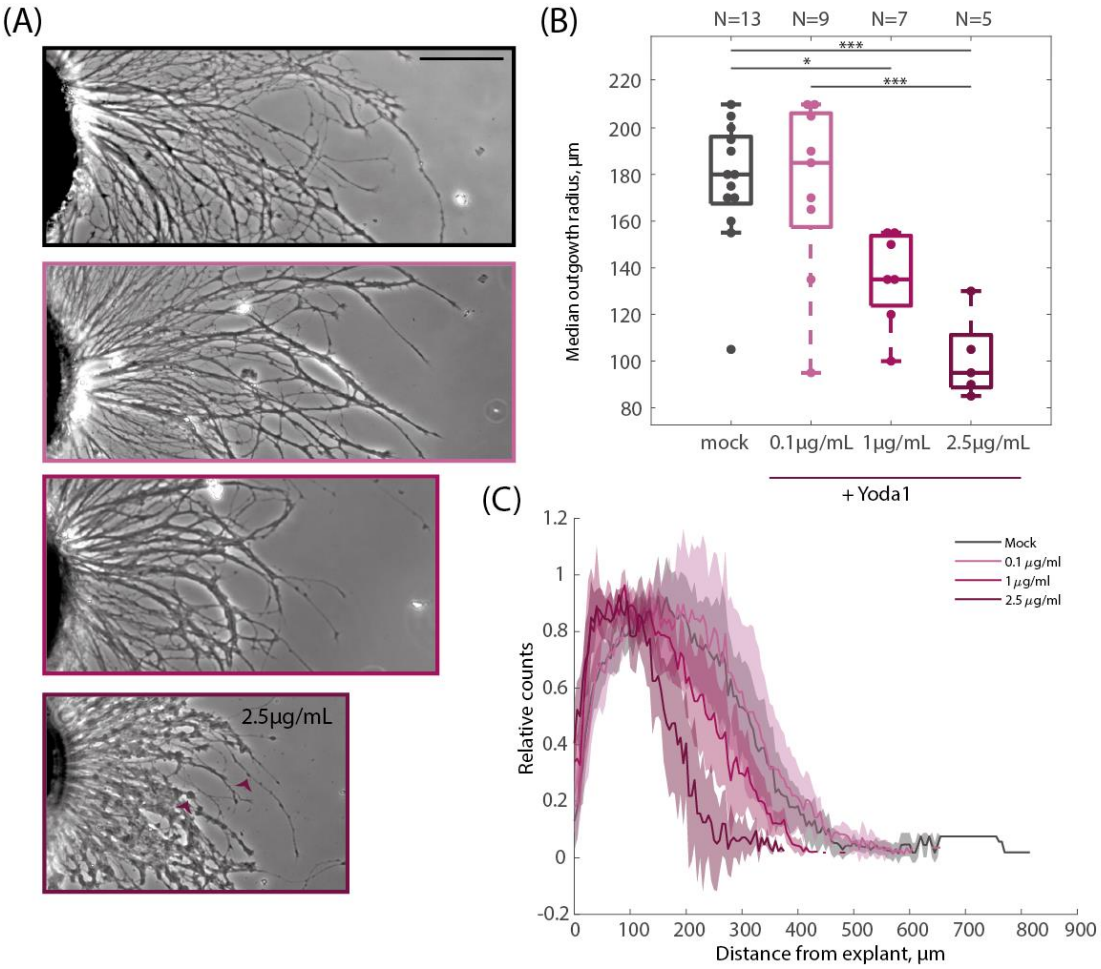

Figure 5.4: Chronic treatment with Yoda1 reduces axon outgrowth on glass

*Explants incubated overnight with increasing concentrations of Yoda1 display reduced outgrowth. (A) Regions of axons taken from representative explants for each condition. Scale bar is 100 µm. At 2.5 µg/mL Yoda1, near the upper limit of possible concentrations due to the relative insolubility of Yoda1 in aqueous solution, explants are visibly enfeebled, by eye demonstrating an increase in varicosities along their length (examples shown with arrowheads). Explants were analysed with Sholl analysis. (B) Median outgrowth radii and (C) Sholl profiles, displayed as previously described with the line indicating the median and shaded region the standard deviation, indicate that increasing Yoda1 concentration seems to reduce axon outgrowth. Note also that approximately the same number of explants were plated in each case, but the number which adhered to the substrate and produced axons decreased with increasing Yoda1 concentration. The number of explants analysed in each condition (N) is stated above the boxplot in (B). These data are from a single experiment. Data were assessed with an ANOVA ($p = 5.8e^{-05}$) followed by a Bonferroni post-hoc test: $p_{mock \rightarrow 1\mu g/mL} = 0.023$, $p_{mock \rightarrow 2.5\ \mu g/mL} = 1.2e^{-04}$, $p_{2.5\mu g/mL \rightarrow 0.1\mu g/mL} = 4.3e^{-04}$. Differences between 1 µg/mL and 0.1 µg/mL populations, and between the 1 µg/mL and 2.5 µg/mL populations did not reach significant ($p_{1\mu g/mL \rightarrow 0.1\mu g/mL} = 0.058$, $p_{1\mu g/mL \rightarrow 2.1\mu g/mL} = 0.18$). *p< 0.05, **p<0.01, ***p<0.001*

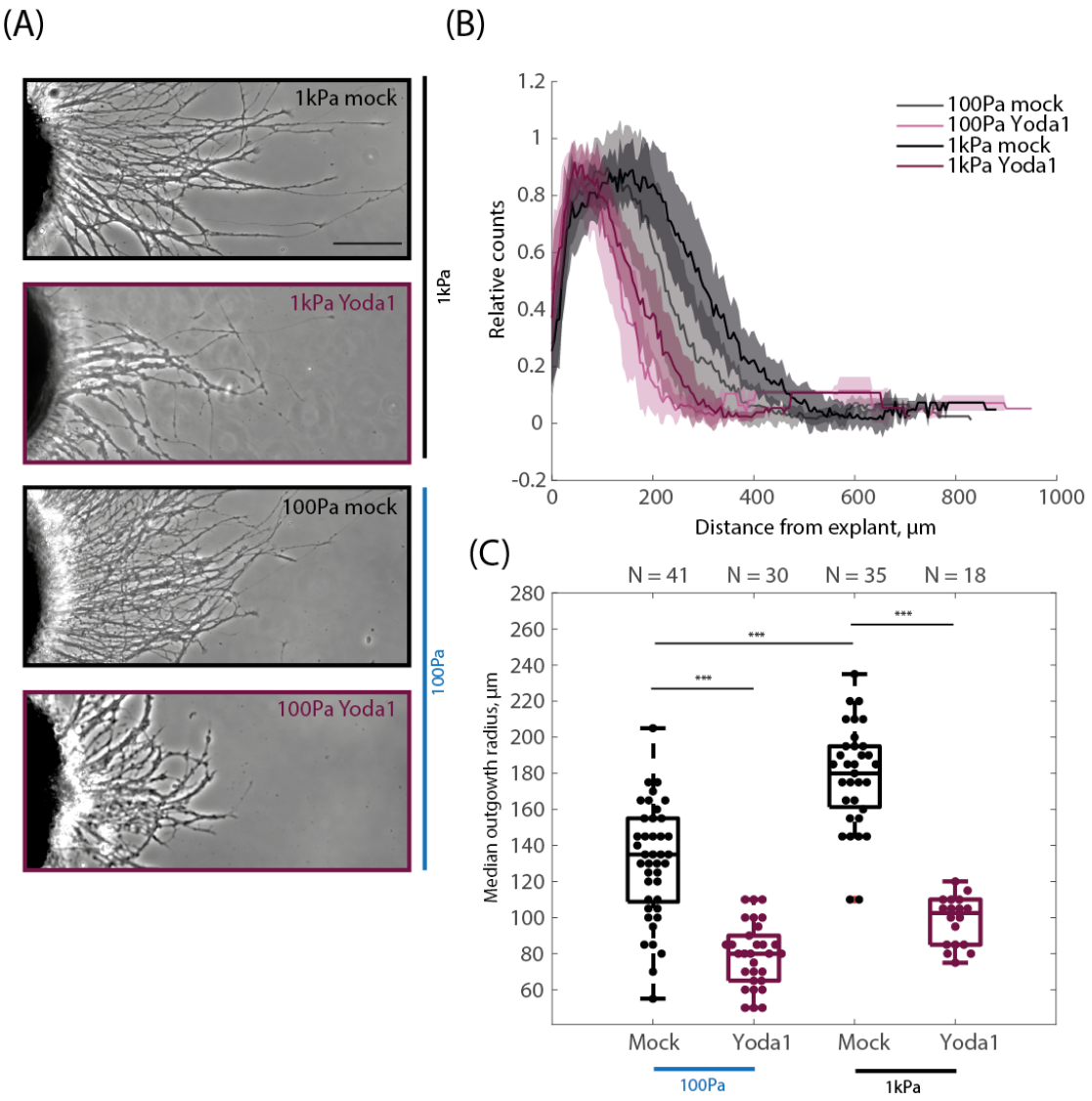

Figure 5.5: Chronic treatment with Yoda1 reduces outgrowth on 100 Pa and 1 kPa substrates

*Treatment with 2.5 µg/mL Yoda1 overnight significantly reduced RGC axon outgrowth from explants grown on both 100 and 1 kPa substrates. (A) Sample images of axons on soft (blue line) and stiff (black line) substrates treated over night with Yoda1 (magenta outlines) or a mock treatment (black outlines). Scale bar is 100 µm. Explants were analysed with Sholl analysis. (B) Sholl profiles, displayed as previously described with the line indicating the median and shaded region the standard deviation, and (C) median outgrowth radii, indicate that outgrowth is reduced in the Yoda1 treated condition on both 100 Pa and 1 kPa substrates. Data are from three biological replicates. The number of explants analysed in each condition (N) is shown above the boxplots in C. Data were assessed using an ANOVA ($p = 3.3e^{-30}$) followed by a Bonferroni post hoc test. For clarity, not all significance bars are shown on the plot. For those values shown: $p_{soft\_mock \rightarrow stiff\_mock} = 3.7e^{-09}$, $p_{soft\_mock \rightarrow soft\_yoda1} = 3.8e^{-09}$, $p_{stiff\_mock \rightarrow stiff\_yoda1} = 3.8e^{-09}$. In addition, $p_{soft\_yoda1 \rightarrow stiff\_yoda1} = 0.072$, $p_{stiff\_mock \rightarrow soft\_yoda1} = 3.8e^{-09}$, $p_{soft\_mock \rightarrow stiff\_yoda1} = 1.1e^{-04}$. ***p<0.01*

Yoda1 generally has been used in acute assays rather than chronic treatments, and, as its exact mechanism is not well known, further experiments would be needed to confirm the

validity of Yoda1s use in chronic assays. As a preliminary exploration of this, I first assessed the nature of the calcium signal induced by Yoda1.

Immediately following Yoda1 application, axons showed an increase in rapid calcium flickers, and calcium levels began to increase. Ten minutes later, an obvious global elevation of intracellular calcium was visible (Figure 5.6A). This gradual and sustained elevation of intracellular calcium is consistent with previous calcium imaging studies using Yoda1 to activate human Piezo1[178].

As calcium transients are thought to slow neuronal growth[223], this could be the cause of the phenotype observed in the Yoda1 treated explants. Additionally, a sustained global elevation of calcium might activate pathways leading to cellular damage and death[241,242].

To determine more clearly how Yoda1 treatment distorts axonal morphology, I stained cultures treated overnight with Yoda1 for β-tubulin and VAMP2 (synaptobrevin, Vesicle Associated Membrane Protein 2). VAMP2 is an important, neuronal specific vesicular SNARE protein involved in growth cone chemoattraction, as well as neuritogenesis under certain conditions[60,243]. It was chosen because it should visualize a subpopulation of transport vesicles within the axon and growth cones[244].

The Yoda1 treated neurites appeared to have a disrupted cytoskeleton, as indicated by the tubulin staining, consistent with the large number of axonal varicosities visible even in bright field images of these neurites (Figure 5.6B). VAMP2 distribution was also observationally affected, exhibiting larger accumulations in the Yoda1 treated explants. It should be noted that rigorous validation of the VAMP2 antibody was not undertaken here, though it has been validated in western blots against *Xenopus* tissue (Roberta Cagnetta, personal communication). Finally, to observe if axonal varicosities and the apparent tubulin disruption altered transport in live cells, I injected embryos with an RNA construct encoding the mCherry fluorescent protein. The mCherry construct is enthusiastically translated in RGCs, and excess protein seems to build up in vesicles that can then be visualised moving up and down the axons. While these results are still preliminary, it was possible to observe the appearance of disrupted transport around axonal varicosities in eye primordia explant cultures treated overnight with Yoda1 (Figure 5.6).

While control experiments using other methodologies to chronically elevate calcium would be useful to validate this hypothesis, these results indicate that the results of experiments with chronic Yoda1 treatment may reflect the influence of an excessive

global calcium elevation rather than more precise effects of Piezo1 signalling. That is, Piezo1 channels may simply be held open, allowing calcium to flood the cell, rather than activating specific pathways that may be targeted by endogenous Piezo1 signalling, due to, for example, activation of specific effectors targeted to microdomains proximal to Piezo1 channels.

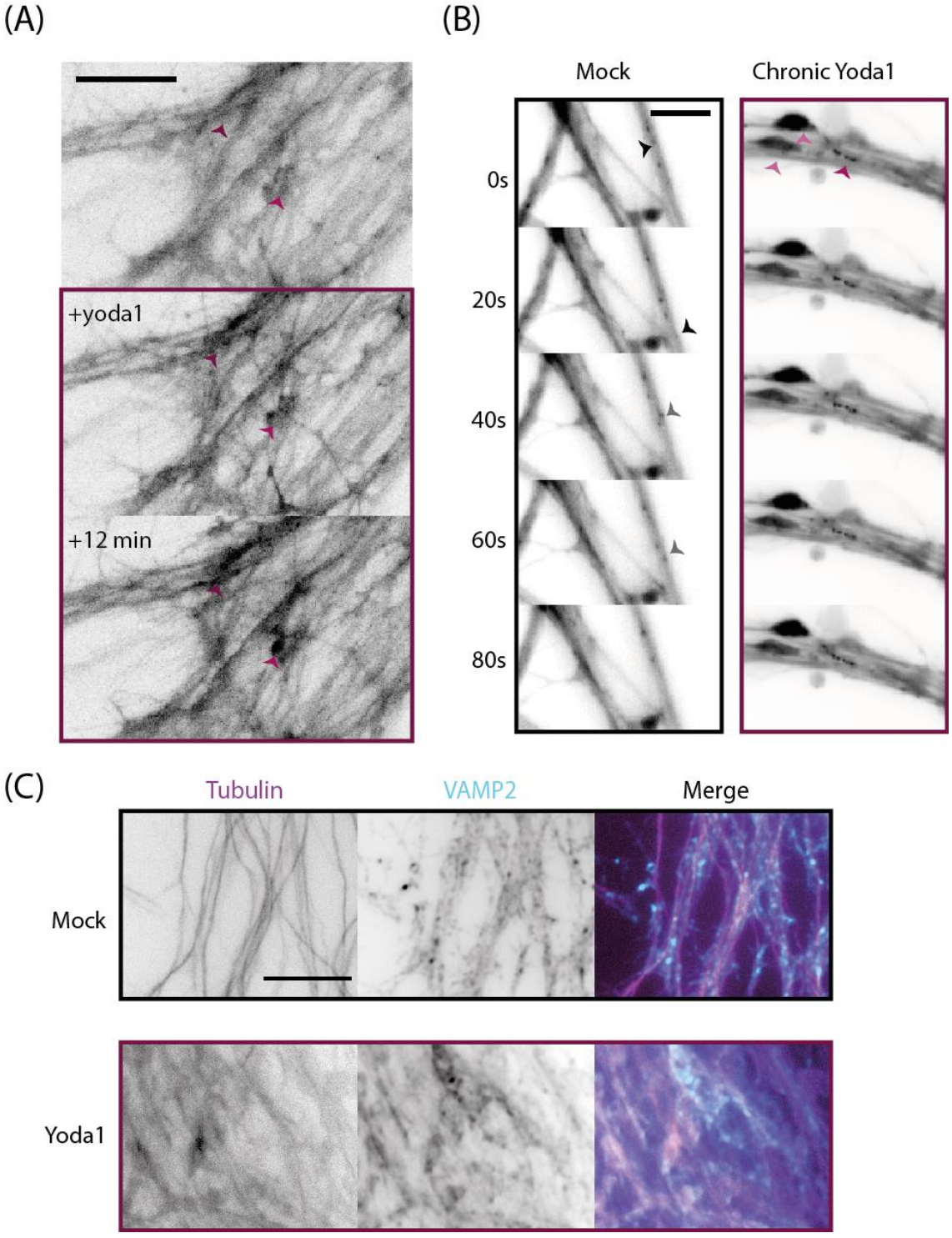

Figure 5.6: Preliminary investigation of the impacts of Yoda1 treatment

Figure 5.6: (continued)

Preliminary investigations suggest that chronic Yoda1 treatment causes an accumulation of intracellular calcium and possibly leads to cytoskeletal disruption. These results are preliminary and would need to be repeated for a more rigorous and quantitative analysis (A) Inverted fluorescence images showing calcium imaging of Yoda1 added to RGC cultures expressing the genetically encoded calcium indicator jRCAMP1b. The frames shown are, first, before addition of Yoda1, next, immediately after addition of 2.5 µg/mL Yoda1, and finally, after the explant has incubated with Yoda1 for 12 minutes. An accumulation of calcium can be observed (for example, compare the points indicated by red arrows). Imaging conditions were sufficiently gentle that the accumulation of calcium is unlikely to be due to damage from phototoxicity. Scale is 20 µm. (B) Stills from movies of mCherry-expressing explants treated overnight with 2.5 µg/mL Yoda1 (magenta outline) or a mock treatment (black outlines). These preliminary results suggested problems with cytoskeleton and transport in these cells. The highly-expressed mCherry protein accumulates in vesicles which are transported along axons. In the control (left, black outline) these vesicles move quickly along axons; for examples the same vesicles in subsequent frames are indicated by black or gray arrowheads. In the Yoda1 condition (right, red outline) I sometimes observed the accumulation of vesicles (red arrow) in front of axonal varicosities (light pink arrow). Timestamps are in seconds, and the scale bar is 10 µm. (C) Representative images from ICC of RGC cultures treated overnight with 2.5 µg/mL Yoda1 or mock treatment. Axons were stained for tubulin and VAMP2. In this example the tubulin stain appears particularly pathological, but there was some variation in this across different explants. Scale is 10 µm.

5.2.3 Yoda1 treatment does not influence growth cone collapse

As chronic elevation of Yoda1 seemed likely to cause nonspecific effects via the accumulation of intracellular calcium (Figure 5.6), I attempted a collapse assay using a relatively acute stimulation with Yoda1. Yoda1 was added for 10 minutes prior to Sema3A, which was then allowed to collapse growth cones for 10 minutes before cultures were fixed and counted. Yoda1 treatment did not influence basal collapse rates, and, unexpectedly, pre-treatment with Yoda1 did not seem to influence the collapse response (Figure 5.7). This is especially odd, as the increase in intracellular calcium observed in Yoda1 treated explants (Figure 5.6) would be expected to cause a reduction in collapse even independent of any Piezo1 specific ramifications of Yoda1 treatment.

This set of experiments used a high concentration of Sema3A (450 ng/mL); in case the response was saturating and a strong dose of Sema3A might be obscuring the influence of Yoda1 treatment, I conducted one additional replicate using a lower concentration of Sema3A (250 ng/mL). However, this did not reveal any additional influence of Yoda1 on the growth cone response to Sema3A (Figure 5.7).

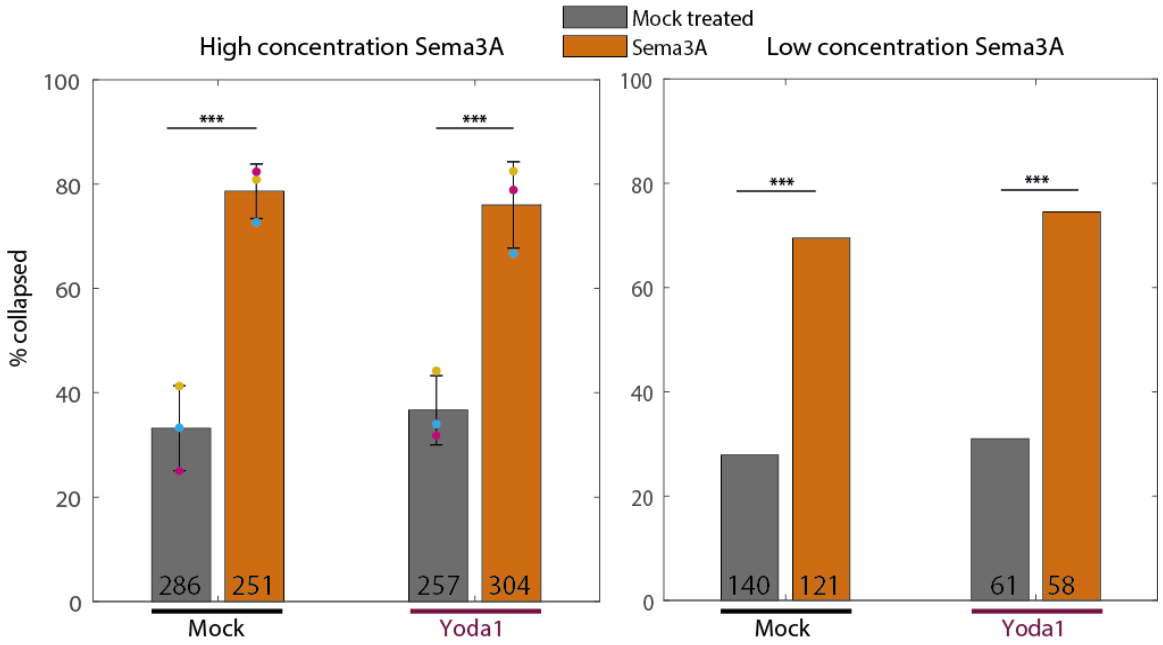

Figure 5.7: Collapse assays on glass substrates with Yoda1 pre-treatment

Acute treatment with Yoda1 does not seem to influence the collapse response to Sema3A in RGC growth cones. Left: growth cones were collapsed with 450 ng/mL Sema3A. Bar heights indicate the mean of three biological replicates. Individual data points are scattered on the bars and colour-coded by replicate, and error bars indicate the standard deviation among these three replicates. Numbers on bars indicate the total number of growth cones counted for each condition, pooled from all three replicates. P-values result from a Pearson Chi-Square test conducted on pooled growth cone numbers. For clarity, not all significance bars are included on the figure. For those shown in the figure: $p_{sema3A \rightarrow ctrl} = 5.3e^{-27}$; $p_{sema3a\_yoda1 \rightarrow ctrl\_yoda1} = 5.8e^{-20}$. *Right: growth cones were collapsed with 250 ng/mL Sema3A. Data are from one biological replicate only. Data were assessed using Pearson Chi-Square tests. For clarity, not all significant bars are included on the figure, for those shown:* $p_{sema3A \rightarrow ctrl} = 2e^{-11}$; $p_{sema3a\_yoda1 \rightarrow ctrl\_yoda1} = 4e^{-08}$. *A table containing all* χ^2 *statistics and p-values for this figure can be found in Appendix 5.2 (Table 10). ***p<0.001.*

5.2.4 Yoda1 does not seem to stimulate calpain activity

Calpain is a cysteine protease activated by Ca^{2+} signals. It is heavily involved in regulation of cell motility via its ability to cleave talin and focal adhesion kinase (FAK) to promote focal adhesion turnover[99]. Calpain has been implicated in mechano-chemical regulation of motility downstream of at least one mechanically gated calcium channel, TRPC1[245]. Moreover, Calpain activity has been directly implicated downstream of Sema3A[96,97], and it has also been suggested that Yoda1-induced Piezo1 activity activates calpain[246].

I assessed calpain activation downstream of Yoda1-induced Piezo1 activation in *Xenopus* RGCs. Calpain activity can be assessed by measuring the rate of cleavage of a fluorogenic calpain substrate, CMAC, *t*-BOC-Leu-Met (7-Amino-4-Chloromethylcoumarin, *t*-BOC-

L-Leucyl-L-Methionine amide, which will be referred to simply as *t*-BOC)[247], a method which has been exploited in *Xenopus* nerons[99,245]. Briefly, *t*-BOC enters cells where it is cleaved by calpain, causing a shift in its emission/excitation maxima. Thus the rate of increase in intensity of the fluorescence signal near the emission maximum for the calpain cleavage product can be taken to report the activity level of calpain.

As expected, treatment with a potent calpain inhibitor, calpastatin peptide inhibitor (CPI) resulted in strongly reduced fluorescence intensity after 8 minutes of incubation with *t*-BOC as compared to mock treated cultures incubated with *t*-BOC over the same time period (Figure 5.8). I found that under regular imaging (i.e. every few minutes over a 20-30 minute time period) the intensity of the *t*-BOC signal increased and then seemed to plateau at around 10 minutes. In principle this assay should result in continuously increasing fluorescence so long as calpain is active; the plateau effect seemed to be due to photobleaching (Figure S 3). I therefore decided to image only at two distinct time points, 8 and 16 minutes after addition of *t*-BOC + Yoda1 or mock solution.

The results of this assay in RGCs were unexpected: Yoda1 treatment seemed to result in less calpain activity than was observed in mock treated cultures. In the mock treated cultures, mean fluorescence intensity in the regions imaged at 16 minutes was 2.3 fold greater than in those imaged at 8 minutes. For Yoda1-treated cultures the fold change was 1.9 (Figure 5.8).

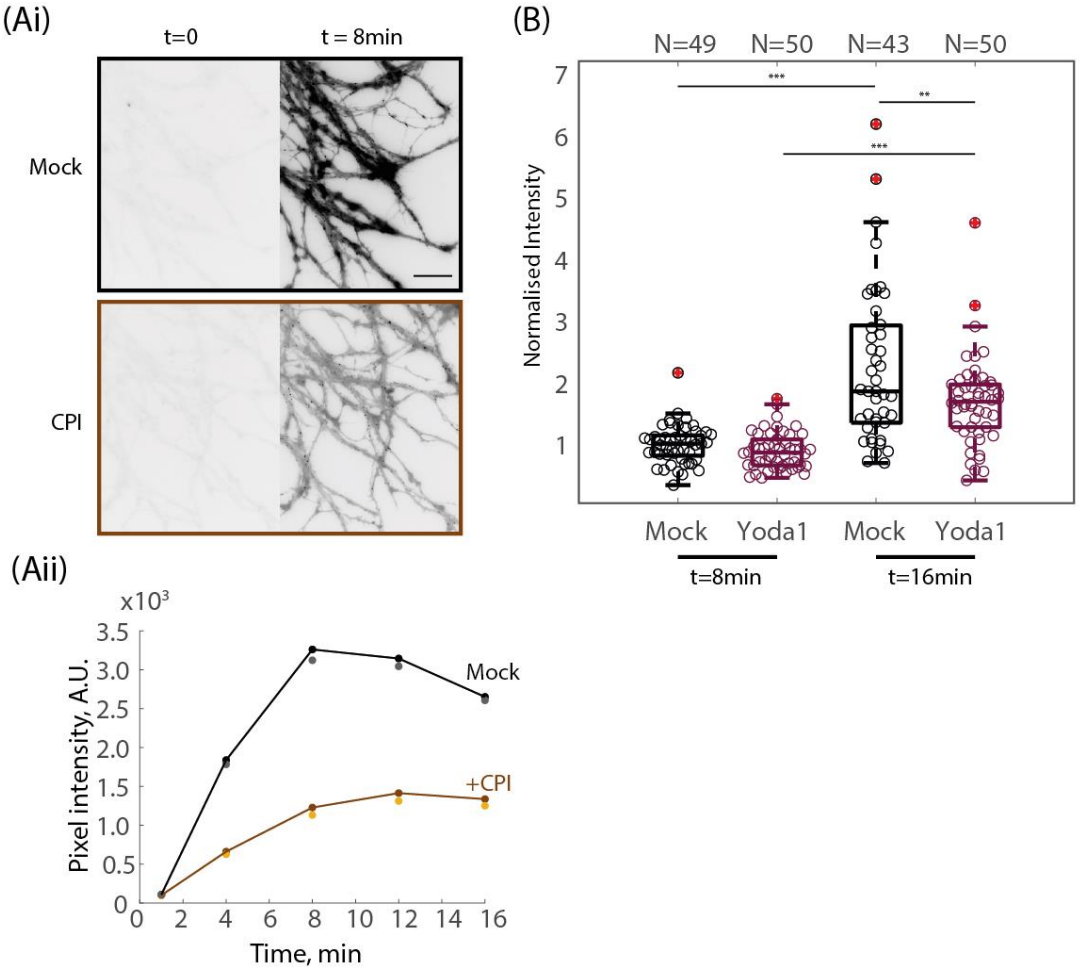

Figure 5.8: Yoda1 treatment does not activate calpain in RGC axons

Figure 5.8: (continued)

*Analysis of the fluorogenic calpain substrate t-BOC indicates that Yoda 1 does not activate, and may in fact mildly inhibit, calpain activity in this system. (A) Validation of the t-BOC assay using an inhibitor of Calpain, the calpastatin inhibitor peptide (CPI). Compared with mock treated cultures, cultures treated with 1µm CPI demonstrated a strongly reduced increase in fluorescence intensity (Ai) Images are shown from immediately and 8 minutes after addition of t-BOC. Scale bar is 25 µm. (Aii) Time series showing mean fluorescence intensity in a region of a culture containing either CPI or a mock treatment imaged every 5 minutes. Regions that that were densely covered with axons were selected for analysis. Lines and darker circles show means, lighter circles are medians. The slope of the initial increase is much more rapid in cultures without CPI. After about 10 minutes fluorescence seems to plateau and begin to decrease slowly. (B) Yoda1 and t-BOC were added simultaneously, and axons on 100 and kPa substrates were imaged after 8 and again after 16 minutes. As expected for cells containing functional calpain, fluorescence increased strongly over this time period. However, the presence of Yoda1 did not lead to a larger relative increase in fluorescence, as would be expected for a calpain activator. These cells were analysed using the height of Gaussian fits to profiles drawn across axons, as explained in Figure 4.7. Data are from three biological replicates with each replicate normalized so that the mean value of the mock treated cultures at 8 minutes is set to 1. Total number of axons analysed for each condition (N) are stated above the boxplots. Data were analysed using an ANOVA ($p=7.9e^{-18}$) followed by a Bonferroni post hoc test. Values shown on plot: $p_{mock8min \rightarrow mock16min} = 3.8e^{-09}$, $p_{yoda8min \rightarrow yoda16min} = 3.9e^{-07}$, $p_{mock16min \rightarrow yoda16min} = 0.0013$; additionally: $p_{mock8min \rightarrow yoda16min} = 1.6e^{-05}$, $p_{yoda8min \rightarrow mock16min} = 3.8e^{-09}$. **p<0.01, ***p< 0.001.*

5.3 Chapter conclusions and outlook

These experiments produced conflicting results regarding the potential role of Piezo1 in determining how substrate stiffness influences axon guidance signals. On glass substrates, the MO KD of Piezo1 produced a robust effect on neurite outgrowth: RGCs with Piezo1 knocked down extended significantly further over 24 hours than control axons. The same effect was not observed on gels, regardless of stiffness. Chronic treatment with the Piezo1 agonist Yoda1 resulted in a reduction in outgrowth on both glass substrates and gels. However, Yoda1 treatment did not seem to result in activation of calpain, which is implicated downstream of Piezo1, and Yoda1 treatment also did not alter the proportion of growth cones that collapsed in response to Sema3A.

While additional experiments will be needed to definitively determine the role of Piezo1 in RGC mechanosensitivity, a few observations can still be made.

5.3.1 Growth phenotypes under Piezo1 modulation

Knockdown of Piezo1 increases explant outgrowth on glass (Figure 5.2), but not on compliant hydrogels (Figure 5.3). Piezo1 KD should have no effect under conditions in which Piezo1 is not active. One hypothesis might therefore be that Piezo1 is not very active on polyacrylamide hydrogels regardless of stiffness. Glass presents explants with

a very different environment than gels, not only in stiffness, but also as regards adhesion. It has recently been suggested that Piezo1 calcium flickers are activated immediately around adhesion sites by forces concordant with traction forces generated at adhesions and dependent on myosin activity[175]. Neurons normally generate quite weak forces, and perhaps on gels these are not strong enough to activate Piezo1. This hypothesis could be tested by a more thorough exploration of adhesion conditions. In these experiments, all substrates were coated with laminin. Coating glass substrates instead solely with PDL, for example, would provide an environment in which integrins could not be engaged. One might then expect that Piezo1 KD would not influence RGC outgrowth on glass.

Another possible explanation is some sort of functional compensation. Such a mechanism has been observed for the MSC TRPC1. Calcium transients mediated partially by TRPC1 are important for pathfinding, but *Xenopus* spinal neurons with TRPC1 knocked down had similar rates of outgrowth and basal calcium activity to control neurons; a phenotype resulting from TRPC1 KD only emerged upon perturbation[245]. This was proposed to be because other MSCs were able to compensate for reduced TRPC1 under normal growth conditions. In the case of Piezo1, perhaps glass presents a sufficiently pathological environment that neurons are unable to effectively compensate for the loss of Piezo1.

Yoda1, the Piezo1 agonist, provoked a growth reduction following chronic treatment on both gels and glass; however, these results should be interpreted with caution as it is possible that morphological changes are due to neuron damaged linked to an excessive calcium influx.

In general, the growth phenotypes for Piezo1 knockdown and Yoda1 treatment are the opposite of those that might be expected based on our previous work[123] in which we found that treatment with the Piezo1 inhibitor GsMTx-4 reduced outgrowth on both soft and stiff substrates. One possible explanation for this is that chronic GsMTx-4 might, similarly to chronic Yoda1 treatment, activate other pathways that overwhelm any Piezo-1 specific impacts. Indeed it was previously observed that acute application of GsMTx-4, as well as other MSC inhibitors, increased neurite outgrowth rates, leading to the hypothesis that calcium influx through MSCs was generally inhibitory to axon outgrowth [248].

5.3.2 Yoda1

The Yoda1 results present somewhat of a dilemma— Yoda1 treatment induced a calcium influx, but failed to either influence the Sema3A response or to activate calpain. Even if

the Yoda1-induced calcium influx was unspecific, one would expect to observe some modulation of the Sema3A response, which is acutely sensitive to calcium levels[212]. One curious option can be presented here: generally, low calcium elevations are associated with repulsion and more intense calcium elevations with attraction. However, one paper has suggested, and experimentally demonstrated, tri-phasic growth cone turning responses, such that an even more intense calcium influx could actually revert an attractive growth cone response back to a repulsive one[212]. Perhaps calcium increase due to Yoda1 stimulation is sufficiently extreme to push the growth cone into this regime. This hypothesis could be tested by conducting additional collapse assays using lower concentrations of Yoda1 pre-treatment.

5.3.3 Outlook

The results presented in this chapter did not provide a clear indication of whether Piezo1 activity is modulated by changes in substrate mechanics. I therefore decided to examine directly the mechanisms by which Piezo1 might be gated in these cells. Piezo1 gating is not fully understood (See Section 1.3.2.1); however, it is clear that changes in lipid bilayer tension play a critical role. I therefore began by explicitly measuring membrane tension as a function of substrate stiffness, and these measurements are the topic of the next chapter.

6 MEMBRANE TENSION OF RGC AXONS ON SOFT AND STIFF SUBSTRATES

6.1 Membrane tension and substrate stiffness

Piezo1 channels are able to sense forces propagated through the bilayer without the need for any intermediates[160,164,249], and are sensitive to changes in the lipid environment[172,173].

MSCs, including Piezo1, have been shown to be more active on stiffer substrates[123,142,245,250]. However, how a change in substrate stiffness might result in increased forces transmitted to MSCs is not clear. In particular, to my knowledge no study has explicitly examined whether membrane tension changes in response to substrate-stiffness.

To determine if changes in substrate stiffness caused alterations in membrane tension that might influence gating of Piezo1 channels in RGCs, I measured membrane tension of *Xenopus* RGC axons as a function of substrate stiffness in collaboration with Jeffrey Mc Hugh in the lab of Ulrich Keyser in the Cavendish laboratory at the University of Cambridge.

6.2 Optical tweezers measurements of axonal membrane tension on soft and stiff substrates

Membrane tension was measured by pulling thin membrane tethers using optical tweezers. A rich body of work underlies the interpretation of biophysical membrane parameters such as tension from the forces needed to extract thin membrane tubes from cells[251–253]. The lab of Michael Sheetz first demonstrated the use of a functionalized bead held in an optical trap to probe neuronal membrane properties[254,255]. In this experiment, a bead coated with a membrane adhesive moiety such as concanavalinA (conA) is approached to the cell. After the bead adheres to the cell membrane, it is retracted to a set length and/or with a set velocity, and the forces required to pull and maintain the tether in its steady state are observed (Figure 6.1). Isolating the different parameters that

contribute to this force (Eq. 1, $F = 2\pi\sqrt{2TB}$, $T = T_m + \gamma$) requires measurement of tether radius and of the tension measured in a cytoskeleton-free bleb, as these parameters are used to de-convolve the bilayer tension T_m from the contribution of membrane cytoskeletal adhesion, γ, and the bending modulus, B[181,182] (see Section 1.3.3). The results below report only F; no attempt has yet been made to address the relative contributions of T_m, γ, and B.

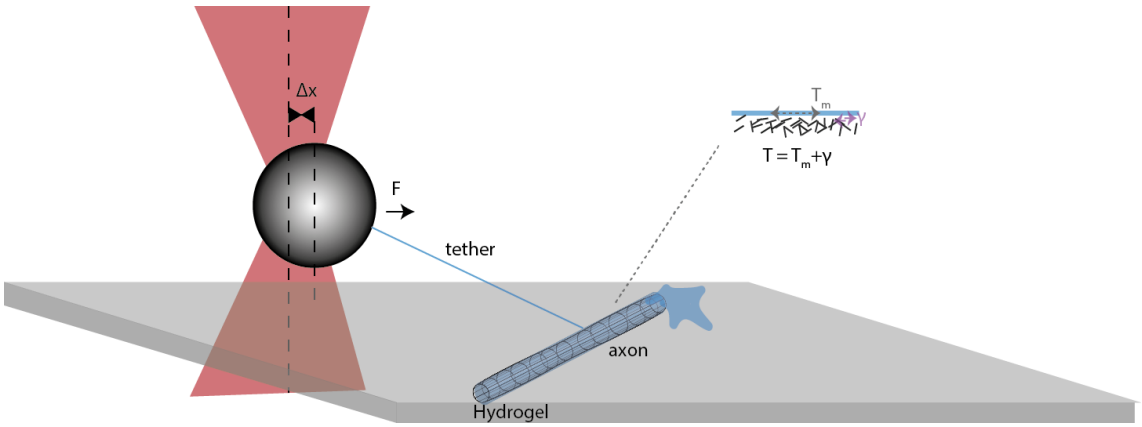

Figure 6.1: Principle of optical tweezers measurements of membrane tension

Membrane tethers are extracted via a conA-coated bead held in an optical trap of known stiffness k (see Methods, Section 2.11). The force F exerted by the tether pulls the bead a distance Δx from the centre of the optical trap. In which case F = kΔx, and $T = \frac{F^2}{8\pi^2 B}$, *where B is the membrane bending rigidity. The apparent tension T is a combination of the bilayer tension* T_m *and the membrane-cytoskeletal adhesion term γ. Diagram borrows conceptually from*[256].

Statement of contributions: The custom built optical tweezers setup used for the following experiments was constructed by Kurt Andresen (visiting Professor at the Cavendish Laboratory, currently at Gettysburg College, PA, USA) and Jeffrey Mc Hugh (Cavendish Laboratory). I performed dissections and cell culture. Optical tweezers experiments were conducted together with Dr. Andresen and/or Mr. McHugh. Mr. Mc Hugh wrote the analysis programs and analysed the data. Mr. Mc Hugh and myself reviewed individual videos and force curves together in order to refine the data.

We established a system that allowed us to pull membrane tethers as well as capture high resolution fluorescence images of axons. For these experiments, we used axons from embryos injected with TMR-dextran, as this label provides an extremely bright signal without adversely affecting the health of the embryos.

Tethers were pulled from RGC axons from eye primordia explants grown on glass and 100 Pa or 1 kPa hydrogel substrates. There was no significant difference between force values measured on 100 Pa (F = 15.9 ± 5.0 pN, mean ± standard deviation) and 1 kPa (F = 16.8 ± 4.8 pN) substrates. Interestingly, the force values on glass (F = 8.5 ± 4.1 pN) were significantly smaller than those on either of the gels (Figure 6.2). These values are

relatively consistent with previous measurements of membrane tension in embryonic neurons[257].

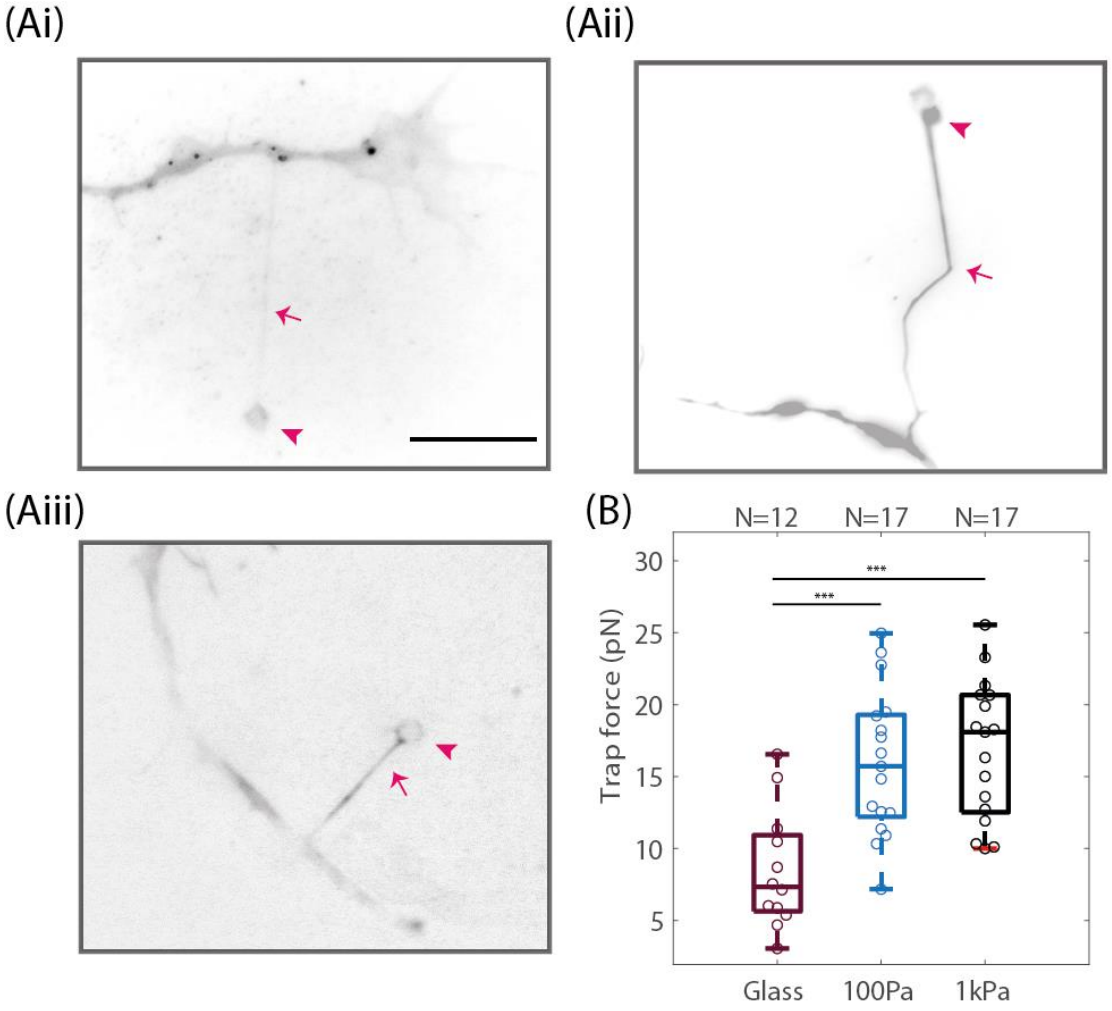

Figure 6.2: Membrane tension is similar on soft and stiff substrates

Figure 6.2: (continued)

*Optical tweezers measurements of membrane tension on glass and hydrogels. (A) Inverted fluorescence images of tethers pulled from RGC neurons; arrowheads indicate beads, arrows indicate tethers. (Ai) A thin tether with the growth cone clearly visible to the right. (Aii) A tether that appears visually thicker than the 'normal' tether in Ai, possibly suggesting the presence of cytoskeletal filaments. (Aiii) In this situation the tether slid to attach to a thin cell protrusion of some type (the curvy region), and then continued to grow out of the tip of this protrusion (straight region) (This tether was not included in the analysis in B). (B) Trap force values for tethers pulled from axon shafts on 100 Pa, 1 kPa, and glass substrates. Each point represents a single tether, data come from three (glass) or four (gels) separate days of measurements, and the total number of tethers pulled for each condition (N) is stated above the bars. Data was assessed with an ANOVA ($5.3e^{-05}$), and subsequently with a Bonferroni post hoc test. Force values did not differ significantly between axons on 100 Pa and 1 kPa substrates ($p = 0.85$); however trap forces were significantly greater for axons on hydrogels than on glass ($p_{glass \rightarrow 1kpa} = 8.6e^{-05}$, $p_{glass \rightarrow 100pa} = 4.2e^{-04}$). ***$p<0.001$.*

During the course of the experiments we made several additional interesting observations about the behaviour of the membrane tethers.

First, there was a large amount of diversity in the appearance of the force curves (Figure S 5). While many contained an overshoot followed by a return to steady state, similar to force profiles reported in the literature for membrane tethers pulled from neurons[258], no single profile dominated. Second, tethers slid easily, i.e. the base of the tether was often observed to move along the axon rather than remain stationary. Gradients of membrane tension have been reported in neurons[259], but we did not distinguish any clear directionality in spontaneous tether sliding that might indicate the existence of a stable tension gradient. Third, while our spatial resolution was not sufficient to determine the radii of the tethers (which generally requires electron microscopy), observationally there were high levels of variation in the widths and overall appearance of the tethers, suggesting that cytoskeletal elements might have invaded a subset of tethers (Figure 6.2). These observations will be further discussed in (Section 7.4.1.2)

6.2.1 Preliminary data from an optical membrane tension dye

Statement of contributions: I prepared RGC cultures, Ryan Greenhalgh and I conducted imaging with the help of Kevin O'Holleran in the Cambridge Advanced Imaging Centre. Mr. Greenhalgh completed downstream analysis.

Optical tweezers measurements of membrane tension have very limited spatial resolution. It is possible that Piezo1 is activated by small-scale spatiotemporal fluctuations in membrane tension, rather than global changes in the average value of membrane tension.

An optical membrane tension dye called FliptR (fluorescent lipid tension reporter) has recently been published[185]. The FliptR probe intercalates into the membrane and changes

in the fluorescence lifetime of the probe linearly correlate with increases in membrane tension.

Together with Ryan Greenhalgh, I have begun exploring the use of this dye to obtain membrane tension measurements in RGCs with high spatiotemporal resolution. These experiments are ongoing. Preliminarily, in our hands the dye gives an excellent fluorescent signal, and there appears to be higher tension around the periphery of the growth cones. Moving forward we hope to measure dynamics of membrane tension with FliptR on 100 Pa and 1 kPa substrates to compliment the optical tweezers measurements.

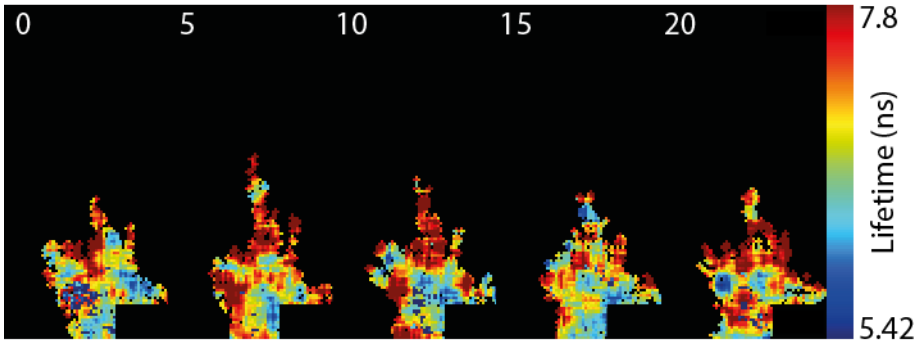

Figure 6.3: Preliminary experiments with FliptR on glass substrates

Fluorescence lifetime images taken from a time-lapse move of growing Xenopus RGC neurons. Red colours indicate greater dye lifetimes and higher membrane tension. Blue colours indicate lower dye lifetimes and lower membrane tension. Timestamps are in minutes. These experiments were conducted in collaboration with the Cambridge Advanced Imaging Centre. Images and analysis courtesy of Ryan Greenhalgh.

6.3 Conclusions and Outlook

The measurements presented here suggest that, as expected considering literature values for embryonic neurons[257,259], tethers pulled from RGCs exert low forces on the optical trap, suggesting low membrane tension and/or weak membrane-cytoskeletal adhesion. Furthermore, we did not observe a significant difference in trap force values between axons grown on soft and stiff substrates. Interestingly, membrane tension did seem to differ between hydrogels and glass: trap force values were significantly lower on glass.

These observations, and their potential implications for Piezo1 gating will be discussed more in Section 7.4.1.

7 DISCUSSION

7.1 Mechanical control of the Sema3A response

The results presented here demonstrate that variations in substrate stiffness within the physiological range encountered by navigating RGC axons are able to modulate the response of growth cones to the guidance cue Sema3A.

Additionally I have shown that softer substrates elevate basal levels of growth cone cGMP, and that this is likely the proximal cause of the reduced response of growth cones to Sema3A on soft substrates (Figure 4.3, Figure 4.4). Softer substrates also cause a more depolarized membrane potential (Figure 4.7). This is possibly dependent on the cGMP elevation observed on soft substrates, as increased cGMP can cause membrane depolarization in a PKG-dependent manner[48]; however I have not yet demonstrated this connection explicitly. I also observe more frequent calcium transients on soft substrates, which is consistent with a more depolarized membrane presenting a more permissive environment for the activation of voltage-gated calcium channels (Figure 4.9). A more depolarized resting membrane potential would also be expected to result in an increased calcium influx upon Sema3A stimulation (and therefore a less repulsive Sema3A response[48,212]).

In the following sections I will discuss the potential implications of mechanical regulation of the Sema3A response in *Xenopus* brain (Section 7.1, Figure 7.1), and comment briefly on other tissues where Sema3A signalling plays critical roles (Section 7.2.2.1). Finally, I will discuss more generally the role of chemical gradients in axon guidance and the potential importance of mechanical signals as a mechanism to increase the specificity and robustness of chemical signals (Section 7.2.2). The regulation of the Sema3A response through cyclic nucleotide levels implies that this mechanism may be broadly applicable to other guidance cues, and I will discuss this in Section 7.2.3.

The mechanosensory element responsible for these effects has proven difficult to identify. We have previously demonstrated that Piezo1 is necessary for axon pathfinding in the *Xenopus* optic tract; however, further experiments are needed to determine precisely how Piezo1 functions in axon guidance. In Sections 7.3 and 7.4 I will discuss the potential role

of Piezo1 in *Xenopus* RGCs, and comment on the connection between substrate stiffness and Piezo1 gating. Additionally I will suggest other potential mechanosensors that might contribute to the mechanical regulation of the Sema3A response (Section 7.5).

7.2 Scope and significance

The finding that substrate stiffness robustly influences the Sema3A response is an important addition to our understanding of the subtle regulation of signalling pathways in axon guidance.

Sema3As has generally been considered to act, by default, as a highly repulsive or collapsing signal, because this is how it acts in the most experimentally accessible assay: *in vitro* collapse or turning assays conducted on glass or plastic substrates. My results suggest that, particularly in the very soft tissues of the nervous system, this assumption might not be valid. Moreover my results indicate that small alterations in substrate stiffness could provide a sensitive way for developing tissues to tune cellular responses to Sema3A.

In the following section, I will offer some thoughts on how mechanical regulation of the Sema3A response may increase the fidelity of axon pathfinding in the *Xenopus* optic pathway.

7.2.1 Potential *in vivo* role of mechanical modulation of the Sema3A response

I studied the Sema3A response in the context of RGC pathfinding. The physical environment through which RGC axons navigate during their growth through the *Xenopus* optic tract (Section 1.2.1) has been extensively characterized[123,132]. As described in more depth in Section 1.4, *Xenopus* brain tissue is soft and mechanically heterogeneous. Growing RGCs navigate through a mechanical environment that changes over time, and in particular, a stiffness gradient develops that temporally precedes the turning of the axons at a critical bend in their growth trajectory[132] (Figure 1.10).

We have previously found that this stiffness gradient may impact axon guidance via direct neuronal mechanosensing. That is, neurons navigate down the stiffness gradient towards softer regions (which is their behaviour in *in vitro* stiffness gradients, see Figure 1.9). Thus the stiffness gradient orients RGC growth in concert with the chemical gradient of Sema3A[123]. The findings in this thesis raise the possibility of a different, or possibly complementary, mechanism of regulation: increased stiffness should cause RGCs to

respond more strongly to Sema3A, turning away more sharply in response to a Sema3A gradient. Thus, axons encountering a stiffer environment, towards the anterior aspect of the optic tract, should respond more strongly to Sema3A then those axons nearer the posterior aspect of the optic tract, which encounter a softer environment. This additional level of regulation could help curb stray axons venturing towards to Sema3A gradient. The reduced stiffness on the posterior side of the optic tract could reduce the Sema3A response here, and therefore prevent excessive turning (Figure 7.1).

RGCs gain the ability to sense the Sema3A signal via a developmentally-regulated increase in receptor expression[115]; tissue stiffening during brain development could serve as an additional, partially redundant mechanism (Figure 7.1). This thesis did not explore how the Sema3A response changes at stiffnesses lower than G' = 100 Pa, but *Xenopus* brain tissue can probably reach significantly softer values[123,132]. Specifically, the values of brain stiffness recorded in Figure 1.10 range from K = 50-250 Pa, where K is that reduced apparent elastic modulus. This corresponds to shear moduli of approximately G'= 15-75 Pa. ($K = \frac{E}{(1-\gamma_p{}^2)}, E = 2G(1 + \gamma_p)$, where γ_p is Poisson's ratio and E is Young's Modulus. Assuming γ_p = 0.4, G = 0.3K. γ_p = 0.5 for a perfectly elastic material, but Xenopus brain tissue is viscoelastic and a better estimation is likely a slightly lower value (Ryan Greenhalgh and Joy Thompson, personal communications).)

If levels of cGMP continue to increase with decreasing substrate stiffness, one could envision that the response to Sema3A might be completely abolished, or even become attractive at very low stiffness. Thus Sema3A might initially provide an attractive cue, and, when the brain stiffens and the gradient in stiffness develops, might only then provide a spatially constrained region of repulsion. Such a mechanism would not only be consistent with the observed growth pattern of RGCs, it would also serve as a redundant mechanism to the proposed concentration gradient of Sema3A, potentially making this signal more robust and less prone to noise-based errors (Figure 7.1, See also Section 7.2.2).

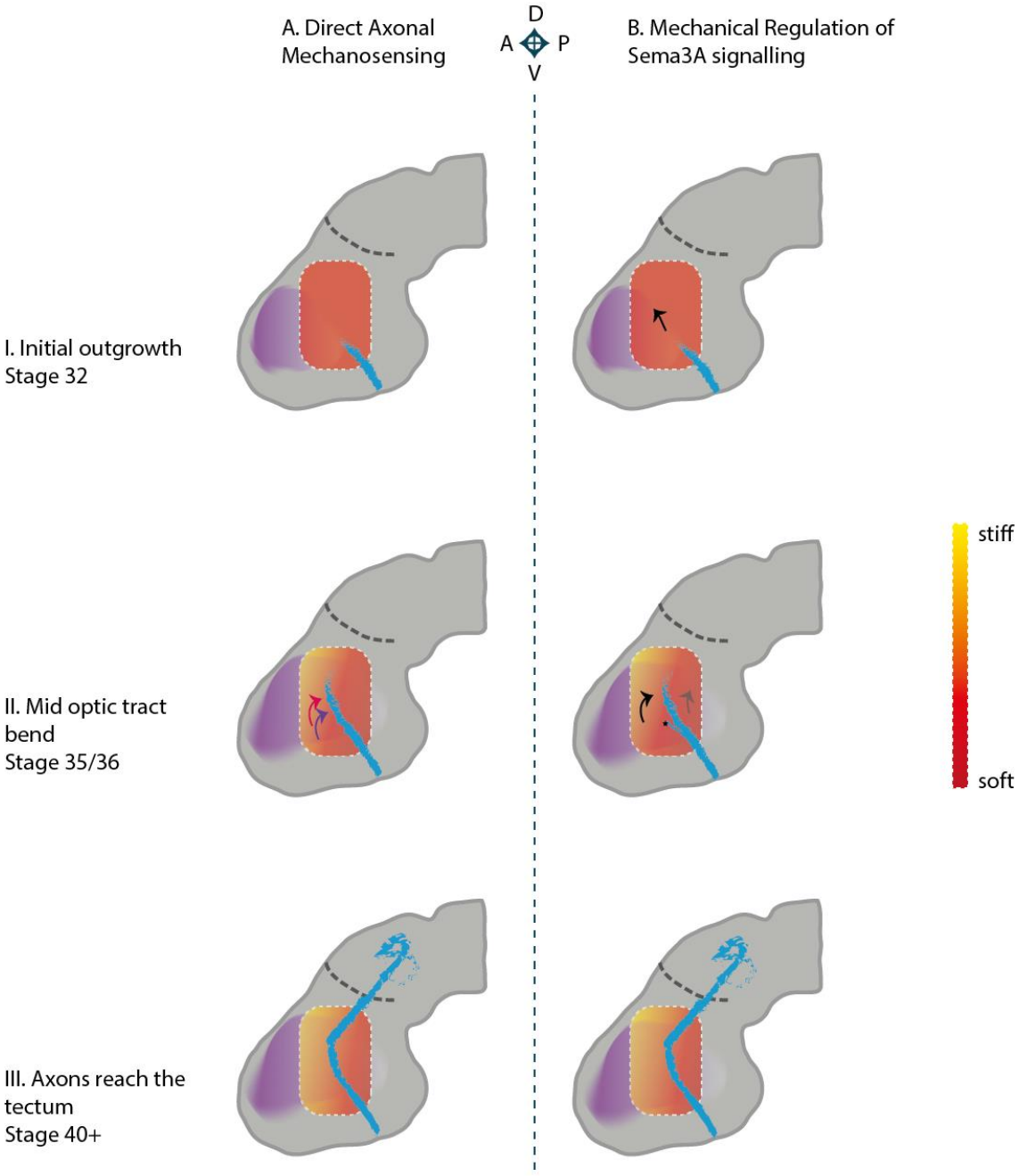

Figure 7.1: Possible mechanisms of mechanical regulation of the Sema3A response in the Xenopus brain

Figure 7.1: (continued)

Mechanics may play multiple important roles in axon guidance in the Xenopus optic tract. (A) Our previous hypothesis for mechanical regulation of the Sema3A response, based on the finding that stiffness gradients can guide RGC axons: RGCs navigate down stiffness gradients (yellow→red gradient, red arrow in ii) towards softer regions. This may function additively or synergistically with the Sema3A gradient (purple→white gradient, purple arrow in ii) during axon turning at the mid-optic tract band. (B) Additional modes of regulation are suggested by the results presented in this thesis. (i) Early during the outgrowth of the optic tract, axons have begun to express Sema3A receptors[115] and Sema3A mRNA is present. Low stiffness might make the Sema3A patch attractive (or at least not repulsive), thereby encouraging (or at least not discouraging) axon growth. If this layer of regulation is not present, this region of Sema3A would still be expected to serve as a repulsive signal, which is less consistent with the axonal growth trajectory (though other cues of course play a role). (ii). At the mid-optic tract bend, higher stiffness on the anterior side of the optic tract facing the Sema3A localisation may induce axons to respond to the Sema3A with a strong repulsive turn (black arrow), helping to coral stray axons (arrowhead), on the side further from the Sema3A, the response is diminished due to reduce tissue stiffness (gray arrow), which reduced response may help prevent over-turning of the axons. (iii) Axons reach the optic tectum. D,V,A,P: Dorsal, Ventral, Anterior, Posterior.

7.2.2 Gradient sensing and the importance of collaboration among signalling modalities

How the region of Sema3A expression proximal to the optic tract actually functions to direct axon growth has not been shown definitively. The distribution Sema3A in Figure 7.1 represents the RNA expression patterns that have been visualized with *in situ* hybridization[115,116]. However, no reliable data are available for the Sema3A *protein* expression in this region, in part due to the fact that the relevant protein population is a secreted, extracellular one which complicates immunostaining.

Due to its localisation proximal to a critical turning point in the RGC axon tract, and its ability to cause repulsive turning *in vitro*, it has been assumed that a secreted gradient of Sema3A repels axons *in vivo*. However, the formation of a sufficiently stable, long range gradient in a complex and developing tissue is nontrivial[260]. Moreover, based on purely physical constraints (such as, for example, the noise inherent in ligand detection and signal amplification), the ability of molecular gradients alone to provide sufficiently precise information to produce the complex neuronal trajectories observed *in vivo* has been questioned[261].

Mechanics and adhesion might act as an additional regulatory mechanism to better ensure the robustness and reproducibility of chemical guidance[260]. Due to both axonal mechanosensing and mechanical regulation of the Sema3A response, the addition of a substrate stiffness gradient to even a homogeneous level of Sema3A would be expected to provoke a directional response. In the case of the *Xenopus* brain, Sema3A is may

already be present in a gradient, in which case the response will be further accentuated by the substrate stiffness gradient, as well as being spatially constrained.

7.2.2.1 Sema3A in other contexts

Sema3A is a widely expressed signalling molecule. In addition to its roles in many parts of the nervous system[79,80,262], Sema3A/PlxA1/Npn1 signalling is indispensable in numerous biological contexts, including, for example, bone formation and maintenance[263–265] and immune suppression and autoimmunity[266,267].

The diversity of environments in which Sema3A signalling is active are replete with instances where mechanics and changes in the mechanical environment may play important roles. To take one of the examples mentioned above, Sema3A was found to promote osteogenic differentiation of bone marrow mesenchymal stem cells[264,268], a process at the interface of two radically different mechanical environments—bone and bone marrow.

It would be interesting to study how the signalling cascade of Sema3A in these other cell types depends on substrate stiffness, and to ascertain if stiffness represents a conserved parameter used to modulate Sema3A/PlxA1/Npn1 signalling across biological contexts.

7.2.3 Substrate-stiffness may modulate the response to numerous guidance cues via cyclic nucleotide levels

I have shown that substrate mechanics regulates Sema3A by altering cGMP levels. cGMP and cAMP are often co-regulated[269,270], and it is thus very probable that the level of cAMP is also altered with substrate stiffness, which I hope to test explicitly in the future. Should this be the case, the potentially broad applicability of this regulatory mechanism would be expanded yet further. cGMP and cAMP are master regulators of numerous guidance cue signalling cascades (see Section 1.1.3), which can rely either on cyclic nucleotide levels, as the Sema3A response, or on the ratio of cAMP to cGMP, as in the Netrin-1 response[42,44,271,272]. Moreover, cyclic nucleotide levels are important in regulating other aspects of growth behaviour, for instance, the degree of alignment of neurons with microtopographical features[273]. Spatial and temporal changes in substrate stiffness could thus provide a general mechanism by which neuronal behaviour is regulated by setting the levels of intracellular cyclic nucleotides.

7.3 Calcium signalling

In the calcium imaging experiments conducted for this thesis, I examined all calcium transients that occurred in a relatively large region densely populated with neurons, at relatively low temporal resolution. Calcium transients occur on this timescale both *in vitro*[222] and *in vivo*[224], and these transients are critically important for regulating numerous aspects of neuronal growth and behaviour. With these experiments I aimed to capture a broad picture of these growth modulatory transients. Neurons express a high density of various different types of calcium channels[274]. Thus once a depolarization is initiated, multiple classes of voltage gated-calcium channels likely open, and the imaging employed here likely captured transients communicated through many types of channels, as well as calcium release from intracellular stores. In preliminary studies using a variety of peptide inhibitors of voltage gated calcium channels, no single inhibitor seemed able to convincingly eliminate spontaneous calcium activity (data not shown). Omega-Conotoxin GVIA, a blocker of N-type voltage gated calcium channels (which are expressed in the ganglion cell layer of *Xenopus* tadpoles[274]), showed a potential reduction in transient frequency. However, these experiments need to be repeated before any conclusions can be drawn.

A main focus of this thesis was the MSC Piezo1. As Piezo1 is a calcium permeant channel, and Piezo1 activity can be measured via calcium imaging[165,250], the question of a contribution of Piezo1 activity to these calcium transients naturally arises. None of my calcium imaging experiments attempted to isolate signals arising specifically from Piezo1 (which would likely be difficult in neurons due to the density of calcium channels). Whole cell influxes of calcium due to Piezo1 activation have been observed, but these were in cells that were both overexpressing Piezo1 and mechanically stimulated with an AFM cantilever[165]. Neurons mechanically stimulated with an AFM cantilever do make large scale calcium elevations which evidence suggests are mediated via Gd^{2+} sensitive MSCs[142], and we were able to occasionally observe similar transients upon AFM simulation of *Xenopus* RGC growth cones (experiments in collaboration with Joy Thompson, data not shown). However, experiments examining the activity of endogenous Piezo1, in the absence of large external mechanical perturbations, have rather found weaker, spatially restricted transients occurring on the timescale of seconds[175,250].

Even if Piezo1 does not serve as the main conduit for calcium in these transients, it is possible that Piezo1 helps to initiate transients that are then amplified by other channels. GsMTx-4 sensitive MSCs have been found to contribute to growth restricting calcium

transients in *Xenopus* spinal neurons[248]. The growth phenotypes observed in my experiments – reduction in outgrowth upon Yoda1 stimulation and increased outgrowth (on glass) upon Piezo1 knockdown, are at least consistent with a similar role for Piezo1. Calcium imaging of Piezo1 KD neurons should help determine if Piezo1 is responsible for any of the observed spontaneous calcium activity.

7.4 Piezo1 gating in RGCs

This thesis did not definitively identify a candidate for the primary mechanosensor responsible for the observed intracellular changes in second messengers.

Our previous work showed that Piezo1 knockdown caused severe axon pathfinding defects[123], which had suggested Piezo1 as a likely candidate; however, so far my results in this regard are not conclusive. Collapse assays and local stimulation experiments with the Biopen using Piezo1 KD axons should help me conclusively determine whether Piezo1 activity regulates the Sema3A response.

In the following sections I will discuss how recent results regarding the mechanism of Piezo1 gating may relate to my findings on neuronal membrane tension.

7.4.1 Piezo1 gating and membrane tension

Xenopus axons and growth cones express relatively high levels of Piezo1[123], indicating that it likely serves an important function. One important outstanding question is how active endogenous Piezo1 is in *Xenopus* growth cones. Moreover, it is not clear whether changes in substrate stiffness within the studied range can modulate Piezo1 activity, and, if so, how this regulation proceeds.

I addressed this by measuring membrane tension in neurons grown on different substrates, based on the idea that lateral bilayer tension is an important contributor to Piezo1 gating[164,249]. In the following sections I will discuss in more detail the interpretation of optical tweezers measurements of membrane tension, and how the values we obtained in our measurements may relate to the actual values needed to gate Piezo1.

7.4.1.1 Role of the Cytoskeleton

The force value that is the primary readout of optical tweezer measurements is related to both the bilayer tension and the membrane-cytoskeletal adhesion, and is also influenced by the bending rigidity (B) of the membrane (Eq. 1: $F = 2\pi\sqrt{2TB}$, Figure 6.1). It is possible to decouple the tension term T ($T = T_m+\gamma$, where T_m is the bilayer tension and γ

is the membrane-cytoskeletal adhesion term) from the bending rigidity by measuring tether radii, in which case one can use Eqs. 2: $T = \frac{F}{2\pi R}, B = \frac{FR}{2\pi}$ [257,275] (see also a more complete discussion in Section 1.3.3).

Separating T_m and γ requires measuring a patch of membrane decoupled from the cytoskeleton. This has been achieved, for example, by inducing membrane blebs[184] or plasma membrane vesicles (PMVs)[257]. These measurements have found that while T varied across cell types, T_m was remarkably consistent. γ was responsible for variations in T among cell types and generally accounted for around 70-90% of T[184,257]. Interestingly, Pontes et al. calculated that in neurons, in contrast to other nervous system cell types, γ comprised only about 46% of T. In fact, the force needed to pull membrane tethers from neurons and from cytoskeleton-free PMVs was nearly identical, at F ≅16 pN (the difference in T arose as PMVs had a twofold higher bending rigidity)[257]. This suggested that neurons have extremely low membrane cytoskeletal adhesion.

Consistent with this suggestion, we regularly observed sliding of tethers even though we never intentionally induced tether sliding. This phenomenon has been observed before in one other instance, in chick dorsal root ganglia neurons[258]. In this study, Datar et al., found that tethers slid easily on neurons, but not on HeLa cells; tether sliding in neurons was relatively insensitive to perturbation of actin, whereas actin disruption in HeLa cells facilitated sliding. Thus it has been proposed that perhaps the low membrane-cytoskeleton adhesion in neurons is related to the unique actin cytoskeletal structures found in axons[276].

7.4.1.2 Membrane tension values and Piezo gating

In agreement with literature values for neuronal cells, we measured low trap forces for tethers pulled from RGCs: F≅15 pN (compare, for example ~32 pN and ~63 pN measured in astrocytes and microglia, respectively[257]). This is similar to values obtained by Pontes et al.[257], and even lower values have been measured in chick neurons[255].

One might ask if, based on literature measurements, one would expect Piezo1 to be activated solely by T at these values. While we did not attempt to decouple tension from bending rigidity, Pontes and colleagues used electron microscopy to measure tether radii in OT measurements of mammalian neurons, and calculated an value of T = 1.6x 10^{-5} N/m[257]. Lewis and Grandl[249] have calculated current vs. tension curves for Piezo1 activation and found that Piezo1 activation was fit to a Boltzman distribution with tension

values at half maximal activation around 1.4 x 10^{-3} N/m. Similar values for the tension values needed for Piezo1 activation were estimated in by Cox and colleagues[164]. With the caveat that these values were obtained in patch-clamp measurements, in which Piezo1 might not behave entirely as it does in intact membranes (Section 1.3.2.1), this is a significantly higher tension value than that which we have measured. This apparent mismatch in tension values suggests that perhaps the functional gating of Piezo1 may not proceed via large scale changes in membrane tension.

While studies of Piezo1 gating have focused on the role of membrane tension, recent results connect endogenous Piezo1 activity to traction forces generated at adhesion sites[175]. In *Xenopus* RGCs, ICC indicates that Piezo1 is enriched in the axon shaft (Eva Pillai, personal communication), where one would not expect significant numbers of force generating adhesions[277]. Thus it doubtful that endogenous Piezo1 activity is regulated by this mechanism in axon shafts, though of course it may be the case in growth cones.

Finally, membrane tension is often assumed to be a global parameter that quickly equilibrates across the surface of a structure[180]. A recent publication suggests that, contrary to this view model of a cell membrane as 2D fluid, tension in fact may not propagate long distances through biological membranes[186]. In this study, local elevations in membrane tension, created by pulling out membrane tethers, resulted in only a localized influx of calcium, indicating localized activation of MSCs[186]. It is interesting to speculate that in cells such as neurons where T and γ are both very low, membrane tension and the pattern of MSC activation in response to stimuli might be different. For example, low membrane-cytoskeletal adhesion could facilitate tension propagation through the membrane in these cells.

7.4.1.3 FliptR experiments

Optical tweezers experiments have limited ability to probe spatial and temporal variations in tension. Together with Ryan Greenhalgh, I began exploring the use of the FliptR membrane tension probe to detect the scale and frequency of localized membrane tension fluctuations in RGCs. It should be noted that FliptR measures a different and complementary parameter to that observed using optical tweezers: the FliptR probe is a small molecule that intercalates among lipids and is sensitive to changes in lipid packing[185]. Therefore its read out is more closely related to T_m (i.e. exclusive of any cytoskeletal contribution (γ)). In future experiments with this probe, we hope to begin to

understand the magnitude and frequency of tension fluctuations in RGC membranes, in order to gauge how such fluctuations might contribute to Piezo1 gating. As Sema3A induces large scale membrane restructuring, it would also be interesting to observe tension changes that transiently occur upon Sema3A stimulation: one interesting hypothesis I have not touched on here is that Sema3A might itself activate growth cone Piezo1.

7.5 Other candidate mechanosensitive elements

While I have focused on Piezo1, there are many other pathways and mechanisms that might contribute to the mechanosensitivity of the Sema3A response, some of which will be discussed in the following section.

7.5.1 Candidates in the Sema3A receptor complex

One possibility is that the receptor complexes that receive the Sema3A signal are themselves mechanosensitive.

The minimal Sema3A receptor complex comprises two copies each of PlexinA1 and Npn1 (See Section 1.1.4); however, this receptor complex can include other components, such as Ig-superfamily cell adhesion molecule L1 CAM[76,77], which is strongly expressed in the visual system of the embryonic frog[278]. L1 is a homophilic cell-cell adhesion molecule, though it also heterophilically binds β-integrins via an RGD sequence, and ECM components such as chondroitin sulfate proteoglycans (CSPGs). L1 can induce massive restructuring of the actin cytoskeleton[279,280]. Moreover, fasciculation of RGC axons growing on a laminin substrate proceeds, at least in part, through the activity of L1[281].

L1 binds Npn1 in both trans and cis: that is, L1 present in the cell membrane can form an integral part of the Sema3A receptor complex, but L1 present on other cells or added in the media can also bind Npn1 (in fact addition of soluble L1 can convert a repulsive Sema3A response to an attractive one, again via modulation of cGMP levels) [76,77,282,283].

L1's ability to modulate adhesion, especially via cis-interactions with integrin, suggests that perhaps these molecules could directly convey mechanosensitivity to the Sema3A receptor complex.

With this in mind, it is interesting to consider that on soft substrates, axons are less fasciculated than on stiff substrates (Figure 1.8). This implies that more axons are likely

adhered to laminin on soft 100 Pa substrates, and more to L1 or other neural cell adhesion molecules on the 1 kPa substrates. Given the importance of cell adhesion in controlling intracellular cyclic nucleotide levels and guidance cue responses, this difference could prove instructive in controlling Sema3A responses. Experiments examining isolated axons on different substrates could potentially disentangle the role of fasciculation from that of stiffness.

7.5.2 Candidates in the Sema3A signalling cascade

Sema3A signalling converges on growth cone point contacts (the slightly more delicate neuronal equivalent of focal adhesions), thus its activity relies on the fundamental equilibria established among traction forces, actomyosin treadmilling, and substrate properties[99,284]. Sema3A is also known to regulate important mechanosensitive point contact proteins, for example, in non-neuronal cells it was found that Sema3A alters FAK phosphorylation in manner dependent on adhesion conditions[285]. Feedback from point contact proteins, or simply changes in the structure of the point contacts on which Sema3A signalling acts, could confer mechanosensitivity on the Sema3A response. Further experiments, including, for example, more detailed imaging of point contact turnover, would be needed to determine how strongly point contact dynamics and composition vary between 100 Pa and 1 kPa substrates.

Endo and exocytosis are also critical for guidance cue responses (Section 1.1.4.2). Endo and exocytosis are mechanically regulated parameters that are likely involved in biomechanical feedback loops for the regulation of growth and membrane tension: in particular, exocytosis decreases membrane tension and is facilitated by high membrane tension, whereas endocytosis increases membrane tension and is facilitated by low membrane tension[180,243,286,287]. Therefore, changes in membrane properties as a function of substrate stiffness – or, given that bulk membrane tension does not seem highly variable across cell types, changes in the rates of endo and exocytosis needed to maintain a setpoint of membrane tension – could well influence the Sema3A response. For example changes in the speed of endocytosis could alter the time-course of collapse. Measuring the rates of endo and exocytosis in neurons on soft and stiff substrates, both basally, and in response to Sema3A stimulation would therefore be informative.

Finally, TRPC5, an ion channel that can be activated by mechanical stimuli[288] has been implicated downstream of Sema3A[96]. Modulation of TRPC5 activity by mechanical stimuli might alter the Sema3A response.

7.6 Final Conclusions and outlook

In this thesis I have shown that a simple change in substrate stiffness, within the physiological range of stiffnesses that are encountered in the developing brain, strongly alters the response of *Xenopus* RGCs to Sema3A.

Changes in substrate stiffness modulated the levels of cGMP and calcium dynamics, two critical second messengers which function as master regulators in signalling cascades downstream of numerous axon guidance cues. Altered growth cone cyclic nucleotide levels would be expected to have a broad influence on many different axon guidance cues. Given the highly heterogeneous and dynamic nature of substrate stiffness in developing tissues, this may be a more general mechanism by which axon growth and guidance is regulated in developing tissue. These results and their potential relation to the known Sema3A signalling cascade are shown in Figure 7.2.

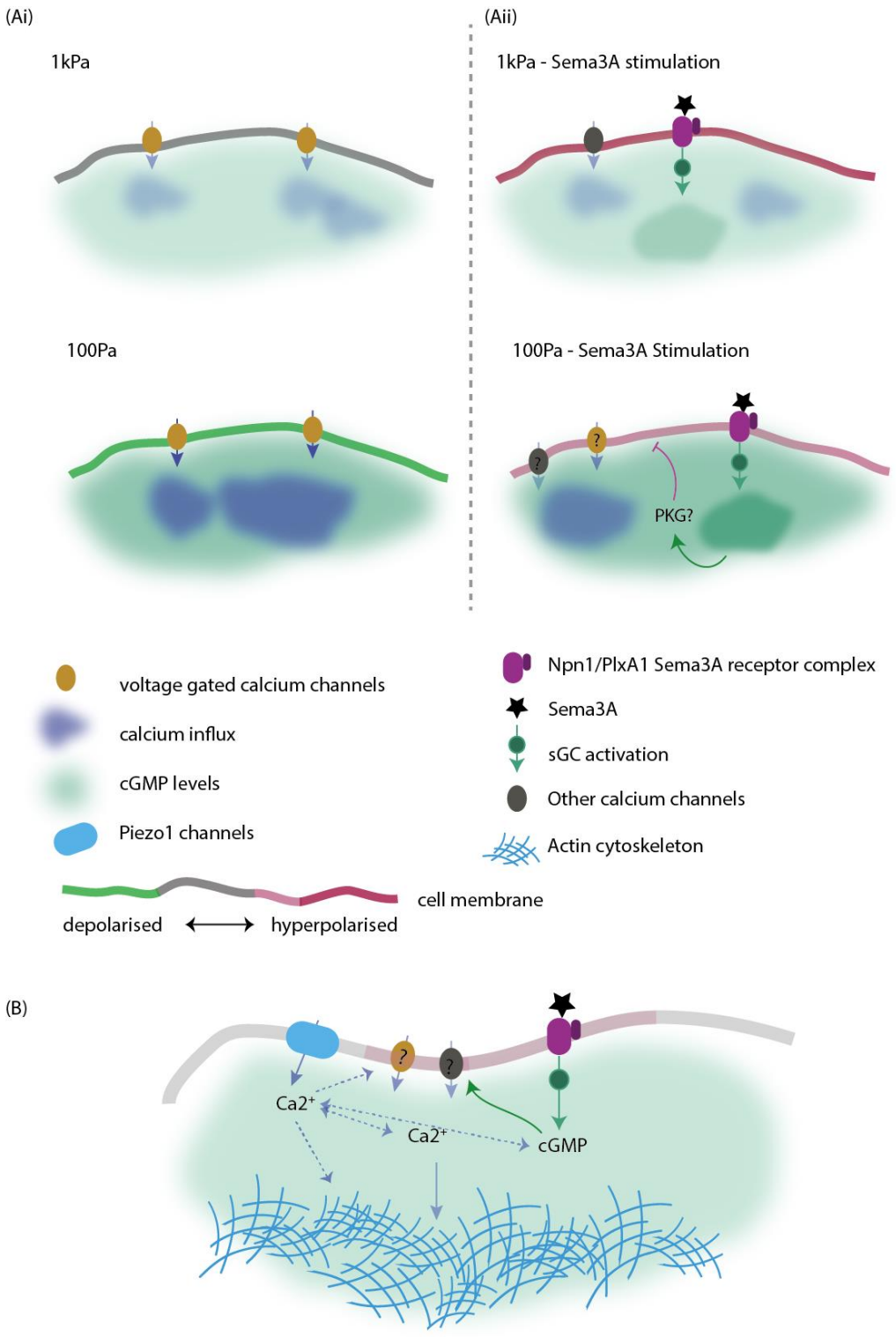

Figure 7.2: Summary of results

Figure 7.2: (continued)

This diagram describes my findings regarding the modulation of growth cone biochemistry on substrates of different stiffness (Ai), and speculates on how they may influence the Sema3A response to induce the observed reduction in the collapse response on soft substrates (Aii), and finally how Piezo1 channels may participate in the regulation of growth cone morphology and pathfinding (B). The cartoons depict a region of growth cone membrane.

(Ai) (My data): in growth cones on soft substrates (bottom), cGMP levels are elevated as compared to on stiff substrates (top). This could proceed, for example, via activation of guanylyl cyclases or suppression of phosphodiesterase activity on soft substrates, or the reverse on stiff substrates. Membrane potential is also more depolarized on soft substrates, possibly due to the cGMP elevation. There is increased calcium transient activity, possibly due to the more depolarized membrane facilitating voltage gated calcium channel opening.

(Aii) Application of my results to known Sema3A signalling modalities[48,81]): under highly repulsive conditions on stiff substrates (top), Sema3A induces an increase in cGMP, which probably proceeds via activation of the soluble guanylyl cyclase (sGC). This triggers membrane hyperpolarization (probably via chloride channels). Calcium influx follows, possibly via cGMP-gated cyclic nucleotide gated ion channels. On soft substrates (bottom) Sema3A induces an increase in intracellular cGMP; combined with the already higher basal cGMP, cGMP levels may reach a sufficient concentration to begin to activate protein kinase G. As PKG tends to depolarize membranes, this possibly attenuates the membrane hyperpolarization induced by a repulsive Sema3A stimulus (pink arrow). Combined with the basal level of membrane depolarization on soft substrates, this results in a less hyperpolarized membrane. Calcium influx follows. Perhaps the less hyperpolarized membrane enables calcium entry through some voltage gated calcium channels, contributing to a higher calcium influx and a less repulsive Sema3A response.

(C) Possible involvement of Piezo1 in RGC outgrowth and growth cone responses. My data support the hypothesis that Piezo1 is involved in the production of growth restricting calcium transients, and, given the robust differences in growth behaviour between axons grown on soft and stiff substrates, this suggests that Piezo1's activity may vary with substrate stiffness; however, I have yet to confirm this experimentally. If Piezo1 activity is indeed regulated by substrate stiffness, Piezo1 signalling could influence the Sema3A signalling cascade by a variety of mechanisms. The involvement of Piezo1 in growth regulation suggests that its signalling cascade converges upon the cytoskeleton, where it could support or oppose Sema3A induced collapse via regulation of actin turnover rates or modulation of adhesion complexes. Additionally, calcium influx through Piezo1 could contribute to membrane depolarization, facilitating activation of voltage gated calcium channels. Finally, some evidence from studies of Piezo1's role in the vasculature suggest that it may influence cyclic nucleotide levels[162,289]. Should such pathways be active in neurons, Piezo1 could also influence Sema3A signalling by influencing the levels of growth cone cGMP.

These results have important implications for our understanding how growth cones 'read' and 'process' complex guidance information *in vivo*. Classically, much of the characterisation of axon guidance cues has been conducted using *in vitro* assays which reduce the complex and chaotic *in vivo* environment to a small set of homogeneous and well controlled stimuli. The adhesion context that a growth cone encounters has for some time now been appreciated as a critical regulator of growth cone responses to chemical guidance cues, and my results indicate that mechanics is another such regulator.

Ultimately, these *in vitro* assays must be used to make predictions about *in vivo* growth behaviour and responses of growth cones. To be able to understand growth cone behaviour sufficiently to predict axonal trajectories in a given environment would require processing immense amounts of data; and computer modelling approaches offer a promising option to parse the cacophony of different *in vivo* stimuli.

Axons' demonstrate an uncanny ability to identify precise trajectories inside complex tissues, and to prevail towards the correct target even in the case of severe perturbations. We are still a long ways away from being able to fully explain this remarkable process. The importance of chemical cues cannot be disputed, but questions remain about the ability of biological systems to generate sufficiently stable and precise gradients to result in the exacting neuronal trajectories observed. Moreover, considering chemistry in the absence of the physical environment deprives neurons of a rich and important source of information about their environment. A modulatory role for mechanosensory axon guidance via substrate stiffness (and/or adhesion) could be the missing link for patterning the brain.

-

8 REFERENCES

1. Engle, E. C. Human genetic disorders of axon guidance. *Cold Spring Harb Perspect Biol* **2**, a001784 (2010).
2. Van Battum, E. Y., Brignani, S. & Pasterkamp, R. J. Axon guidance proteins in neurological disorders. *The Lancet Neurology* **14**, 532–546 (2015).
3. Cajal, S. R. y. À quelle époque apparaissent les expansions des cellules nerveuses de la moëlle épiniè du poulet? *Anatomomischer Anzeiger* **21–22**, 609–639 (1890).
4. Tamariz, E. & Varela-Echavarría, A. The discovery of the growth cone and its influence on the study of axon guidance. *Front. Neuroanat.* **9**, (2015).
5. Harrison, R. G. The reaction of embryonic cells to solid structures. *Journal of Experimental Zoology* **17**, 521–544 (1914).
6. Luarte, A., Cornejo, V. H., Bertin, F., Gallardo, J. & Couve, A. The axonal endoplasmic reticulum: one organelle—many functions in development, maintenance, and plasticity. *Developmental Neurobiology* **78**, 181–208 (2018).
7. Dailey, M. E. & Bridgman, P. C. Structure and organization of membrane organelles along distal microtubule segments in growth cones. *Journal of Neuroscience Research* **30**, 242–258 (1991).
8. Shigeoka, T. *et al.* Dynamic axonal translation in developing and mature visual circuits. *Cell* **166**, 181–192 (2016).
9. Cagnetta, R., Frese, C. K., Shigeoka, T., Krijgsveld, J. & Holt, C. E. Rapid cue-specific remodeling of the nascent axonal proteome. *Neuron* **99**, 29-46.e4 (2018).
10. Dent, E. W., Gupton, S. L. & Gertler, F. B. The growth cone cytoskeleton in axon outgrowth and guidance. *Cold Spring Harb Perspect Biol* **3**, a001800 (2011).
11. Dent, E. W. & Gertler, F. B. Cytoskeletal dynamics and transport in growth cone motility and axon guidance. *Neuron* **40**, 209–227 (2003).

12. Geraldo, S. & Gordon-Weeks, P. R. Cytoskeletal dynamics in growth-cone steering. *J Cell Sci* **122**, 3595–3604 (2009).

13. Papandréou, M.-J. & Leterrier, C. The functional architecture of axonal actin. *Molecular and Cellular Neuroscience* **91**, 151–159 (2018).

14. Bridgman, P. C. & Dailey, M. E. The organization of myosin and actin in rapid frozen nerve growth cones. *J Cell Biol* **108**, 95–109 (1989).

15. Leterrier, C., Dubey, P. & Roy, S. The nano-architecture of the axonal cytoskeleton. *Nature Reviews Neuroscience* **18**, 713–726 (2017).

16. Kapitein, L. C. & Hoogenraad, C. C. Which way to go? Cytoskeletal organization and polarized transport in neurons. *Molecular and Cellular Neuroscience* **46**, 9–20 (2011).

17. Letourneau, P. C. Differences in the organization of actin in the growth cones compared with the neurites of cultured neurons from chick embryos. *The Journal of Cell Biology* **97**, 963–973 (1983).

18. Medeiros, N. A., Burnette, D. T. & Forscher, P. Myosin II functions in actin-bundle turnover in neuronal growth cones. *Nat Cell Biol* **8**, 216–226 (2006).

19. Schaefer, A. W., Kabir, N. & Forscher, P. Filopodia and actin arcs guide the assembly and transport of two populations of microtubules with unique dynamic parameters in neuronal growth cones. *The Journal of Cell Biology* **158**, 139–152 (2002).

20. Xiong, Y., Lee, A. C., Suter, D. M. & Lee, G. U. Topography and nanomechanics of live neuronal growth cones analyzed by atomic force microscopy. *Biophysical Journal* **96**, 5060–5072 (2009).

21. Korobova, F. & Svitkina, T. Arp2/3 complex is important for filopodia formation, growth cone motility, and neuritogenesis in neuronal cells. *MBoC* **19**, 1561–1574 (2008).

22. Goldberg, D. J., Foley, M. S., Tang, D. & Grabham, P. W. Recruitment of the Arp2/3 complex and Mena for the stimulation of actin polymerization in growth cones by nerve growth factor. *Journal of Neuroscience Research* **60**, 458–467 (2000).

23. Vignjevic, D. *et al.* Role of fascin in filopodial protrusion. *J Cell Biol* **174**, 863–875 (2006).

24. Dent, E. W. & Kalil, K. Axon branching requires interactions between dynamic microtubules and actin filaments. *J. Neurosci.* **21**, 9757–9769 (2001).

25. Lin, C. H., Espreafico, E. M., Mooseker, M. S. & Forscher, P. Myosin drives retrograde F-actin flow in neuronal growth cones. *The Biological Bulletin* **192**, 183–185 (1997).

26. Craig, E. M., Van Goor, D., Forscher, P. & Mogilner, A. Membrane tension, myosin force, and actin turnover maintain actin treadmill in the nerve growth cone. *Biophysical Journal* **102**, 1503–1513 (2012).

27. Myers, J. P., Santiago-Medina, M. & Gomez, T. M. Regulation of axonal outgrowth and pathfinding by integrin–ecm interactions. *Developmental Neurobiology* **71**, 901–923 (2011).

28. Betz, T., Koch, D., Lu, Y.-B., Franze, K. & Käs, J. Growth cones as soft and weak force generators. *Proceedings of the National Academy of Sciences* **108**, 13420–13425

29. Chan, C. E. & Odde, D. J. Traction dynamics of filopodia on compliant substrates. *Science* **322**, 1687–1691 (2008).

30. Tanaka, E., Ho, T. & Kirschner, M. W. The role of microtubule dynamics in growth cone motility and axonal growth. *The Journal of Cell Biology* **128**, 139–155 (1995).

31. Marsh, L. & Letourneau, P. C. Growth of neurites without filopodial or lamellipodial activity in the presence of cytochalasin B. *The Journal of Cell Biology* **99**, 2041–2047 (1984).

32. Holt, C. E. A single-cell analysis of early retinal ganglion cell differentiation in Xenopus: from soma to axon tip. *J. Neurosci.* **9**, 3123–3145 (1989).

33. Roberts, A. & Taylor, J. S. H. A scanning electron microscope study of the development of a peripheral sensory neurite network. *Development* **69**, 237–250 (1982).

34. Brittis, P. A. & Silver, J. Multiple factors govern intraretinal axon guidance: a time-lapse study. *Molecular and Cellular Neuroscience* **6**, 413–432 (1995).

35. Huber, A. B., Kolodkin, A. L., Ginty, D. D. & Cloutier, J.-F. Signaling at the growth cone: ligand-receptor complexes and the control of axon growth and guidance. *http://dx.doi.org/10.1146/annurev.neuro.26.010302.081139* **26**, 509–563 (2003).

36. Tessier-Lavigne, M. & Goodman, C. S. The molecular biology of axon guidance. *Science* **274**, 1123–1133 (1996).

37. Erskine, L. & Herrera, E. The retinal ganglion cell axon's journey: Insights into molecular mechanisms of axon guidance. *Developmental Biology* **308**, 1–14 (2007).

38. O'Donnell, M., Chance, R. K. & Bashaw, G. J. Axon growth and guidance: receptor regulation and signal Transduction. *Annual Review of Neuroscience* **32**, 383–412 (2009).

39. Trousse, F., Martí, E., Gruss, P., Torres, M. & Bovolenta, P. Control of retinal ganglion cell axon growth: a new role for Sonic hedgehog. *Development* **128**, 3927–3936 (2001).

40. McFarlane, S., McNeill, L. & Holt, C. E. FGF signaling and target recognition in the developing xenopus visual system. *Neuron* **15**, 1017–1028 (1995).

41. Stone, K. E. & Sakaguchi, D. S. Perturbation of the developing Xenopus retinotectal projection following injections of antibodies against β1Integrin receptors and N-cadherin. *Developmental Biology* **180**, 297–310 (1996).

42. Nishiyama, M. *et al.* Cyclic AMP/GMP-dependent modulation of Ca2+ channels sets the polarity of nerve growth-cone turning. *Nature* **423**, 990–995 (2003).

43. Song, H., Ming, G. & Poo, M. cAMP-induced switching in turning direction of nerve growth cones. *Nature* **388**, 275 (1997).

44. Henley, J. R., Huang, K., Wang, D. & Poo, M. Calcium mediates bidirectional growth cone turning induced by myelin-associated glycoprotein. *Neuron* **44**, 909–916 (2004).

45. Hong, K., Nishiyama, M., Henley, J., Tessier-Lavigne, M. & Poo, M. Calcium signalling in the guidance of nerve growth by netrin-1. *Nature* **403**, 93–98 (2000).

46. Zheng, J. Q. Turning of nerve growth cones induced by localized increases in intracellular calcium ions. *Nature* **403**, 89–93 (2000).

47. Bashaw, G. J. & Klein, R. Signaling from Axon Guidance Receptors. *Cold Spring Harb Perspect Biol* **2**, a001941 (2010).

48. Nishiyama, M., von Schimmelmann, M. J., Togashi, K., Findley, W. M. & Hong, K. Membrane potential shifts caused by diffusible guidance signals direct growth-cone turning. *Nat Neurosci* **11**, 762–771 (2008).

49. Wang, G. X. & Poo, M. Requirement of TRPC channels in netrin-1-induced chemotropic turning of nerve growth cones. *Nature* **434**, 898–904 (2005).

50. Akiyama, H., Fukuda, T., Tojima, T., Nikolaev, V. O. & Kamiguchi, H. Cyclic nucleotide control of microtubule dynamics for axon guidance. *J. Neurosci.* **36**, 5636–5649 (2016).

51. Jurney, W. M., Gallo, G., Letourneau, P. C. & McLoon, S. C. Rac1-mediated endocytosis during ephrin-A2- and semaphorin 3A-Induced growth cone collapse. *J. Neurosci.* **22**, 6019–6028 (2002).

52. Castellani, V., Falk, J. & Rougon, G. Semaphorin3A-induced receptor endocytosis during axon guidance responses is mediated by L1 CAM. *Molecular and Cellular Neuroscience* **26**, 89–100 (2004).

53. Fournier, A. E. *et al.* Semaphorin3a enhances endocytosis at sites of receptor–F-actin colocalization during growth cone collapse. *The Journal of Cell Biology* **149**, 411–422 (2000).

54. Tojima, T., Itofusa, R. & Kamiguchi, H. asymmetric clathrin-mediated endocytosis drives repulsive growth cone guidance. *Neuron* **66**, 370–377 (2010).

55. Hall, A. & Lalli, G. Rho and Ras GTPases in axon growth, guidance, and branching. *Cold Spring Harb Perspect Biol* **2**, a001818 (2010).

56. Wu, K. Y. *et al.* Local translation of RhoA regulates growth cone collapse. *Nature* **436**, 1020–1024 (2005).

57. Iseppon, F., Napolitano, L. M. R., Torre, V. & Cojoc, D. Cdc42 and RhoA reveal different spatio-temporal dynamics upon local stimulation with Semaphorin-3A. *Frontiers in Cellular Neuroscience* (2015). doi:10.3389/fn-cel2015.00333

58. Kahn, O. I. & Baas, P. W. Microtubules and growth cones: motors drive the turn. *Trends in Neurosciences* **39**, 433–440 (2016).

59. Buck, K. B. & Zheng, J. Q. Growth cone turning induced by direct local modification of microtubule dynamics. *J. Neurosci.* **22**, 9358–9367 (2002).

60. Tojima, T. *et al.* Attractive axon guidance involves asymmetric membrane transport and exocytosis in the growth cone. *Nat Neurosci* **10**, 58–66 (2007).

61. Zivraj, K. H. *et al.* Subcellular profiling reveals distinct and developmentally regulated repertoire of growth cone mRNAs. *J. Neurosci.* **30**, 15464–15478 (2010).

62. Giuditta, A., Kaplan, B. B., Minnen, J. van, Alvarez, J. & Koenig, E. Axonal and presynaptic protein synthesis: new insights into the biology of the neuron. *Trends in Neurosciences* **25**, 400–404 (2002).

63. Campbell, D. S. & Holt, C. E. Chemotropic responses of retinal growth cones mediated by rapid local protein synthesis and degradation. *Neuron* **32**, 1013–1026 (2001).

64. Leung, K. M. *et al.* Asymmetrical β-actin mRNA translation in growth cones mediates attractive turning to netrin-1. *Nature Neuroscience* **9**, 1247–1256 (2006).

65. Gherardi, E., Love, C. A., Esnouf, R. M. & Jones, E. Y. The sema domain. *Current Opinion in Structural Biology* **14**, 669–678 (2004).

66. Luo, Y., Raible, D. & Raper, J. A. Collapsin: A protein in brain that induces the collapse and paralysis of neuronal growth cones. *Cell* **75**, 217–227 (1993).

67. Kolodkin, A. L. *et al.* Fasciclin IV: Sequence, expression, and function during growth cone guidance in the grasshopper embryo. *Neuron* **9**, 831–845 (1992).

68. Alto, L. T. & Terman, J. R. Semaphorins and their signaling mechanisms. in *Semaphorin Signaling: Methods and Protocols* (ed. Terman, J. R.) 1–25 (Springer New York, 2017). doi:10.1007/978-1-4939-6448-2_1

69. Fan, J. & Raper, J. A. Localized collapsing cues can steer growth cones without inducing their full collapse. *Neuron* **14**, 263–274 (1995).

70. Takahashi, T. *et al.* Plexin-neuropilin-1 complexes Form functional semaphorin-3A receptors. *Cell* **99**, 59–69 (1999).

71. Janssen, B. J. C. *et al.* Neuropilins lock secreted semaphorins onto plexins in a ternary signaling complex. *Nature Structural & Molecular Biology* **19**, 1293–1299 (2012).

72. Koppel, A. M. & Raper, J. A. Collapsin-1 covalently dimerizes, and dimerization is necessary for collapsing activity. *J. Biol. Chem.* **273**, 15708–15713 (1998).

73. Nakamura, F., Tanaka, M., Takahashi, T., Kalb, R. G. & Strittmatter, S. M. Neuropilin-1 extracellular domains mediate semaphorin D/III-induced growth cone collapse. *Neuron* **21**, 1093–1100 (1998).

74. Siebold, C. & Jones, E. Y. Structural insights into semaphorins and their receptors. *Seminars in Cell & Developmental Biology* **24**, 139–145 (2013).

75. Tamagnone, L. *et al.* Plexins are a large family of receptors for transmembrane, secreted, and GPI-anchored semaphorins in vertebrates. *Cell* **99**, 71–80 (1999).

76. Castellani, V., Chédotal, A., Schachner, M., Faivre-Sarrailh, C. & Rougon, G. Analysis of the L1-deficient mouse phenotype reveals cross-talk between Sema3A and L1 signaling pathways in axonal guidance. *Neuron* **27**, 237–249 (2000).

77. Castellani, V., Angelis, E. D., Kenwrick, S. & Rougon, G. Cis and trans interactions of L1 with neuropilin-1 control axonal responses to semaphorin 3A. *The EMBO Journal* **21**, 6348–6357 (2002).

78. Harvey, A. R. Receptor complexes for each of the class 3 semaphorins. *Front. Cell. Neurosci.* **6**, (2012).

79. Cioni, J.-M. *et al.* Sema3A signaling controls layer-specific interneuron branching in the cerebellum. *Current Biology* **23**, 850–861 (2013).

80. Polleux, F., Morrow, T. & Ghosh, A. Semaphorin 3A is a chemoattractant for cortical apical dendrites. *Nature* **404**, 567–573 (2000).

81. Togashi, K. *et al.* Cyclic GMP-gated CNG channels function in Sema3A-induced growth cone repulsion. *Neuron* **58**, 694–707 (2008).

82. Guirland, C., Suzuki, S., Kojima, M., Lu, B. & Zheng, J. Q. Lipid rafts mediate chemotropic guidance of nerve growth cones. *Neuron* **42**, 51–62 (2004).

83. Tran, T. S., Kolodkin, A. L. & Bharadwaj, R. Semaphorin regulation of cellular morphology. *Annual Review of Cell and Developmental Biology* **23**, 263–292 (2007).

84. Song, H. *et al.* Conversion of neuronal growth cone responses from repulsion to attraction by cyclic nucleotides. *Science* **281**, 1515–1518 (1998).

85. Dent, E. W., Barnes, A. M., Tang, F. & Kalil, K. Netrin-1 and semaphorin 3A promote or inhibit cortical axon branching, respectively, by reorganization of the cytoskeleton. *J. Neurosci.* **24**, 3002–3012 (2004).

86. Fan, J., Mansfield, S. G., Redmond, T., Gordon-Weeks, P. R. & Raper, J. A. The organization of F-actin and microtubules in growth cones exposed to a brain-derived collapsing factor. *The Journal of Cell Biology* **121**, 867–878 (1993).

87. Püschel, A. W. GTPases in semaphorin signaling. in *Semaphorins: receptor and intracellular signaling mechanisms* (ed. Pasterkamp, R. J.) **600**, 12–23 (Springer New York, 2007).

88. Toyofuku, T. *et al.* FARP2 triggers signals for Sema3A-mediated axonal repulsion. *Nat Neurosci* **8**, 1712–1719 (2005).

89. Jin, Z. & Strittmatter, S. M. Rac1 Mediates Collapsin-1-Induced Growth Cone Collapse. *J. Neurosci.* **17**, 6256–6263 (1997).

90. Rohm, B., Rahim, B., Kleiber, B., Hovatta, I. & Püschel, A. W. The semaphorin 3A receptor may directly regulate the activity of small GTPases. *FEBS Letters* **486**, 68–72 (2000).

91. Kinbara, K., Goldfinger, L. E., Hansen, M., Chou, F.-L. & Ginsberg, M. H. Ras GTPases: integrins' friends or foes? *Nat Rev Mol Cell Biol* **4**, 767–777 (2003).

92. Zanata, S. M., Hovatta, I., Rohm, B. & Püschel, A. W. Antagonistic effects of Rnd1 and RhoD GTPases regulate receptor activity in Semaphorin 3A-induced cytoskeletal collapse. *J. Neurosci.* **22**, 471–477 (2002).

93. Ito, Y., Oinuma, I., Katoh, H., Kaibuchi, K. & Negishi, M. Sema4D/plexin-B1 activates GSK-3β through R-Ras GAP activity, inducing growth cone collapse. *EMBO reports* **7**, 704–709 (2006).

94. Piper, M., Salih, S., Weinl, C., Holt, C. E. & Harris, W. A. Endocytosis-dependent desensitization and protein synthesis–dependent resensitization in retinal growth cone adaptation. *Nature Neuroscience* **8**, 179–186 (2005).

95. Nayal, A., Webb, D. J. & Horwitz, A. F. Talin: an emerging focal point of adhesion dynamics. *Current Opinion in Cell Biology* **16**, 94–98 (2004).

96. Kaczmarek, J. S., Riccio, A. & Clapham, D. E. Calpain cleaves and activates the TRPC5 channel to participate in semaphorin 3A-induced neuronal growth cone collapse. *PNAS* **109**, 7888–7892 (2012).

97. Qin, Q., Liao, G., Baudry, M. & Bi, X. Role of calpain-mediated p53 truncation in semaphorin 3A-induced axonal growth regulation. *Proc. Natl. Acad. Sci. U.S.A.* **107**, 13883–13887 (2010).

98. Chan, K. T., Bennin, D. A. & Huttenlocher, A. Regulation of adhesion dynamics by calpain-mediated proteolysis of focal adhesion kinase (FAK). *J. Biol. Chem.* **285**, 11418–11426 (2010).

99. Kerstein, P. C., Patel, K. M. & Gomez, T. M. Calpain-mediated proteolysis of talin and FAK regulates adhesion dynamics necessary for axon guidance. *J. Neurosci.* **37**, 1568–1580 (2017).

100. Leung, L. C. *et al.* Coupling of NF-protocadherin signaling to axon guidance by cue-induced translation. *Nat Neurosci* **16**, 166–173 (2013).

101. McFarlane, S. & Lom, B. The Xenopus retinal ganglion cell as a model neuron to study the establishment of neuronal connectivity. *Developmental Neurobiology* **72**, 520–536 (2012).

102. Holt, C. E., Bertsch, T. W., Ellis, H. M. & Harris, W. A. Cellular determination in the xenopus retina is independent of lineage and birth date. *Neuron* **1**, 15–26 (1988).

103. Nieuwkoop & Faber. *Normal Table of Xenopus Laevis*. (Garland Publishing Inc, 1994).

104. Nakagawa, S. *et al.* Ephrin-B regulates the ipsilateral routing of retinal axons at the optic chiasm. *Neuron* **25**, 599–610 (2000).

105. Mann, F. & Holt, C. E. Control of retinal growth and axon divergence at the chiasm: lessons from Xenopus. *BioEssays* **23**, 319–326 (2001).

106. Sperry, R. W. Chemoaffinity in the orderly growth of nerve fiber patterns and connections. *PNAS* **50**, 703–710 (1963).

107. Harris, W. A. Local positional cues in the neuroepithelium guide retinal axons in embryonic Xenopus brain. *Nature* **339**, 218 (1989).

108. Harris, W. A. Homing behaviour of axons in the embryonic vertebrate brain. *Nature* **320**, 266–269 (1986).

109. Brittis, P. A., Lemmon, V., Rutishauser, U. & Silver, J. Unique changes of ganglion cell growth cone behavior following cell adhesion molecule perturbations: a time-lapse study of the living retina. *Molecular and Cellular Neuroscience* **6**, 433–449 (1995).

110. Deiner, M. S. *et al.* Netrin-1 and DCC mediate axon guidance locally at the optic disc: loss of function leads to optic nerve hypoplasia. *Neuron* **19**, 575–589 (1997).

111. Erskine, L. *et al.* Retinal ganglion cell axon guidance in the mouse optic chiasm: expression and function of robos and slits. *J. Neurosci.* **20**, 4975–4982 (2000).

112. Hutson, L. D. & Chien, C.-B. Pathfinding and error correction by retinal axons: the role of astray/robo2. *Neuron* **33**, 205–217 (2002).

113. Sakai, J. A. & Halloran, M. C. Semaphorin 3d guides laterality of retinal ganglion cell projections in zebrafish. *Development* **133**, 1035–1044 (2006).

114. Ichijo, H. & Kawabata, I. Roles of the telencephalic cells and their chondroitin sulfate proteoglycans in delimiting an anterior border of the retinal pathway. *J. Neurosci.* **21**, 9304–9314 (2001).

115. Campbell, D. S. *et al.* Semaphorin 3A elicits stage-dependent collapse, turning, and branching in Xenopus retinal growth cones. *J. Neurosci.* **21**, 8538–8547 (2001).

116. Atkinson-Leadbeater, K. *et al.* Dynamic expression of axon guidance cues required for optic tract development is controlled by fibroblast growth factor signaling. *J. Neurosci.* **30**, 685–693 (2010).

117. Mann, F., Ray, S., Harris, W. A. & Holt, C. E. Topographic mapping in dorsoventral axis of the Xenopus retinotectal system depends on signaling through ephrin-B ligands. *Neuron* **35**, 461–473 (2002).

118. Itano, N., Okamoto, S., Zhang, D., Lipton, S. A. & Ruoslahti, E. Cell spreading controls endoplasmic and nuclear calcium: A physical gene regulation pathway from the cell surface to the nucleus. *PNAS* **100**, 5181–5186 (2003).

119. Engler, A. J., Sen, S., Sweeney, H. L. & Discher, D. E. Matrix easticity directs stem cell lineage specification. *Cell* **126**, 677–689 (2006).

120. Nagelkerke, A., Bussink, J., Rowan, A. E. & Span, P. N. The mechanical microenvironment in cancer: How physics affects tumours. *Seminars in Cancer Biology* **35**, 62–70 (2015).

121. Kumar, S. & Weaver, V. M. Mechanics, malignancy, and metastasis: The force journey of a tumor cell. *Cancer Metastasis Rev* **28**, 113–127 (2009).

122. Franze, K. The mechanical control of nervous system development. *Development* **140**, 3069–3077 (2013).

123. Koser, D. E. *et al.* Mechanosensing is critical for axon growth in the developing brain. *Nat Neurosci* **19**, 1592–1598 (2016).

124. Engstrom, T. A., Pogoda, K., Cruz, K., Janmey, P. A. & Schwarz, J. M. Compression stiffening in biological tissues: On the possibility of classic elasticity origins. *Physical Review E* **99**, (2019).

125. Gurmessa, B., Ricketts, S. & Robertson-Anderson, R. M. Nonlinear actin deformations lead to network stiffening, yielding, and nonuniform stress propagation. *Biophysical Journal* **113**, 1540–1550 (2017).

126. Chatelin, S., Constantinesco, A. & Willinger, R. Fifty years of brain tissue mechanical testing: From in vitro to in vivo investigations. *Biorheology* **47**, 255–276 (2010).

127. Christ, A. F. *et al.* Mechanical difference between white and gray matter in the rat cerebellum measured by scanning force microscopy. *Journal of Biomechanics* **43**, 2986–2992 (2010).

128. Jansen, L. E., Birch, N. P., Schiffman, J. D., Crosby, A. J. & Peyton, S. R. Mechanics of intact bone marrow. *J Mech Behav Biomed Mater* **50**, 299–307 (2015).

129. Schöne, M., Schulz, R. M., Tzschätzsch, H., Varga, P. & Raum, K. Ultrasound palpation for fast in-situ quantification of articular cartilage stiffness, thickness and relaxation capacity. *Biomech Model Mechanobiol* **16**, 1171–1185 (2017).

130. Allison, D. P., Mortensen, N. P., Sullivan, C. J. & Doktycz, M. J. Atomic force microscopy of biological samples. *Wiley Interdisciplinary Reviews: Nanomedicine and Nanobiotechnology* **2**, 618–634 (2010).

131. Binnig, G., Quate, C. F. & Gerber, Ch. Atomic force microscope. *Phys. Rev. Lett.* **56**, 930–933 (1986).

132. Thompson, A. J. *et al.* Rapid changes in tissue mechanics regulate cell behaviour in the developing embryonic brain. *eLife* **8**, e39356 (2019).

133. Kleinman, H. K. & Martin, G. R. Matrigel: Basement membrane matrix with biological activity. *Seminars in Cancer Biology* **15**, 378–386 (2005).

134. Benya, P. D. & Shaffer, J. D. Dedifferentiated chondrocytes reexpress the differentiated collagen phenotype when cultured in agarose gels. *Cell* **30**, 215–224 (1982).

135. Schnaar, R. L., Weigel, P. H., Kuhlenschmidt, M. S., Lee, Y. C. & Roseman, S. Adhesion of chicken hepatocytes to polyacrylamide gels derivatized with N-Acetylglycosamine. *The Journal of Biological Chemistry* **253**, 7940–7951 (1978).

136. Georges, P. C. & Janmey, P. A. Cell type-specific response to growth on soft materials. *Journal of Applied Physiology* **98**, 1547–1553 (2005).

137. Dembo, M. & Wang, Y.-L. Stresses at the cell-to-substrate interface during locomotion of fibroblasts. *Biophysical Journal* **76**, 2307–2316 (1999).

138. Butler, J. P., Tolić-Nørrelykke, I. M., Fabry, B. & Fredberg, J. J. Traction fields, moments, and strain energy that cells exert on their surroundings. *American Journal of Physiology-Cell Physiology* **282**, C595–C605 (2002).

139. Tan, J. L. *et al.* Cells lying on a bed of microneedles: an approach to isolate mechanical force. *Proceedings of the National Academy of Sciences* **100**, 1484–1489 (2003).

140. Bray, D. Axonal growth in response to experimentally applied mechanical tension. *Developmental Biology* **102**, 379–389 (1984).

141. Dai, J., Sheetz, M. P., Wan, X. & Morris, C. E. Membrane tension in swelling and shrinking molluscan neurons. *The Journal of Neuroscience* **18**, 6681–6692 (1998).

142. Franze, K. *et al.* Neurite branch retraction Is caused by a threshold-dependent mechanical impact. *Biophys J* **97**, 1883–1890 (2009).

143. Goult, B. T., Yan, J. & Schwartz, M. A. Talin as a mechanosensitive signaling hub. *J Cell Biol* **217**, 3776–3784 (2018).

144. Rio, A. del *et al.* Stretching single talin rod molecules activates vinculin binding. *Science* **323**, 638–641 (2009).

145. Geiger, B., Spatz, J. P. & Bershadsky, A. D. Environmental sensing through focal adhesions. *Nature Reviews Molecular Cell Biology* **10**, 21–33 (2009).

146. Bershadsky, A. D., Balaban, N. Q. & Geiger, B. Adhesion-dependent cell mechanosensitivity. *Annual Review of Cell and Developmental Biology* **19**, 677–695 (2003).

147. Pelham, R. J. & Wang, Y. Cell locomotion and focal adhesions are regulated by substrate flexibility | PNAS. *Proceedings of the National Academy of Sciences* **94**, 13661–13665 (1997).

148. Yeung, T. *et al.* Effects of substrate stiffness on cell morphology, cytoskeletal structure, and adhesion. *Cell Motility* **60**, 24–34 (2005).

149. Stutchbury, B., Atherton, P., Tsang, R., Wang, D.-Y. & Ballestrem, C. Distinct focal adhesion protein modules control different aspects of mechanotransduction. *J Cell Sci* **130**, 1612–1624 (2017).

150. Zebda, N., Dubrovskyi, O. & Birukov, K. G. Focal adhesion kinase regulation of mechanotransduction and its impact on endothelial cell functions. *Microvasc Res* **83**, 71–81 (2012).

151. Leckband, D. E., le Duc, Q., Wang, N. & de Rooij, J. Mechanotransduction at cadherin-mediated adhesions. *Current Opinion in Cell Biology* **23**, 523–530 (2011).

152. Bazellières, E. *et al.* Control of cell–cell forces and collective cell dynamics by the intercellular adhesome. *Nature Cell Biology* **17**, 409–420 (2015).

153. Campinho, P. *et al.* Tension-oriented cell divisions limit anisotropic tissue tension in epithelial spreading during zebrafish epiboly. *Nature Cell Biology* **15**, 1405–1414 (2013).

154. Martinac, B. & Cox, C. D. Mechanosensory transduction: focus on ion channels. in *Reference Module in Life Sciences* (Elsevier, 2017). doi:10.1016/B978-0-12-809633-8.08094-8

155. Ridone, P., Vassalli, M. & Martinac, B. Piezo1 mechanosensitive channels: what are they and why are they important. *Biophys Rev* (2019). doi:10.1007/s12551-019-00584-5

156. Coste, B. *et al.* Piezo1 and Piezo2 Are essential components of distinct mechanically activated cation channels. *Science* **330**, 55–60 (2010).

157. Coste, B. *et al.* Piezo proteins are pore-forming subunits of mechanically activated channels. *Nature* **483**, 176–181 (2012).

158. Ge, J. *et al.* Architecture of the mammalian mechanosensitive Piezo1 channel. *Nature* **527**, 64–69 (2015).

159. Zhao, Q. *et al.* Structure and mechanogating mechanism of the Piezo1 channel. *Nature* **554**, 487–492 (2018).

160. Syeda, R. *et al.* Piezo1 channels Are inherently mechanosensitive. *Cell Reports* **17**, 1739–1746 (2016).

161. Lacroix, J. J., Botello-Smith, W. M. & Luo, Y. Probing the gating mechanism of the mechanosensitive channel Piezo1 with the small molecule Yoda1. *Nature Communications* **9**, 2029 (2018).

162. Li, J. *et al.* Piezo1 integration of vascular architecture with physiological force. *Nature* **515**, 279–282 (2014).

163. Gottlieb, P. A., Bae, C. & Sachs, F. Gating the mechanical channel Piezo1. *Channels* **6**, 282–289 (2012).

164. Cox, C. D. *et al.* Removal of the mechanoprotective influence of the cytoskeleton reveals PIEZO1 is gated by bilayer tension. *Nature Communications* **7**, ncomms10366 (2016).

165. Gaub, B. M. & Müller, D. J. Mechanical stimulation of Piezo1 receptors depends on extracellular matrix proteins and directionality of force. *Nano Lett.* **17**, 2064–2072 (2017).

166. Gudipaty, S. A. *et al.* Mechanical stretch triggers rapid epithelial cell division through Piezo1. *Nature* **543**, 118–121 (2017).

167. Tissue expression of PIEZO1 - Summary - The Human Protein Atlas. Available at: https://www.proteinatlas.org/ENSG00000103335-PIEZO1/tissue. (Accessed: 15th September 2019)

168. Ranade, S. S. *et al.* Piezo1, a mechanically activated ion channel, is required for vascular development in mice. *PNAS* **111**, 10347–10352 (2014).

169. Albuisson, J. *et al.* Dehydrated hereditary stomatocytosis linked to gain-of-function mutations in mechanically activated PIEZO1 ion channels. *Nature Communications* **4**, 1884 (2013).

170. Lukacs, V. *et al.* Impaired PIEZO1 function in patients with a novel autosomal recessive congenital lymphatic dysplasia. *Nature Communications* **6**, 8329 (2015).

171. Nourse, J. L. & Pathak, M. M. How cells channel their stress: Interplay between Piezo1 and the cytoskeleton. *Seminars in Cell & Developmental Biology* **71**, 3–12 (2017).

172. Ridone, P. *et al.* Disruption of membrane cholesterol organization impairs the concerted activity of PIEZO1 channel clusters. *bioRxiv* 604488 (2019). doi:10.1101/604488

173. Qi, Y. *et al.* Membrane stiffening by STOML3 facilitates mechanosensation in sensory neurons. *Nature Communications* **6**, 8512 (2015).

174. Guo, Y. R. & MacKinnon, R. Structure-based membrane dome mechanism for Piezo mechanosensitivity. *eLife Sciences* **6**, e33660 (2017).

175. Ellefsen, K. L. *et al.* Myosin-II mediated traction forces evoke localized Piezo1-dependent Ca 2+ flickers. *Commun Biol* **2**, 1–13 (2019).

176. Syeda, R. *et al.* Chemical activation of the mechanotransduction channel Piezo1. *eLife Sciences* **4**, e07369 (2015).

177. Evans, E. L. *et al.* Yoda1 analogue (Dooku1) which antagonizes Yoda1-evoked activation of Piezo1 and aortic relaxation. *British Journal of Pharmacology* **175**, 1744–1759 (2018).

178. Wang, Y. *et al.* A lever-like transduction pathway for long-distance chemical- and mechano-gating of the mechanosensitive Piezo1 channel. *Nature Communications* **9**, 1300 (2018).

179. Coster, H. G. L. The physics of cell membranes. *Journal of Biological Physics* **29**, 363–399 (2003).

180. Diz-Muñoz, A., Fletcher, D. A. & Weiner, O. D. Use the force: membrane tension as an organizer of cell shape and motility. *Trends in Cell Biology* **23**, 47–53 (2013).

181. Pontes, B., Monzo, P. & Gauthier, N. C. Membrane tension: A challenging but universal physical parameter in cell biology. *Seminars in Cell & Developmental Biology* **71**, 30–41 (2017).

182. Pontes, B. *et al.* Cell cytoskeleton and tether extraction. *Biophysical Journal* **101**, 43–52 (2011).

183. Nussenzveig, H. M. Cell membrane biophysics with optical tweezers. *Eur Biophys J* **47**, 499–514 (2018).

184. Dai, J. & Sheetz, M. P. Membrane tether formation from blebbing cells. *Biophysical Journal* **77**, 3363–3370 (1999).

185. Colom, A. *et al.* A fluorescent membrane tension probe. *Nature Chemistry* **10**, 1118 (2018).

186. Shi, Z., Graber, Z. T., Baumgart, T., Stone, H. A. & Cohen, A. E. Cell membranes resist flow. *Cell* **175**, 1769-1779.e13 (2018).

187. Falk, J. *et al.* Electroporation of cDNA/Morpholinos to targeted areas of embryonic CNS in Xenopus. *BMC Developmental Biology* **7**, 107 (2007).

188. Warren, S. C. *et al.* Rapid global fitting of large fluorescence lifetime imaging microscopy datasets. *PLOS ONE* **8**, e70687 (2013).

189. Gosse, C. & Croquette, V. Magnetic tweezers: micromanipulation and force measurement at the molecular level. *Biophysical Journal* **82**, 3314–3329 (2002).

190. Ballerstadt, R., Evans, C., McNichols, R. & Gowda, A. Concanavalin A for in vivo glucose sensing: A biotoxicity review. *Biosensors and Bioelectronics* **22**, 275–284 (2006).

191. Ferreira, T. A. *et al.* Neuronal morphometry directly from bitmap images. *Nature Methods* **11**, 982–984 (2014).

192. Janmey, P. A. & Miller, R. T. Mechanisms of mechanical signaling in development and disease. *J. Cell. Sci.* **124**, 9–18 (2011).

193. Cox, E. C., Müller, B. & Bonhoeffer, F. Axonal guidance in the chick visual system: Posterior tectal membranes induce collapse of growth cones from the temporal retina. *Neuron* **4**, 31–37 (1990).

194. Raper, J. A. & Kapfhammer, J. R. The enrichment of a neuronal growth cone collapsing activity from embryonic chick brain. *Neuron* **4**, 21–29 (1990).

195. Monschau, B. *et al.* Shared and distinct functions of RAGS and ELF-1 in guiding retinal axons. *The EMBO Journal* **16**, 1258–1267 (1997).

196. Meima, L. *et al.* AL-1-induced growth cone collapse of rat cortical neurons is correlated with REK7 expression and rearrangement of the actin cytoskeleton. *European Journal of Neuroscience* **9**, 177–188 (1997).

197. Koch, D., Rosoff, W. J., Jiang, J., Geller, H. M. & Urbach, J. S. Strength in the periphery: growth cone biomechanics and substrate rigidity response in peripheral and central nervous system neurons. *Biophysical Journal* **102**, 452–460 (2012).

198. Manns, R. P. C., Cook, G. M. W., Holt, C. E. & Keynes, R. J. Differing semaphorin 3A concentrations trigger distinct signaling mechanisms in growth cone collapse. *Journal of Neuroscience* **32**, 8554–8559 (2012).

199. Ming, G. *et al.* cAMP-dependent growth cone guidance by netrin-1. **19**, 1225–1235 (1997).

200. Tessier-Lavigne, M. & Placzek, M. Guidance of developing axons by diffusible chemoattractants. in *Principles of Medical Biology* (eds. Bittar, E. E. & Bittar, N.) **11**, 153–165 (Elsevier, 1998).

201. Pujic, Z., Giacomantonio, C. E., Unni, D., Rosoff, W. J. & Goodhill, G. J. Analysis of the growth cone turning assay for studying axon guidance. *Journal of Neuroscience Methods* **170**, 220–228 (2008).

202. Moshayedi, P. *et al.* Mechanosensitivity of astrocytes on optimized polyacrylamide gels analyzed by quantitative morphometry. *J Phys Condens Matter* **22**, 194114 (2010).

203. Goodhill, G. J. & Urbach, J. S. Theoretical analysis of gradient detection by growth cones. *Journal of Neurobiology* **41**, 230–241 (1999).

204. Isbister, C. M., Mackenzie, P. J., To, K. C. W. & O'Connor, T. P. Gradient steepness influences the pathfinding decisions of neuronal growth cones in vivo. *J. Neurosci.* **23**, 193–202 (2003).

205. Bentley, D. & Toroian-Raymond, A. Disoriented pathfinding by pioneer neurone growth cones deprived of filopodia by cytochalasin treatment. *Nature* **323**, 712–715 (1986).

206. Zheng, J. Q., Wan, J. J. & Poo, M. M. Essential role of filopodia in chemotropic turning of nerve growth cone induced by a glutamate gradient. *J. Neurosci.* **16**, 1140–1149 (1996).

207. Gomez, T. M., Robles, E., Poo, M. & Spitzer, N. C. Filopodial calcium transients promote substrate-dependent growth cone turning. *Science* **291**, 1983–1987 (2001).

208. Model, M. A. Methods for cell volume measurement. *Cytometry Part A* **93**, 281–296 (2018).

209. Perez Gonzalez, N. *et al.* Cell tension and mechanical regulation of cell volume. *MBoC* **29**, 0–0 (2018).

210. Li, H., Pang, F., Shi, Y. & Liu, Z. Cell dynamic morphology classification using deep convolutional neural networks. *Cytometry Part A* **93**, 628–638 (2018).

211. Goodhill, G. J. *et al.* The dynamics of growth cone morphology. *BMC Biology* **13**, 10 (2015).

212. Naoki, H. *et al.* Multi-phasic bi-directional chemotactic responses of the growth cone. *Scientific Reports* **6**, 36256 (2016).

213. Garthwaite, J. *et al.* Potent and selective inhibition of nitric oxide-sensitive guanylyl cyclase by 1H-[1,2,4]oxadiazolo[4,3-a]quinoxalin-1-one. *Mol Pharmacol* **48**, 184–188 (1995).

214. Blackshaw, S. E. & Warner, A. E. Alterations in resting membrane properties during neural plate stages of development of the nervous system. *J Physiol* **255**, 231–247 (1976).

215. Spitzer, N. C. Electrical activity in early neuronal development. *Nature* **444**, 707 (2006).

216. Hille, B. *Ion Channels of Excitable Membranes*. (Sinaeur, 2001).

217. Neher, E. & Sakmann, B. Single-channel currents recorded from membrane of denervated frog muscle fibres. *Nature* **260**, 799–802 (1976).

218. Fairless, R. *et al.* Membrane potential measurements of isolated neurons using a voltage-Sensitive dye. *PLOS ONE* **8**, e58260 (2013).

219. Measuring Membrane Potential using the FLIPR® Membrane Potential Assay Kit on Fluorometric Imaging Plate Reader (FLIPR®) Systems. *Molecular Devices* Available at: https://www.moleculardevices.com/en/assets/app-note/reagents/measuring-

membrane-potential-using-flipr-membrane-potential-assay-kit-on-flipr. (Accessed: 12th February 2019)

220. Zheng, J. Q., Felder, M., Connor, J. A. & Poo, M. Turning of nerve growth cones induced by neurotransmitters. *Nature* **368**, 140–144 (1994).
221. Spitzer, N. C., Lautermilch, N. J., Smith, R. D. & Gomez, T. M. Coding of neuronal differentiation by calcium transients. *Bioessays* **22**, 811–817 (2000).
222. Gu, X. & Spitzer, N. C. Distinct aspects of neuronal differentiation encoded by frequency of spontaneous Ca2+ transients. *Nature* **375**, 784–787 (1995).
223. Gomez, T. M., Snow, D. M. & Letourneau, P. C. Characterization of spontaneous calcium transients in nerve growth cones and their effect on growth cone migration. *Neuron* **14**, 1233–1246 (1995).
224. Gomez, T. M. & Spitzer, N. C. In vivo regulation of axon extension and pathfinding by growth-cone calcium transients. *Nature* **397**, 350 (1999).
225. Dana, H. *et al.* Sensitive red protein calcium indicators for imaging neural activity. *eLife Sciences* **5**, e12727 (2016).
226. Gu, X., Olson, E. C. & Spitzer, N. C. Spontaneous neuronal calcium spikes and waves during early differentiation. *J. Neurosci.* **14**, 6325–6335 (1994).
227. Luo, L. & O'Leary, D. D. M. Axon retraction and degeneration in development and disease. *Annual Review of Neuroscience* **28**, 127–156 (2005).
228. Cheng, S., Geddis, M. S. & Rehder, V. Local calcium changes regulate the length of growth cone filopodia. *Journal of Neurobiology* **50**, 263–275 (2002).
229. Lau, P., Zucker, R. S. & Bentley, D. Induction of filopodia by direct local elevation of intracellular calcium ion concentration. *J Cell Biol* **145**, 1265–1275 (1999).
230. Suchyna, T. M. *et al.* Identification of a peptide toxin from grammostola spatulata spider venom that blocks cation-selective stretch-activated channels. *The Journal of General Physiology* **115**, 583–598 (2000).

231. Bowman, C. L., Gottlieb, P. A., Suchyna, T. M., Murphy, Y. K. & Sachs, F. Mechanosensitive ion channels and the peptide inhibitor GsMTx-4: history, properties, mechanisms and pharmacology. *Toxicon* **49**, 249–270 (2007).

232. Suchyna, T. M. *et al.* Bilayer-dependent inhibition of mechanosensitive channels by neuroactive peptide enantiomers. *Nature* **430**, 235 (2004).

233. Session, A. M. *et al.* Genome evolution in the allotetraploid frog Xenopus laevis. *Nature* **538**, 336–343 (2016).

234. Šmít, D., Fouquet, C., Pincet, F., Zapotocky, M. & Trembleau, A. Axon tension regulates fasciculation/defasciculation through the control of axon shaft zippering. *eLife* **6**, e19907 (2017).

235. Honig, M. G., Petersen, G. G., Rutishauser, U. S. & Camilli, S. J. In vitro studies of growth cone behavior support a role for fasciculation mediated by cell adhesion molecules in

sensory axon guidance during development. *Developmental Biology* **204**, 317–326 (1998).

236. Tsuchiya, M. *et al.* Cell surface flip-flop of phosphatidylserine is critical for PIEZO1-mediated myotube formation. *Nat Commun* **9**, 1–15 (2018).
237. Emery, D. G. & Lucas, J. H. Ultrastructural damage and neuritic beading in cold-stressed spinal neurons with comparisons to NMDA and A23187 toxicity. *Brain Research* **692**, 161–173 (1995).
238. Takeuchi, H. *et al.* Neuritic beading induced by activated microglia is an early feature of neuronal dysfunction toward neuronal death by inhibition of mitochondrial respiration and axonal transport. *J. Biol. Chem.* **280**, 10444–10454 (2005).
239. Pavlidis, M., Stupp, T., Naskar, R., Cengiz, C. & Thanos, S. Retinal ganglion cells resistant to advanced glaucoma: a postmortem study of human retinas with the carbocyanine dye DiI. *Invest. Ophthalmol. Vis. Sci.* **44**, 5196–5205 (2003).
240. Goel, S., Wharton, S. B., Brett, L. P. & Whittle, I. R. Morphological changes and stress responses in neurons in cerebral cortex infiltrated by diffuse astrocytoma. *Neuropathology* **23**, 262–270 (2003).
241. Wang, J. T., Medress, Z. A. & Barres, B. A. Axon degeneration: molecular mechanisms of a self-destruction pathway. *J Cell Biol* **196**, 7–18 (2012).
242. Brustovetsky, T., Bolshakov, A. & Brustovetsky, N. Calpain activation and Na+/Ca2+ exchanger degradation occur downstream of calcium deregulation in hippocampal

neurons exposed to excitotoxic glutamate. *Journal of Neuroscience Research* **88**, 1317–1328 (2010).

243. Gupton, S. L. & Gertler, F. B. Integrin signaling switches the cytoskeletal and exocytic machinery that drives neuritogenesis. *Developmental Cell* **18**, 725–736 (2010).
244. Sabo, S. L. & McAllister, A. K. Mobility and cycling of synaptic protein–containing vesicles in axonal growth cone filopodia. *Nat Neurosci* **6**, 1264–1269 (2003).
245. Kerstein, P. C. *et al.* Mechanosensitive TRPC1 channels promote calpain proteolysis of talin to regulate spinal axon outgrowth. *J. Neurosci.* **33**, 273–285 (2013).
246. Wang, Y.-Y. *et al.* Piezo1 mediates neuron oxygen-glucose deprivation/reoxygenation injury via Ca2+/calpain signaling. *Biochemical and Biophysical Research Communications* **513**, 147–153 (2019).
247. Rosser, B. G., Powers, S. P. & Gores, G. J. Calpain activity increases in hepatocytes following addition of ATP. Demonstration by a novel fluorescent approach. *J. Biol. Chem.* **268**, 23593–23600 (1993).
248. Jacques-Fricke, B. T., Seow, Y., Gottlieb, P. A., Sachs, F. & Gomez, T. M. Ca2+ Influx through mechanosensitive channels inhibits neurite outgrowth in opposition to other

influx pathways and release from intracellular stores. *J. Neurosci.* **26**, 5656–5664 (2006).

249. Lewis, A. H. & Grandl, J. Mechanical sensitivity of Piezo1 ion channels can be tuned by cellular membrane tension. *eLife* **4**,
250. Pathak, M. M. *et al.* Stretch-activated ion channel Piezo1 directs lineage choice in human neural stem cells. *PNAS* **111**, 16148–16153 (2014).
251. Bo, L. & Waugh, R. E. Determination of bilayer membrane bending stiffness by tether formation from giant, thin-walled vesicles. *Biophysical Journal* **55**, 509–517 (1989).
252. Hochmuth, R. M. & Evans, E. A. Extensional flow of erythrocyte membrane from cell body to elastic tether. I. Analysis. *Biophysical Journal* **39**, 71–81 (1982).
253. Sheetz, M. P. & Dai, J. Modulation of membrane dynamics and cell motility by membrane tension. *Trends in Cell Biology* **6**, 85–89 (1996).
254. Dai, J. & Sheetz, M. P. Mechanical properties of neuronal growth cone membranes studied by tether formation with laser optical tweezers. *Biophys. J.* **68**, 988–996 (1995).
255. Hochmuth, F. M., Shao, J. Y., Dai, J. & Sheetz, M. P. Deformation and flow of membrane into tethers extracted from neuronal growth cones. *Biophys J* **70**, 358–369 (1996).
256. Keren, K. Cell motility: the integrating role of the plasma membrane. *Eur Biophys J* **40**, 1013 (2011).
257. Pontes, B. *et al.* Membrane elastic properties and cell function. *PLOS ONE* **8**, e67708 (2013).
258. Datar, A., Bornschlögl, T., Bassereau, P., Prost, J. & Pullarkat, P. A. Dynamics of membrane tethers reveal novel aspects of cytoskeleton-membrane interactions in axons. *Biophysical Journal* **108**, 489–497 (2015).
259. Dai, J. & Sheetz, M. P. Axon membrane flows from the growth cone to the cell body. *Cell* **83**, 693–701 (1995).
260. Bajanca, F. *et al.* In vivo topology converts competition for cell-matrix adhesion into directional migration. *Nature Communications* **10**, 1518 (2019).

261. Goodhill, G. J. Can molecular gradients wire the brain? *Trends in Neurosciences* **39**, 202–211 (2016).

262. Huber, A. B. *et al.* Distinct roles for secreted semaphorin signaling in spinal motor axon guidance. *Neuron* **48**, 949–964 (2005).

263. Hayashi, M. *et al.* Autoregulation of osteocyte Sema3A orchestrates estrogen action and counteracts bone aging. *Cell Metabolism* **29**, 627-637.e5 (2019).

264. Liu, L. *et al.* Semaphorin 3A promotes osteogenic differentiation in human alveolar bone marrow mesenchymal stem cells. *Exp Ther Med* **15**, 3489–3494 (2018).

265. Tang, P., Yin, P., Lv, H., Zhang, L. & Zhang, L. The role of semaphorin 3A in the skeletal system. *CRE* **25**, (2015).

266. Liu, L.-N., Li, X.-M., Ye, D.-Q. & Pan, H.-F. Emerging role of semaphorin-3A in autoimmune diseases. *Inflammopharmacol* **26**, 655–665 (2018).

267. Lepelletier, Y. *et al.* Immunosuppressive role of semaphorin-3A on T cell proliferation is mediated by inhibition of actin cytoskeleton reorganization. *European Journal of Immunology* **36**, 1782–1793 (2006).

268. Liu, X. *et al.* Semaphorin 3A shifts adipose mesenchymal stem cells towards osteogenic phenotype and promotes bone regeneration in vivo. *Stem Cells Int* **2016**, (2016).

269. Levy, F. O. Cardiac PDEs and crosstalk between cAMP and cGMP signalling pathways in the regulation of contractility. *Naunyn-Schmiedeberg's Arch Pharmacol* **386**, 665–670 (2013).

270. Polito, M. *et al.* The NO/cGMP pathway inhibits transient cAMP signals through the activation of PDE2 in striatal neurons. *Front. Cell. Neurosci.* **7**, (2013).

271. Shewan, D., Dwivedy, A., Anderson, R. & Holt, C. E. Age-related changes underlie switch in netrin-1 responsiveness as growth cones advance along visual pathway. *Nature Neuroscience* **5**, 955 (2002).

272. Averaimo, S. *et al.* A plasma membrane microdomain compartmentalizes ephrin-generated cAMP signals to prune developing retinal axon arbors. *Nat Commun* **7**, 12896 (2016).

273. Li, S. *et al.* Intracellular calcium and cyclic nucleotide levels modulate neurite guidance by microtopographical substrate features. *J Biomed Mater Res A* **104**, 2037–2048 (2016).

274. Lewis, B. B. *et al.* Cloning and characterization of voltage-gated calcium channel alpha1 subunits in Xenopus laevis during development. *Developmental Dynamics* **238**, 2891–2902 (2009).

275. Derényi, I., Jülicher, F. & Prost, J. Formation and interaction of membrane tubes. *Phys. Rev. Lett.* **88**, 238101 (2002).

276. Xu, K., Zhong, G. & Zhuang, X. Actin, spectrin, and associated proteins form a periodic cytoskeletal structure in axons. *Science* **339**, 452–456 (2013).

277. Polackwich, R. J., Koch, D., McAllister, R., Geller, H. M. & Urbach, J. S. Traction force and tension fluctuations in growing axons. *Front. Cell. Neurosci.* **9**, (2015).

278. Date, P. *et al.* Visualizing flow in an intact CSF network using optical coherence tomography: implications for human congenital hydrocephalus. *Sci Rep* **9**, 1–15 (2019).

279. Burden-Gulley, S. M., Pendergast, M. & Lemmon, V. The role of cell adhesion molecule L1 in axonal extension, growth cone motility, and signal transduction. *Cell Tissue Res* **290**, 415–422 (1997).

280. Colombo, F. & Meldolesi, J. L1-CAM and N-CAM: from adhesion proteins to pharmacological targets. *Trends in Pharmacological Sciences* **36**, 769–781 (2015).

281. Drazba, J. & Lemmon, V. The role of cell adhesion molecules in neurite outgrowth on Müller cells. *Developmental Biology* **138**, 82–93 (1990).

282. Stoeck, A. *et al.* L1 on ovarian carcinoma cells is a binding partner for Neuropilin-1 on mesothelial cells. *Cancer Letters* **239**, 212–226 (2006).

283. Schmid, R. S. & Maness, P. F. L1 and NCAM adhesion molecules as signaling coreceptors in neuronal migration and process outgrowth. *Current Opinion in Neurobiology* **18**, 245–250 (2008).

284. Woo, S. & Gomez, T. M. Rac1 and RhoA promote neurite outgrowth through formation and stabilization of growth cone point contacts. *J. Neurosci.* **26**, 1418–1428 (2006).

285. Gehler, S., Compere, F. V. & Miller, A. M. Semaphorin 3A increases FAK phosphorylation at focal adhesions to modulate MDA-MB-231 cell migration and spreading on different substratum concentrations. *International Journal of Breast Cancer* (2017). doi:10.1155/2017/9619734

286. Wang, G. *et al.* Biomechanical control of lysosomal secretion via the VAMP7 hub: a tug-of-war between VARP and LRRK1. *iScience* **4**, 127–143 (2018).

287. Sheetz, M. P. Cell control by membrane-cytoskeleton adhesion. *Nat. Rev. Mol. Cell Biol.* **2**, 392–396 (2001).

288. Shen, B. *et al.* Plasma membrane mechanical stress activates TRPC5 channels. *PLOS ONE* **10**, e0122227 (2015).

289. Albarrán-Juárez, J. *et al.* Piezo1 and Gq/G11 promote endothelial inflammation depending on flow pattern and integrin activation. *Journal of Experimental Medicine* **215**, 2655–2672 (2018).

9 APPENDICES

The Appendices contained herein are:

APPENDIX 1.1: Additional statistics pertaining to figures in Chapter 1

APPENDIX 3.1: Additional statistics pertaining to figures in Chapter 3

APPENDIX 4.1: Supplementary figures for Chapter 4

APPENDIX 4.2: Additional statistics pertaining to figures in Chapter 4

APPENDIX 5.1: Supplementary figure for Chapter 5

APPENDIX 5.1: Additional statistics pertaining to figures in Chapter 5

APPENDIX 6.1: Supplementary figure for Chapter 6

The following appendices contain MATLAB scripts. Where functions that were neither my own nor standard MATLAB functions were used, links are provided in the caption preceding the script. Inputs to the function are also described here.

APPENDIX I: Script used for selecting line profiles across axons or filopodia and applying a Gaussian fit. This was used in optical membrane potential imaging (Figure 4.7) and calpain activity experiments (Figure 5.8)

APPENDIX II: Script used for analysis of fluorescent intensities of semi-automatically thresholded ROIs. This was used for quantitative immunofluorescence (Figure 4.2, a slightly earlier version of the script), (Figure 4.3), as well as for the intensity analysis of the TMR-dextran growth cones in (Figure 4.1).

APPENDIX III: Script used for morphological analysis of TMR labelled growth cones, relevant to Figure 4.1

APPENDIX 1.1: ADDITIONAL STATISTICS

Data in Figure 1.8A were assessed with a ANOVA ($1.2e^{-19}$), followed by a Bonferroni post hoc test. All p-values are listed in the following chart, wherein fn = fibronectin, ln = laminin, GsM = GsMTx-4

Table 6: Complete statistics for Figure 1.8

Data in Figure 1.8A were assessed with a ANOVA ($1.2e^{-19}$), followed by a Bonferroni post hoc test. All p-values are listed in the following chart, wherein fn = fibronectin, ln = laminin, GsM = GsMTx-4

Comparison	P-Values
100Pa fn→ 1kPa fn	0.056
100Pa ln ctrl → 1kPa ln ctrl	$2.1e^{-08}$
100Pa fn → 100Pa ln ctrl	0.03
1kPa fn → 1kPa ln ctrl	$2.2e^{-08}$
100Pa ln ctrl→ 100Pa ln GsM	0.066
1kPa ln ctrl →1kpa ln GsM	$2.1e^{-08}$
100Pa ln GsM→ 1kPa ln GsM	0.0089
100Pa ln ctrl →1kP ln GsM	1.0
1kPa ln ctrl → 100Pa ln GsM	$2.1e^{-08}$

APPENDIX 3.1: ADDITIONAL STATISTICS

Table 7: Complete statistics for Figure 3.2

'R' indicates values from the randomized (blinded) group. Blue → comparisons between conditions in unblinded group; Green → comparisons between conditions in unblinded group; violet → comparisons between blinded and unblinded groups.

Comparison	χ^2	P-value
Sema100Pa-mock100Pa	7.41	0.0065
Sema1kPa -mock1kPa	17.51	$2.9e^{-05}$
Sema10kPa-mock10kPa	80.95	$2.3e^{-19}$
Sema100Pa-Sema1kPa	8.116	0.0044
Sema100Pa-Sema10kPa	18.95	$1.3e^{-05}$
Sema1kPa-Sema10kPa	0.5778	0.45
Sema100Pa R-mock100Pa R	24.52	$6.3e^{-07}$
Sema1kPa R -mock1kPa R	37.66	$8.4e^{-10}$
Sema10kPa R -mock10kPa R	89.05	$3.9e^{-21}$
Sema100Pa R -Sema1kPa R	7.185	0.0074
Sema100Pa R -Sema10kPa R	10.97	$9.2e^{-04}$
Sema1kPa R -Sema10kPa R	0.1167	0.73
Sema100Pa – Sema100Pa R	2.56	0.11
Sema1kPa – Sema1kPa R	2.802	0.094
Sema10kPa – Sema10kPa R	1.684	0.19
mock100Pa – mock100Pa R	1.56	0.21
mock1kpa – mock1kPa R	2.088	0.15
mock10kPa – mock10kPa R	0.922	0.34

Table 8: Complete statistics for Figure 3.1 and Figure 3.3

Blue → comparisons between 500 ng/µL treatment and controls, Green → comparisons between 150 ng/µL treatment and controls; orange → comparisons between 500 ng/µL and 150 ng/µL.

Comparison	χ^2	P-value
Sema100Pa_500-mock100Pa	93.78	$3.5e^{-22}$
Sema1kPa_500-mock1kPa	293.8	$7.4e^{-66}$

Sema100Pa_500-Sema1kPa_500	17.56	$2.8e^{-05}$
Sema100Pa_500-mock1kPa	150.6	$1.3e^{-34}$
Sema1kPa_500-mock100Pa	206.7	$7.3e^{-47}$
Sema100Pa_150-mock100Pa	49.95	$1.6e^{-12}$
Sema1kPa_150-mock1kPa	191	$1.9e^{-43}$
Sema100Pa_150-Sema1kPa_150	13.84	$2.0e^{-04}$
Sema100Pa_150-mock1kPa	96.36	$9.6e^{-23}$
Sema1kPa_150-mock100Pa	117.4	$2.4e^{-27}$
Sema100Pa_150-Sema100Pa_500	11.58	$6.7e^{-03}$
Sema1kPa_150-Sema1kPa_500	25.92	$3.5e^{-07}$
Sema100Pa_150-Sema1kPa_500	66.34	$3.8e^{-16}$
Sema100Pa_500-Sema1kPa_150	0.06621	0.80
mock100Pa-mock1kPa	93.78	0.015

APPENDIX 4.1: SUPPLEMENTARY FIGURE

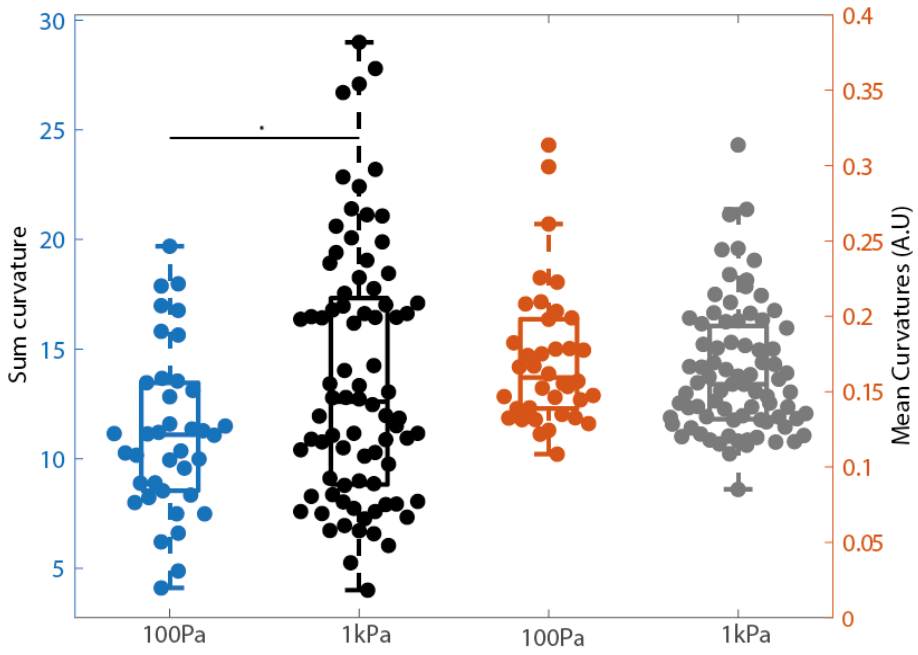

Figure S 1: Additional Parameters from morphological analysis

*This figure pertains to Figure 4.1, please see the caption thereof for methodological details and explanation. Summed curvature values are greater on soft substrates (*p = 0.02, two sample t-test.), but this effect disappears when they are normalized to the length of the growth cone outline (p=0.34, two sample t-test)*

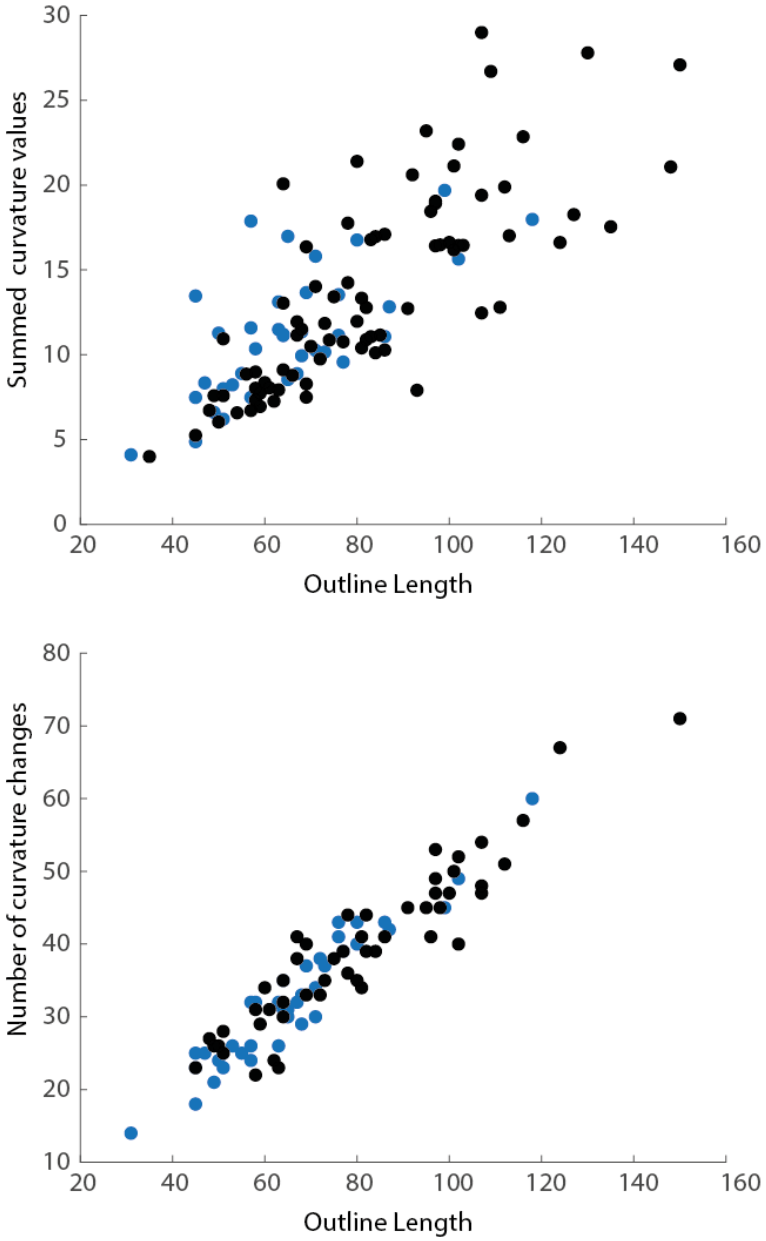

Figure S 2: Sum curvature and curvature changes scale with the length of the growth cone perimeter

This figure pertains to Figure 4.1, please see the caption thereof for methodological details and explanation. The sum curvature (top) and number of curvature changes (bottom) from the 39 growth cones used in the morphological analysis on soft (blue) or 52 growth cones analysed on stiff (black) substrates are scattered against the length of the outline. Both parameters seem to scale linearly with the length of the outline.

APPENDIX 4.2: ADDITIONAL STATISTICS

Table 9: Complete statistics for Figure 4.4

Green shading indicates comparisons among 1 kPa conditions, salmon shading among 100 Pa conditions, and orange shading indicates comparisons between 1 kPa and 100 Pa conditions.

Comparison	χ^2	P-value
1kPa_ctrl_ctrl→ 1kPa_ctrl_Sema	135.2	$3.1e^{-31}$
1kPa_200nM_ctrl→ 1kpa_200nM_Sema	97.31	$5.9e^{-23}$
1kPa_500nM_ctrl→ 1kpa_500nM_Sema	2.78	0.096
1kPa_ctrl_Sema→1kPa_200nM_Sema	0.2515	0.62
1kPa_ctrl_Sema→ 1kPa_500nM_Sema	33.35	$7.7e^{-09}$
1kPa_200nM_Sema→1kpa_500nM_Sema	28.23	$1.1e^{-07}$
100Pa_200nM_ctrl→100Pa_200nM_Sema	53.22	$3.0e^{-13}$
100Pa_500nM_ctrl→100Pa_500nM_Sema	35.59	$2.5e^{-09}$
100Pa_ctrl_ctrl→ 100Pa_ctrl_Sema	30.35	$3.6e^{-08}$
100Pa_ctrl_Sema→ 100Pa_500nM_Sema	0.275	0.60
100Pa_200nM_Sema→ 100Pa_500nM_Sema	3.129	0.08
100Pa_ctrl_Sema→100Pa_200nM_Sema	3.004	0.083
1kpa_ctrl_Sema→ 100Pa_ctrl_Sema	3.83	0.050
1kPa_500nM_Sema→100Pa_500nM_Sema	14.63	$1.3e^{-04}$
1kpa_200nM_Sema→100Pa_200nM_sema	0.2702	0.60

APPENDIX 5.1: SUPPLEMENTARY FIGURE

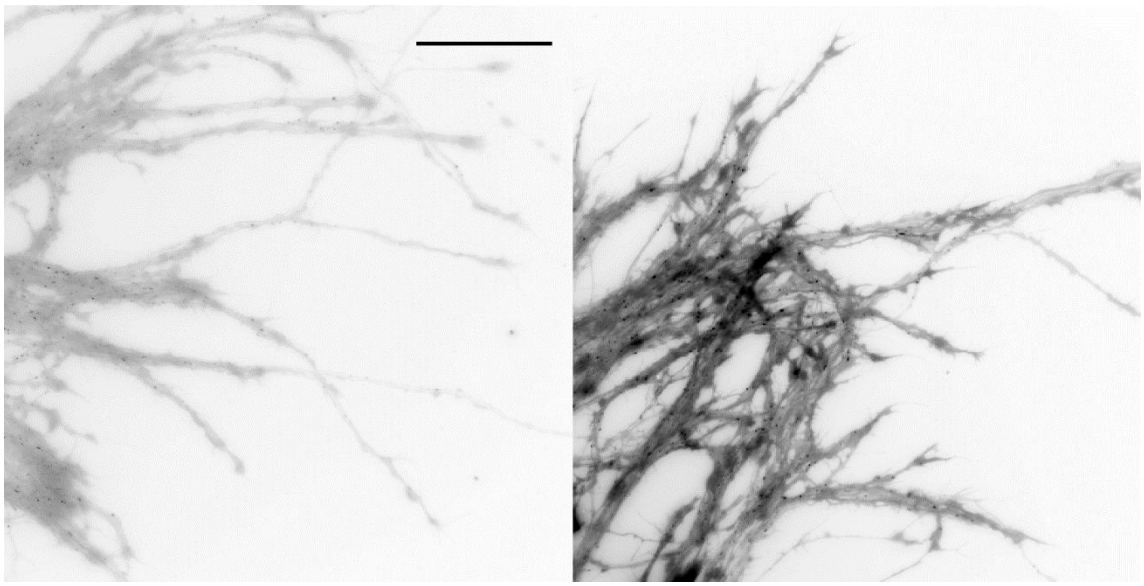

Figure S 3: Photobleaching of t-BOC assay

This figure pertains to Figure 5.8. Images taken at the 20 minute point from t-BOC assays where cultures were imaged every 4 minutes (let) or imaged only once at the end of the time period (right). In other respects the cultures were identical. There is a clear effect of more frequent imaging on the fluorescence intensity of the dye. Scale bar is 50 µm.

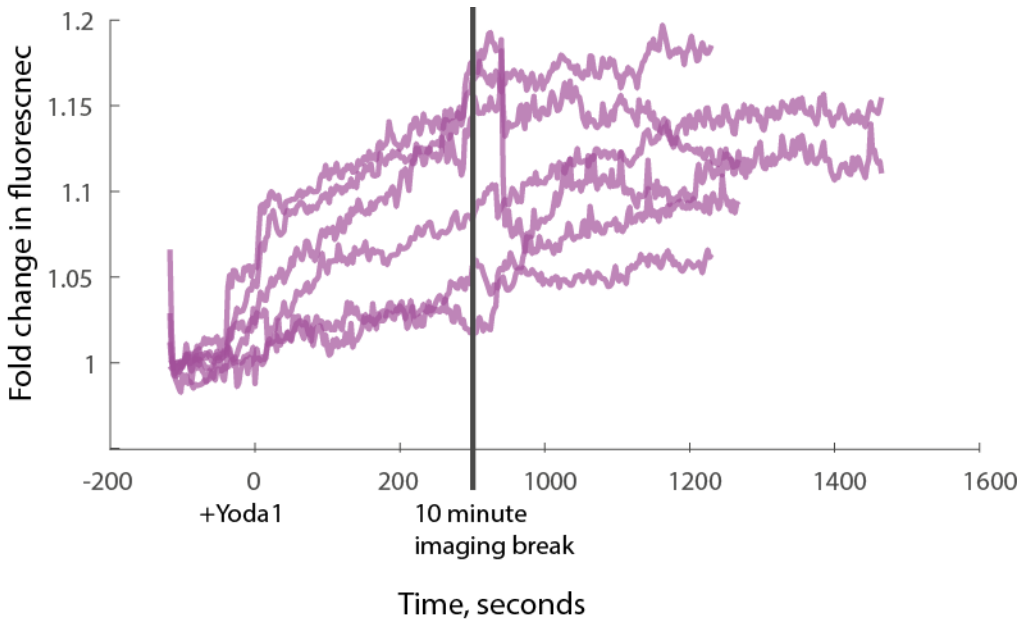

Figure S 4: Yoda1 causes an increase and accumulation of calcium in RGC neurons

Figure S 4: (continued)

This figure pertains to Figure 5.8. Yoda was added at the 0 minute mark, at which point fluorescence beings to increase. These traces are from three separate cultures, taken on the same day, with two small ROI's analysed for each culture. ROIs were selected to be regions that were covered or almost completely covered with axons. Traces are normalized to the fluorescence intensity of the first frame. Cultures were imaged for another 5 minutes, during which fluorescence continued to increase. A 10 minute imaging break was taken and then cultures were imaged for ~5 minues again.

APPENDIX 5.2: ADDITIONAL STATISTICS

Table 10: Complete statistics for Figure 5.7

High S3A dosage	$\chi 2$	p-value
Sema3A→ CTRL	115.8	$5.3e^{-27}$
Sema3A + Yoda1 → CTRL + Yoda1	83.7	$5.8e^{-20}$
Sema3A→ Sema3A + Yoda1	0.0899	0.76
CTRL → CTRL + Yoda1	2.21	0.14
Sema3A → CTRL + Yoda1	84.1	$4.7e^{-20}$
Sema3A + Yoda1 → CTRL	116.4	$3.9e^{-27}$
Low S3A dosage	$\chi 2$	p-value
Sema3A→ CTRL	45.00	$2e^{-11}$
Sema3A + Yoda1 → CTRL + Yoda1	30.14	$4.0e^{-08}$
Sema3A→ Sema3A + Yoda1	0.45	0.50
CTRL → CTRL + Yoda1	1.01	0.31
Sema3A → CTRL + Yoda1	35.2	$3.0e^{-09}$
Sema3A + Yoda1 → CTRL	33.8	$6.0e^{-09}$

APPENDIX 6.1: SUPPLEMENTAL FIGURE

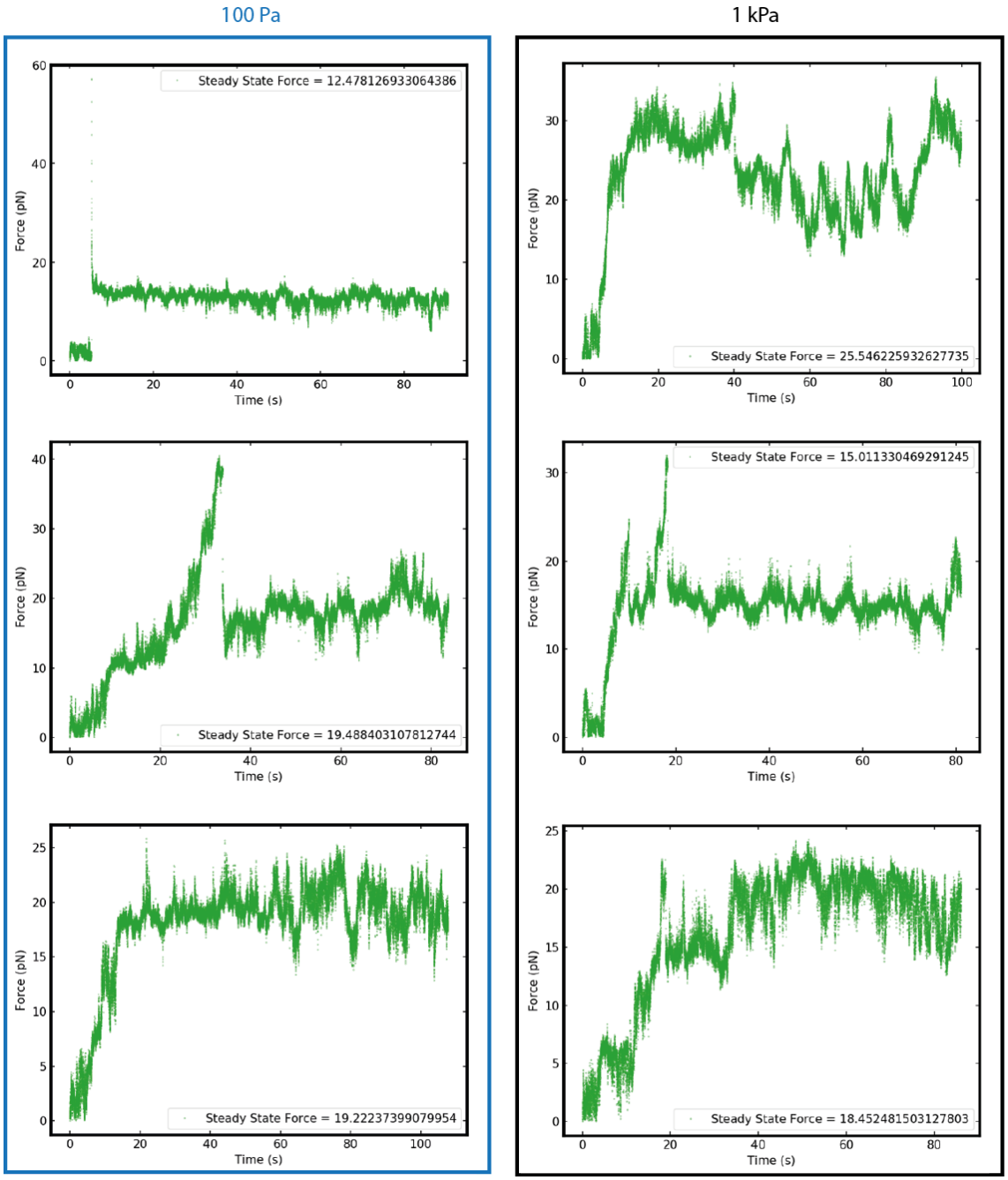

Figure S 5: Force profiles of tethers exhibit significant diversity

Randomly selected force vs time curves from tethers pulled on soft (left, blue outline) and stiff (right, black outline). Note that the y-axes are not consistent. Data courtesy of Jeffrey Mc Hugh.

APPENDIX I: GAUSSIAN FITTING FOR AXONS IN THE CALPAIN ACTIVITY AND MEMBRANE POTENTIAL ANALYSIS

The explicit input to the function is the name of the file analysed. The file in .nd2 format is selected using the freely available BioFormats toolbox (bfmatlab ())

```
function [FitHeight] = vsd_analysis_Final(FileName)
close all;

addpath('c:\users\sarah\Documents\MATLAB\bfmatlab')
%extract from ND2 files
myfiles = bfopen();
data = myfiles{1};
numfiles = 3;
%grab three frames
frame1data = data{1};
frame2data = data{2};
frame3data = data{3};

datastack = cat(3,frame1data,frame2data,frame3data);

topfolder = uigetdir('select');
cd(topfolder);

Subtracted = [];

for b = 1:numfiles
    Imcur = datastack(:,:,b);
    if b ==1;
        imagesc(Imcur);
        BW = roipoly;
        background = mean(mean(Imcur(BW == 1)));
    end
    Imcur = Imcur - background;
    Subtracted(:,:,b) = Imcur;
    close all
end

Submean_new = mean(Subtracted,3); %averages first three subtracted frames

%select line profiles across 'individual axons' of averaged image, then do
gaussian fits
FitHeight = [];
Fitsigma = [];
line = 1;
while line == 1
    figure, current = imagesc(Submean_new);

    h = drawline();
    bounds = h.Position;
    BW = createMask(h,current);
    SE = strel('diamond',5);
    BWnew = imdilate(BW, SE);
    close(gcf);
```

```
    Submean = Submean_new;

    Submean(BWnew == 0) = NaN;
    LineMean = nanmean(Submean);
    x1 = round(bounds(1,1)); y1 = round(bounds(1,2)); x2 = round(bounds(2,1));
y2 = round(bounds(2,2));
    width = x2-x1;
    xvals = 1:width;
    LineMean = LineMean(x1:(x1 + width-1));

    scatter(1:width,LineMean)
    gauss1fit = fittype('a.*exp(-((x-b)/c).^2)+d');

    start = [1000,7.5,4.25,24]; % initial guess: 1000 for axons, 200 for
filopodias
    options = fitoptions('Method','NonlinearLeastSquares','StartPoint',start);
    f = fit(xvals',LineMean',gauss1fit,options);
    plot(f,xvals,LineMean)
    myc = coeffvalues(f);
    answer1  = questdlg('keep line?','','Yes','No','Yes');
    switch answer1
        case 'Yes'
            FitHeight = cat(2,FitHeight,myc(1));
            Fitsigma = cat(2,Fitsigma,myc(3));
            close(gcf)
        case 'No'
            close(gcf)
%             continue
    end
    answer2 = questdlg('new line?','','Yes','No','Rotate Image','Yes');
    switch answer2
        case 'Yes'
            Line = 1;
        case 'Rotate Image'
            Submean_new = imrotate(Submean_new,90);
        case 'No'
            Line = 0;
            break
    end
end
csvwrite(strcat(FileName,'.txt'),cat(1,FitHeight,Fitsigma))
```

APPENDIX II: QUANTITATIVE IMMUNOFLUORESCENCE ANALYSIS

The following code was used for analsysis of Npn1- stained growth cones:

```
addpath('c:\users\sarah\Documents\MATLAB\bfmatlab')

%extract from ND2 files
myfiles = bfopen();
numfiles = length(myfiles);
Int_medians = [];
Int_means = [];

prompt = {'Enter filename'}; title = 'name'; dims = [1 35]; definput =
{'dish_stiffness_specify'};
flname = inputdlg (prompt,title,dims,definput);
flname = flname{1};

j = 3; %index of desired channel
for a = 1:numfiles

    data = myfiles{a};

    data2 = data{j};

    Subtracted = [];

    imagesc(data2);
    BW = roipoly;
    background = mean(mean(data2(BW == 1)));
    DataSub = data2 - background;

    close all

    FitHeight = [];
    Fitsigma = [];
    line = 1;
    while line == 1
        figure, current = imagesc(DataSub);
        BW = roipoly;
        DataSub2 = DataSub; DataSub2(BW == 0) = 0;
        level = graythresh(DataSub2);
        imthresh = 1;
        while imthresh == 1
            BW2 = imbinarize(DataSub2,level);
            imshowpair(DataSub2,BW2,'montage')
            answer1  = questdlg('keep segmentation?','','Yes','New
Threshold','No','Yes');
            switch answer1
                case 'Yes'
                    int_mean = mean(mean(DataSub2(BW2 ==1)));
                    int_median = median(median(DataSub2(BW2 ==1)));
                    close(gcf)
                    imthresh = 0;
                case 'New Threshold'
```

```
                    close(gcf)
                    prompt = {'Enter new threshold'}; title = 'New Threshold';
dims = [1 35]; definput = {num2str(level)};
                    answer = inputdlg (prompt,title,dims,definput);
                    answer = answer{1};
                    level = str2num(answer);
        %             continue
                case 'No'
                    close(gcf)
                    imthresh = 0;
            end
        end
        Int_means = cat(2,Int_means,int_mean);
        Int_medians = cat(2,Int_medians,int_median);
        answer2 = questdlg('new growth cone?','','Yes','No','Yes');
        switch answer2
            case 'Yes'
                Line = 1;
            case 'No'
                Line = 0;
                break
        end
    end
end
csvwrite(strcat(flname,'_means'),Int_means);
csvwrite(strcat(flname,'_medians'),Int_medians);
% end
```

Code used for other fluorescence intensity analysis with slight modifications (this version was used for the TMR-dextran growth cones and therefore also outputs perimeter. This code was modified from an original script written by Max Jacobs

```
direc = uigetdir();

cd(direc)

file = dir('*.tif');
len = length(file);

areas = [];

for i = 1:len
    I = importdata(file(i).name);
    I = I(:,:,1);
    imagesc(I);
    BG = roipoly();
    BGlevel = mean(mean(I(BG==1)));
    Isub = I-BGlevel;
    cla;
    imagesc(Isub)

    mkdir('processed_perimetercalc')
```

```
    fudgeFactor = 0.9
    flag = 1;
    count = 0;
    diamond = 2;
    while flag == 1
        if count >0
            fudgeFactor=inputdlg('Please give a new fudgefactor >0:','Input',1
,{num2str(fudgeFactor)});
            fudgeFactor=str2num(fudgeFactor{:});
        end
        count = count +1
        [~,thresh] = edge(Isub,'sobel');
        BWs = edge(Isub,'sobel',thresh*fudgeFactor);
        figure, imshow(BWs)
        se90 = strel('line',2,90);
        se0 = strel('line',2,0);
        BWdil = imdilate(BWs,[se90 se0]);
        figure, imshow(BWdil)
        BWdfill = imfill(BWdil,'holes');

        diamond=inputdlg('Enter diamond size (integer):','Input',1
,{num2str(diamond)});
        diamond=str2num(diamond{:});
        seD = strel('diamond',diamond); % diamond initially set to 3, change
for GC's with high halo.
        BWfinal = imerode(BWdfill,seD);
        %figure, imshow(BWfinal), title('segmented image');
        clear se0 se90
        %get outline image
        BWoutline = bwperim(BWfinal);
        Segout = I;
        Segout(BWoutline) = 655555;

        IsubA = imadjust(Isub);

        figure, montage({IsubA,Segout})%h=imshow(Segout);
        reply=questdlg('Happy? (indicate <cancel> to skip to next image)');
        close(gcf)
        if strcmpi(reply,'yes')
            h = msgbox('select growth cone')
            figure; roiMask = roipoly(Segout);
            close(gcf)
            BWfinal(roiMask==0)=0
            roiMask = BWfinal
            MaskBound = bwboundaries(roiMask); %maskbound gives me the
boundaries of image
            [~,index]=max(cellfun(@length,MaskBound));

roiMask=poly2mask(MaskBound{index}(:,2),MaskBound{index}(:,1),size(roiMask,1),
size(roiMask,2));
            %make nicer
            roiMask=imfill(roiMask, 'holes');
            %check if mask is ok now
            BWoutline = bwperim(roiMask);
```

```
            figure,imshow(BWoutline); %this output is the outline that we
want!
            reply=questdlg('Happy?');
            close(gcf)
            if strcmpi( reply,'no')
                flag=1;
            elseif strcmpi(reply,'cancel')
                continue
            else
                flag=0;
                AREAGC = sum(sum(roiMask ==1)); %area, also in pixels
                PERIMGC = sum(sum(BWoutline)); %perimeter- in pixels
                nMEANINT = mean(mean(Isub(roiMask==1))); %bg subtracted
fluorescence intensity
                dlmwrite(strcat(file(i).name,'data','.txt'),[AREAGC PERIMGC
PERIMGC/AREAGC nMEANINT]);
            end
        elseif strcmpi(reply,'cancel')
            flag = 0;
        end
        clear BG MASK
        close all
    end
    clear flag count
end
clearvars -except file
```

APPENDIX III: MORPHOLOGICAL ANALYSIS OF TMR-DEXTRAN GROWTH CONES

This code is to compute the curvatures from growth cone outlines. It makes use of the functions LineCurvatures2D and LineNormals2D written by Dirk-Jan Kroon and availably on the MathWorks website.

```
file = dir('*.tif');
numfiles = length(file);
curvatures = [];
pathc = cd;
mkdir('curvatures')

for a = 1:numfiles
    curr_n = file(a).name;
    roiMask = importdata(curr_n);
    N = 5;
    kernel = ones(N)/N^2;
    blurred = conv2(single(roiMask),kernel,'same');
    SmoothMask = blurred >0.5;

    SmoothBoundaries = bwboundaries(SmoothMask);
    segments = numel(SmoothBoundaries);

    check = [];

    for b = 1:segments
        new = SmoothBoundaries{b};
        check(b) = length(new);
    end

    idx = check == max(check);
    SmoothBoundaries = SmoothBoundaries{idx};
    xv = SmoothBoundaries(:,1); yv = SmoothBoundaries(:,2);
    fitlen = numel(xv);
    interval = 5;
    sections = 1:interval:fitlen;

    if numel(sections)<3
        continue
    end

     Lines = [];
     for b = 1:length(sections)-1
         Lines(b,:) = [sections(b) sections(b+1)];
     end

     k = LineCurvature2D(SmoothBoundaries,Lines);
     N = LineNormals2D(SmoothBoundaries,Lines);

     cindex = [];
    for a = 1: fitlen
        if k(a) == 0
            c = [0 0 0];
        elseif k(a)>0
```

```
            c = [1 0 0];
        elseif k(a)<0
            c = [0 0 1];
        end
        cindex = cat(1,cindex,c);
    end

    figure,
    scatter(xv,yv,10,cindex);
    hold on
    kk = k.*100;
    plot([SmoothBoundaries(:,1) SmoothBoundaries(:,1)+kk.*N(:,1)]',
[SmoothBoundaries(:,2) SmoothBoundaries(:,2)+kk.*N(:,2)]','g');
    csvwrite(strcat(pathc,'\curvatures\',curr_n,'_curvatures.txt'),k);

csvwrite(strcat(pathc,'\curvatures\',curr_n,'_smoothboundaries.txt'),SmoothBou
ndaries);
    meancurv = nanmean(abs(k));
    curvatures = cat(1, curvatures, meancurv);
end
```

This code is to compute the number of inflections in the curvature, using text files output from the previous script

```
%this code is run on the raw text files, and is meant to evaluate how often
%curvature switches from positive to negative.

files = dir('*.txt');

numfiles = numel(files);

switches = [];
counts = [];
for a = 1:numfiles
    k = strfind(files(a).name,'curvatures');
    if k/k== 1
        B = importdata(files(a).name);
        BB = B(~isnan(B));
%         counter = [];
        for a = 1:length(BB)
            if BB(a) >= 0
                BB(a) = 1;
            elseif BB(a) < 0
                BB(a) = -1;
            end
        end
        x = [];
        for c = 1:(length(BB)-1)
            x(c) = BB(c) + BB(c+1);
        end
        counter = sum(x==0);
        counts = cat(1,counts,length(BB));
```

```
        switches = cat(1,switches,counter);
    end
end

data= cat(2,switches,counts);
```